Photon production and screening properties of the QGP from lattice QCD

Dissertation zur Erlangung des Grades
"Doktor der Naturwissenschaften"

vorgelegt beim Fachbereich Physik, Mathematik und Informatik der
Johannes Gutenberg-Universität Mainz

Aman Steinberg

geboren in Darmstadt

Mainz, den 24. Oktober 2020

Datum der mündlichen Prüfung: 22. Februar 2021

This page is left blank intentionally.

Parts of this work were used as contributions for the following preprints:

- *The rate of photon production in the quark-gluon plasma from lattice QCD* [64].
  I contributed the generation of the X7 gauge ensemble (see chapter 4).

- *Lattice QCD estimate of the quark-gluon plasma photon emission rate* [94].
  I contributed the generation of the X7 gauge ensemble (see chapter 4).

- *An estimate for the thermal photon rate from lattice QCD* [90].
  I contributed the generation of the X7 gauge ensemble (see chapter 4), the investigation of the parameter landscape for the fitting of the continuum data using an ansatz for the spectral function, and cross-checks for the adaption of the Backus-Gilbert formalism to our problem (see chapter 6).

- *Static and non-static vector screening masses* [67].
  I contributed the generation of the Y7 gauge ensemble (see chapter 4), the calculation of correlators, the extraction of thermal screening masses and amplitudes from the correlators as well as the computation of the effective screening mass and amplitude from the effective approach (see chapter 5).

Abstract

In this work, properties of the quark-gluon plasma are studied, in particular thermal screening masses and the photon production rate. We employ the numerical realization of Quantum Chromodynamics (QCD) called lattice QCD. To the end of calculating screening masses and the rate of photon emission we generate lattice gauge ensembles at temperatures of 254 and $508\,\mathrm{MeV}$ well above the chiral and deconfinement phase transition temperature $T_c \approx 155\,\mathrm{MeV}$ at vanishing net baryon chemical potential and measure the relevant observables on the gauge configurations. The lattice regularized action contains the Wilson gauge action and the $\mathcal{O}(a)$ improved Wilson fermions with $N_f = 2$ mass degenerate light flavors. The generation of the finite-temperature ensembles is performed after careful tuning of the lattice and algorithmic parameters. The ensemble at $254\,\mathrm{MeV}$ enables a continuum extrapolated estimation of the photon emission rate from the quark-gluon plasma where we use two further ensembles at the same temperature that were previously generated within the Mainz lattice group.

Contents

Chapter 1

Heavy-ion Collisions and Quantum Chromodynamics

One of the main research avenues for fundamental research in the area of strongly interacting matter is the quest to understand the emergence of hadronic matter from its constituents - the so-called quarks and gluons. Research in the late 1960s showed that nucleons are composites of three valence quarks. The masses of the quarks inside a nucleon, however, sum up to $\sim 10\mathrm{MeV}$, while the mass of the nucleon lies at $\sim 940\mathrm{MeV}$. Thus, one concluded, about 99% of the nucleon's mass is generated dynamically by the strong interaction [1]. The theory that describes strongly interacting particles is called Quantum Chromodynamics (QCD) with its fundamental degrees of freedom being quarks and gluons. These elementary particles carry a color charge which makes them sensitive to the strong interaction. Hence, the underlying quantum field theory is named Quantum Chromodynamics from the Greek $\chi\varrho\acute{o}\mu o\varsigma$ meaning 'color'.

1.1 Motivation and the QCD phase diagram

When it comes to the emergence of hadrons from quarks and gluons, one has to face the phenomenon that no free quarks have yet been found in nature, they are *confined* into composite objects called hadrons. This color confinement and the dynamical mass generation take place in the regime of low momentum transfer where α_s (the coupling of the strong interaction) is large and non-perturbative techniques need to be applied [1]. One remarkably successful non-perturbative technique is lattice QCD which is reviewed in chapter 2.

The QCD vacuum is filled with a number of condensates related to the origin of

hadronic masses [1]. The chiral condensate is one such condensate and serves as an order parameter for chiral symmetry restoration. When examining QCD at finite temperature (i.e., not in vacuum) one observes that the chiral phase transition occurs at the same temperature as the deconfinement phase transition (at least for zero baryon-chemical potential) [1]. Far above this temperature, quarks and gluons are indeed deconfined and can move quasi-freely. This deconfined phase is called the quark-gluon plasma (QGP). According to most cosmological models concerning the history of the universe, deconfined matter has been realized in nature as a QGP only from about a picosecond to about a few microseconds after the Big Bang in extreme conditions at temperatures greater than $150\,\mathrm{MeV}/k_B$[1]. Therefore, free quarks have not yet been detected in nature around humans. Nonetheless, the properties of the QGP at finite temperature and density have sparked active research endeavors around the globe and are also the subject of this work. In particular, I want to estimate *the photon production rate of the quark-gluon plasma* by computing and reconstructing the spectral function related to the vector channel within the framework of lattice QCD. The QGP is probed in experiments so that theoretical predictions can be confronted with data. Apart from the deconfined QGP phase of QCD there is also a confined hadronic phase.

The phase diagram of QCD

The thermodynamic phases of QCD can be mapped to the plane spanned by temperature T and net baryon chemical potential $\mu_B \equiv \mu$. The resulting arrangement is called the phase diagram of QCD, see fig. 1.1.

There are two phenomena in QCD that are responsible for the shape of the QCD phase diagram, deconfinement and the spontaneous breaking of chiral symmetry [2]. The latter is addressed in subsection 1.5.2, the former is a consequence of the so-called *asymptotic freedom* of QCD. Asymptotic freedom describes that the coupling α_s runs from large values at low momentum transfers or, equivalently, large distances to low values at large momentum transfers/short distances. In 2004, the Nobel Prize in Physics was awarded to Xxxxx and Xxxxxxx [3] as well as Xxxxxxxx [4] for the discovery of the running of the QCD coupling. In the low-energy phase of QCD, the hadron gas, the constituent quarks in the hadrons interact strongly because the coupling is strong.

[1] The universe might have been populated by free quarks and gluons even before that but only after the inflation period had ended. In that period between the end of inflation and $10^{-12}\,\mathrm{sec}$ after the Big Bang the electromagnetic and weak interactions would have still been unified and all particles would have been massless. The physics governing this primordial soup is not yet understood.

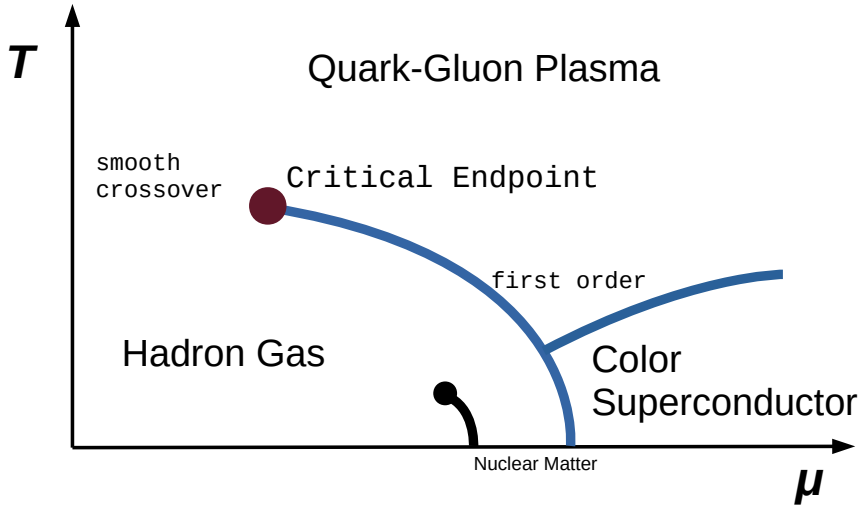

Figure 1.1: Schematic phase diagram of QCD in the plane of temperature T and net baryon chemical potential μ.

When a quark-antiquark pair, for example, is separated, that costs energy and at some point, it becomes energetically favorable for a new quark-antiquark pair to form such that the original pair is again bound into a compound object. This is the phenomenon of confinement of quarks and gluons into hadrons. At vanishing chemical potential $\mu = 0$, the coupling between quarks decreases for increasing temperature and above a critical temperature T_c, quarks and gluons are deconfined. The corresponding phase is the quark-gluon plasma phase where quarks and gluons can move freely. A striking observation is that at T_c, not only are quarks and gluons deconfined, but the chiral symmetry is restored while it is spontaneously broken in the hadronic phase below T_c [2]. As discussed in subsection 1.5.2, chiral symmetry is explicitly broken due to small finite quark masses. Thus, the phase transition at vanishing chemical potential between the hadron gas and the quark-gluon plasma is a rapid, but smooth crossover rather than a true phase transition [2]. In the $N_f = 2$ chiral limit (with the up and down quark masses set to zero), the phase transition is of second order.

At nonvanishing chemical potential $\mu > 0$, however, the phase transition is thought to change its type. It is first-order above some critical baryon-chemical potential μ_c. The first-order phase transition line (blue line in fig. 1.1) must therefore end at a critical endpoint [2]. The existence and the position of this critical endpoint is subject of current research activities both from the theoretical and the experimental side, see Ref. [2] for a recent review. At lower temperatures and intermediate baryon-chemical potential, the matter that is described there could be studied in the core of neutron

stars [2]. Finally, at low temperatures and very large chemical potential, it is possible for a superconducting phase to appear. The quarks then would form BCS pairs with color-flavor locking [2].

The hadron gas predominantly consists of pions and is rather dilute compared to the dense QGP phase. At sufficiently low temperatures, the hadron gas behaves as a nearly ideal gas; and at sufficiently high temperatures, the coupling between quarks and gluons is so weak (because of asymptotic freedom) that the QGP can approximately be described as an ideal gas, too [2]. Along the curve of first-order phase transitions in the $T - \mu$ plane, the pressure and energy density of the two phases must be equal according to Gibbs's criterion. The two phases coexist on the first-order phase transition line [2]. One consequence of the coexistence of the two thermodynamic phases is the occurrence of large fluctuations at the critical point [2]. It is important to remark that the fluctuations in the physical systems are accompanied by long-range correlations [2].

1.2 The photon rate in heavy-ion collisions

In order to study hot and dense strongly interacting matter in the laboratory, one has to produce it by colliding heavy ions in particle colliders such as the LHC at CERN and RHIC at Brookhaven. There is evidence that the matter created in such heavy-ion collisions is equilibrated [1], therefore one concludes that it reproduces the matter that the universe consisted of $\sim 10^{-6}\,\mathrm{sec}$ after the Big Bang. Thus, experiments at LHC and RHIC are employed to study the properties of this primordial matter.

In recent studies (e.g. [5, 6]), however, even non-equilibrium effects like, for instance, momentum anisotropies during the very early stages of the heavy-ion collision are getting more and more attention. In Ref. [5], the authors study the dilepton production rate and elliptic flow using models for relativistic anisotropic hydrodynamics. It is believed that dileptons with intermediate masses of $M \sim 1 \ldots 3\,\mathrm{GeV}$ created in the medium convey information about the earlier stages of the QGP above the deconfinement phase transition temperature whereas dileptons with a mass of less than about $1\,\mathrm{GeV}$ are created predominantly from hadronic matter below the critical temperature and can give insight about the spectral functions of vector mesons [5].

The QGP produced in the initial stages of the collision ($\tau \lesssim 1\,\mathrm{fm/c}$) at LHC or RHIC energies is driven out of equilibrium due to a fast longitudinal expansion of the system. This results in a state which is only pseudo-thermalized but is used in phenomenological calculations as initial stage of a dissipative hydrodynamic evolution until freeze-out and

hadronization ($1\,\mathrm{fm/c} \lesssim \tau \lesssim 10\,\mathrm{fm/c}$) [5]. Dissipative relativistic hydrodynamics was successful so far in describing thermodynamic quantities, collective flow and transport properties of the expanding QGP at RHIC and LHC energies [5].

Anisotropies in collective flow observed in heavy-ion collisions are due to a spatial asymmetry of the collisions and fluctuations in the initial shape of the system. Additionally, when the system undergoes a rapid longitudinal expansion, the momentum distribution functions on the parton level become anisotropic, too [5]. Thus, they will affect the emission rates of electromagnetic probes from the early QGP stages. In order to account for these anisotropies in the momentum distribution, one has to extend ideal hydrodynamics models. On top of that, the authors of Ref. [5] study the effect of the shear viscosity over entropy density ratio for the hydrodynamical evolution of the medium. Their findings suggest that it is important not to neglect effects of anisotropies connected to non-equilibrium thermodynamics in the very early stages of a relativistic heavy-ion collision when examining dilepton emission and elliptic flow.

Although the QGP created at the LHC or RHIC has not yet equilibrated locally or thermally during the early stages of the collisions, dissipative hydrodynamical models are quite successful in describing the evolution of the energy-momentum tensor[2] already after $\sim 1\,\mathrm{fm/c}$ [6]. XXXXX [6] explains this by introducing a non-equilibrium attractor, a solution of the dynamical equations onto which all solutions collapse during the evolution of the system. As soon as a solution collapses onto the attractor, it becomes pseudo-thermalized, i.e. while information about its exact initial conditions is obscured, the solution has not yet reached local thermal equilibrium [6]. Thus, results from hydrodynamical models assuming local thermal equilibrium still provide valuable insights for understanding the evolution of a heavy-ion collision.

The medium that is generated during a heavy-ion collision evolves rapidly starting from the initial nuclear impact until the dissolution of the medium [1]. Historically, measuring photon and dilepton rates was suggested as a means to probe whether a QGP has actually formed during a relativistic heavy-ion collision [7]. Because the thermal dilepton yield from a QGP should exceed the one from a hadron gas far below the ρ mass, an observation of photon excess below this mass was considered proof of QGP formation [8]. The temperature of this medium then could be inferred from the photons that escape at the early stages of the collision [7]. As was shown in Ref. [9] by including two-loop diagrams in the calculation of the photon emission rate, the dominant

[2] On astrophysical scales, large anisotropic fluctuations in the energy-momentum tensor can give rise to gravitational waves, see section 1.3.

contribution at large transverse momenta comes from quark-antiquark annihilation and quark-gluon rescattering. This gives rise to an excess photon yield compatible with the one observed in experiments [8, 10].

When electrically charged particles scatter off each other inside the medium, real photons can be produced while virtual photons are created by particle-antiparticle annihilation processes; these virtual photons then later decay into dilepton pairs [7]. Once real or virtual photons are produced in the medium, they interact with the constituents of the hot and dense matter only through the electromagnetic interaction [7]. This results in a mean free path typically larger than the extent of the fireball. Hence, the photons and dileptons can escape the medium without secondary re-scatterings and provide direct information on the early stages of the heavy-ion collision because the photon rates are largest at the beginning of the collision [7]. They are nonetheless produced throughout the entire evolution of the collision. Hadronic probes, however, mainly probe the later stages of the collision after they have undergone multiple re-scatterings as a consequence of their short mean free path inside the hot and dense medium. They can escape the medium only after it has cooled down and the freezeout stages have begun [7]. These rapid changes during the entire history of the fireball constitute a challenge when one wants to reconstruct the events from the initial impact to the dissolution of the medium [1]. Therefore, even under the assumption of local thermal equilibrium it is important to have a good understanding of the evolution of the medium with respect to temperature and baryon-density when one wants to connect dilepton or photon emission rates to space-time integrated spectral functions in the vector channel [1]. Many intricate models have been developed and tested to this end and one can see that model calculations reproduce dilepton spectra from heavy-ion collisions [1]. The goal of this work, however, does not consist in applying a suitable model but in managing to calculate spectral functions and production rates from the *ab initio* theory of QCD itself. This endeavor faces as its main challenge the numerical computation of the relevant correlation functions and the solution of an inverse problem.

Other sources of photons in heavy-ion collisions

One of the main tasks of phenomenologists trying to describe the physics of relativistic heavy-ion collisions consists in including the complex processes occurring before, during and after equilibration of the medium. Various phenomenological aspects of thermal photon emission in the QGP have been addressed. Apart from the above mentioned

annihilation with rescattering [9], there are other sources of (direct) single photons from quark matter: In the QGP, single photons arise from Compton scattering, annihilation and bremsstrahlung processes, and before equilibrium, the parton cascade model describes a sizeable amount of photons generated by the branching of quarks with timelike kinematics ($q \to q\gamma$) [11]. In a series of papers [12, 13, 14], Xxxxxx, Xxxxx and Xxxxx derive the photon (and gluon) emission rate of a relativistic quark-gluon plasma to leading order. They include bremsstrahlung, inelastic pair annihilation and the Landau-Pomeranchuk-Migdal effect rigorously. This was a seminal achievement as most state-of-the art models for relativistic hydrodynamics rely on their results to evaluate the photon rate in heavy-ion collisions. The authors of Ref. [15] mainly consider the origin of photons from hot hadronic matter. This is important because during a heavy-ion collision, the matter produced before the fireball and after the phase transition from the QGP phase to the (partly mixed and then purely) hadronic phase is predominantly composed of hadronic degrees of freedom. In Ref. [15], the photon production of light pseudo-scalar, vector and axial vector mesons is accounted for including strange and non-strange mesons. The evolution of the collision is modelled via integrating over the spatial and temporal history of the reaction. The expansion and cooling rates of a relativistic heavy-ion collision are governed by the equations of state (EOS) of the QGP or the hadron gas formed during the collision. Therefore it is crucial to know the EOS very precisely and study the effects of the initial conditions of the reaction. The convolution is performed under the constraint of conservation of net baryon number N_B and total entropy S; the ratio of S/N_B, however, must be fixed to match experiments [15]. Hard photons from nucleon-nucleon collisions come in three types: direct photons, fragmentation photons, background photons [16]. Two incoming partons can produce *direct* photons by Compton scattering and annihilation. *Fragmentation* photons are created when final state partons emit bremsstrahlung. When hadrons decay after the collision, they produce *background* photons, these originate mainly in the decay of $\pi^0 \to \gamma\gamma$. Sometimes, direct and fragmentation photons are subsumed under the term *prompt* photons[3] [15]. In order to accurately assess the prompt photon contribution to the observed spectra, one must understand the in-nucleus effects occurring during the collisions. Since photon production in p-p collisions is not yet fully understood, it is difficult to account for nuclear corrections (like the Cronin effect[4], for instance) in

[3] See also chapter 6.

[4] The Cronin effect describes modifications in the transverse momentum distribution of partons in a heavy-ion collision due to the scattering of partons within one colliding nucleon off partons within

heavy-ion collisions [15]. Nonetheless, the authors of Ref. [15], e.g, are able to reproduce the thermal photon emission rate measured in relativistic heavy-ion collisions [10] by including detailed knowledge of thermal emissions from the QGP and hadron gas as well as hadron reactions in the resonance gas. They also estimate the contribution of prompt photons. The thermal emission rates of photons and dileptons are tightly connected as they are both derived from the vector current correlator evaluated either at lightlike (for photons) or timelike (for dileptons) kinematics [15].

Survey of photon and dilepton spectra in heavy-ion collisions

In Ref. [18] and their follow-up work [11], results from the WA80 collaboration at CERN SPS are discussed. The authors compare different models describing a) a hot hadronic gas as initial state which cools and does not undergo a phase transition, and b) a QGP phase as initial state which evolves into a mixed phase of QGP and hadronic gas with a completely hadronic phase as final state and a first-order phase transition in between the initial and final states. They conclude that an evolution of the system starting from a hot hadronic gas cooling down without a QCD phase transition can be ruled out as it clearly overshoots the observed photon emission rate; and it would imply an initial hadron density that is rather unphysical [11].

In phenomenological analyses of the photon yields in $Pb + Pb$ collisions at the WA98 experiment located at CERN SPS, the authors of Ref. [19], for instance, find evidence that QGP is formed for a short time period, but the evidence is not strong. In Ref. [20], the authors are able to distinguish between hard and thermal photons to the photon yield in the WA98 experiment. They point out strong hints towards the creation of QGP for a very short time period ($\sim 1\,\mathrm{fm/c}$) mixed with a hot hadronic gas. It is important to note that one of the main intricacies consists in identifying the direct photons of the photon yield. In Ref. [21], one method is discussed how to separate contributions to the photon yield from direct and from decay photons. This method is applied by the authors of Ref. [22]. They present the contributions of hard (i.e. prompt) and thermal photons to the single photon yield in the WA98 experiment at CERN SPS and are able to reproduce the experimental data by solving relativistic hydrodynamical equations in $3+1$ dimensions. Similar to the previous work of [18, 11], the EOS must be determined in order to describe the expansion and cooling rate of the medium during the relativistic heavy-ion collision; and again they assume as initial state

another nucleon participating in the collision [17].

a) a hadronic gas without a phase transition, and b) a QGP phase with a first-order phase transition. It is important to note that the authors use two-loop perturbative calculations of the correlation functions entering the photon emission rate. When the static emission rate is known, one needs to perform a space-time convolution in order to calculate the total photon yield from a relativistic heavy-ion collision. For this, the EOS used contains hadronic degrees of freedom with masses of up to $\sim 2.5\,\mathrm{GeV}$. In particular, the reactions between the π, ρ, ω, η and the a_1 meson as well as their decay processes are considered. Even in-medium effects are included in the calculation of the yield. Their results, however, do not allow for a conclusive answer whether a QGP has formed or not.

This is different for the work of Ref. [23]. The authors include two-loop perturbative results and in agreement with Ref. [9], explain the results of the WA98 experiment [10] by the formation of a hot and dense quark-gluon plasma which enters a mixed phase of QGP and hot hadronic gas and finally undergoes a phase transition and freeze-out towards a purely hadronic state. In addition, they can rule out a hot hadronic gas as initial state formed in the collision. In fig. 1.2, the contributions of thermal and prompt photons to the single photon yield at the WA98 experiment are shown. For the discussion of prompt photons, see references in [23]. The thermal photons are described as originating from hot and dense quark matter in a QGP and a later mixed phase as well as from hadronic matter during the mixed phase and the final hadronic phase. The sum of prompt and thermal photons describes the expermiental data very well.

The WA98 experiment located at CERN consists of photon and hadron spectrometers with large acceptance [7]. The results relevant for the photon emission rates are derived from data taken at the experiment in 1995 and 1996. For a detailed explanation of the experiment's setup and the data analysis, the reader is kindly referred to Ref. [7].

In this experiment, particles are identified by a time-of-flight method and their momentum is also measured by means of a dipole magnet. Because one wants to minimize the photon background contribution, the beam travels in an evacuated pipe and the detector is designed such that there is only little amount of detector material in the flight path of the particles [7]. The actual photon spectrometer is called the lead-glass detector array, LEDA. About 97% of the photon yield comes from the decay processes of π^0 and η mesons [7]. Therefore it is crucial to accurately determine these decay yields in order to assess the yield of (thermal and prompt) direct photons. In the WA98 experiment, they are determined via the $\pi^0 \to \gamma\gamma$ and $\eta \to \gamma\gamma$ channels

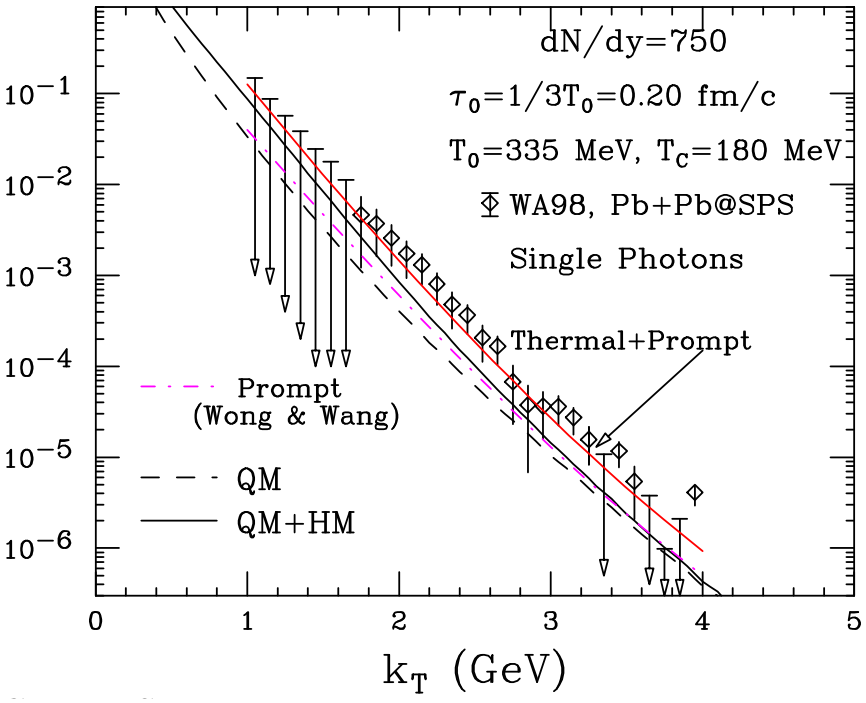

Figure 1.2: Plot of thermal and prompt photon emission rate from experiment [10] as a function of transverse momentum [23]. The data points stem from the WA98 collaboration at CERN SPS. QM indicates the contribution from thermal radiation of quark matter during a QGP and the mixed phase, see the dashed line. HM indicates the contribution from thermal radiation of hadronic matter during the mixed and the hadronic phase. The sum of the two are depicted by the solid black line. The contribution of prompt photons is displayed as the dashed-dotted curve. Finally, the total of thermal and prompt photons is shown by the solid red line.

only [7]. Then the background decay distribution is also calculated based on these radiative decays via a fit ansatz and finally, the difference between the measured and the calculated inclusive photon distribution is used to determine the excess of direct photon production [7]. For central collisions, a significant excess was found [7]. This excess is explained by the effect of annihilation with rescattering that can only occur in dense quark matter [9]. Because only the 10% most central collisions exhibit the direct photon excess and because the initial temperature at the CERN SPS collisions was not sufficiently high, the phenomenological analyses discussed above [19, 20, 22] could only state strong hints towards a formation of QGP for a short time period rather than conclusively showing evidence for QGP formation. But upon including the higher-order effects explained in Ref. [9], the observed excess could be attributed to QGP formation

[23].

The role of dileptons

Additionally, apart from photons, also dilepton pairs probe the complete space-time evolution of the medium created in a relativistic heavy-ion collision and do not suffer from final-state interactions with strongly interacting collision participants [24]. Therefore, measuring dileptons provides direct insight into the dynamics of the QGP. In the confined phase, the thermal dilepton production in the mass region below $1\,\mathrm{GeV}$ is mediated by the light vector mesons ρ, ω and ϕ [24]. The ρ with a mass of $770\,\mathrm{MeV}$ plays the dominant role as it strongly couples to the $\pi\pi$ channel and has a lifetime of about $1.3\,\mathrm{fm/c}$ which is short compared to the lifetime of the fireball (about $5\ldots10\,\mathrm{fm/c}$) [24]. Furthermore, dileptons can be utilized for probing reactions inside the nucleus as well as photon-nucleus reactions because the electrons emitted from the nucleus do not re-scatter within the nuclear matter via the strong interaction [25]. When a photon hits a nucleus inside the medium, the photon more likely interacts with the nucleons inside the nucleus that are facing towards the photon whereas the nucleons on the opposite side of the nucleus are less likely to interact with the photon through the vector channel [25]. This phenomenon is called shadowing and is addressed in Ref. [25] in order to accurately assess in-medium photon reactions.

Photon rate in heavy-ion collisions at the highest energies

When considering the photon production from relativistic heavy-ion collisions at RHIC or LHC energies, one has to take into account effects from jet formation and jet-quenching. In Ref. [26], the authors address the photon production due to jets from high-energy quarks traversing the QGP. Because the photon yield from quark jets depends on the density of the medium traversed by the quark, the photon yield may provide information about the medium's density [26]. Although the photon radiation by a fast quark in the medium due to Compton scattering off thermal gluons and annihilation with a thermal antiquark is of higher order in α_s (compared to prompt photons, e.g.), the contribution is not subleading and needs to be accounted for when describing the photon rate at RHIC or LHC energies [26].

In Ref. [27], the authors calculate the spectra of real and virtual photons including effects of jets in the medium at RHIC energies. Bremsstrahlung processes of jets in the medium radiating gluons and photons are addressed by several authors, e.g. [28, 16].

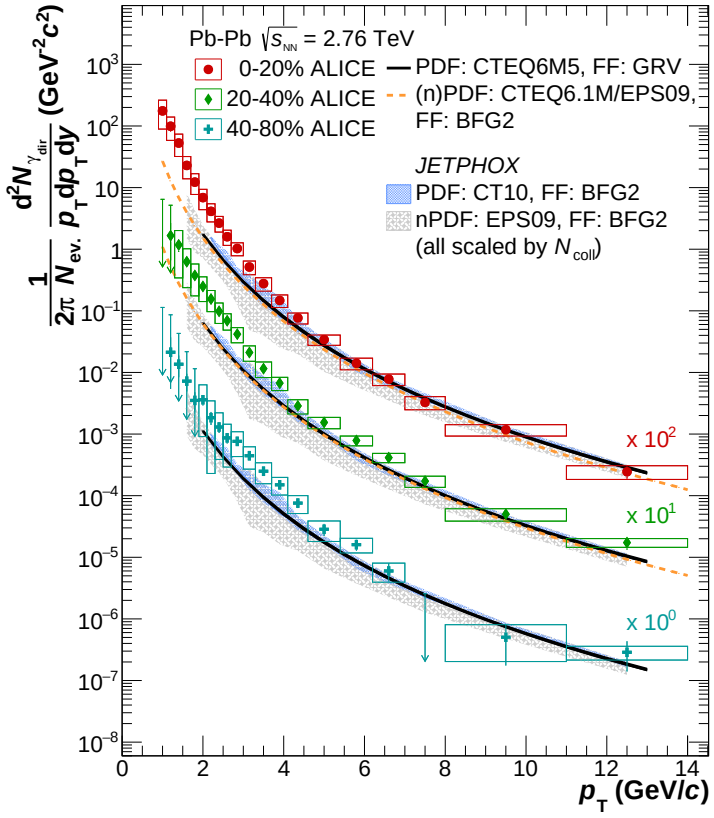

Figure 1.3: Plot of direct photon spectra as a function of transverse momentum from the ALICE collaboration at CERN for three centrality classes and a comparison to NLO predictions [29] and references therein. The data are well described by models assuming the formation of a QGP, see Ref. [29] for details.

The photon spectra measured by the ALICE collaboration in $Pb-Pb$ collisions at CERN [29] agree with perturbative QCD results and are well described by state-of-the-art models concluding the formation of a QGP. Fig. 1.3 shows the measured photon spectrum: Prompt direct photons dominate at high transverse momenta ($p_T \gtrsim 5\,\mathrm{GeV}$) while thermal direct photons dominate at lower transverse momenta ($p_T \lesssim 4\,\mathrm{GeV}$) and convey information about temperature, collective behavior and the space-time evolution of the QGP [29]. Additionally, direct photons are created when hard scattered partons interact with the medium, which is also known as jet-photon conversion [29]. This mechanism occurs mainly at transverse momenta $p_T \lesssim 10\,\mathrm{GeV}$ [29] and is dominated by Compton or annihilation processes of a fast quark with a thermal parton [16]. In their work [29], the ALICE collaboration finds that there is a correlation between the slope of direct photon spectra and the initial temperature which is, however, hard to extract, see [29].

The decay photons in the experiment originate predominantly from π^0, η and ω decays. Again, an excess photon yield is observed in mid-central and central collisions for transverse momenta below $p_T \sim 4\,\mathrm{GeV/c}$ connected to the production of thermal photons [29].

1.3 Connection to cosmology

On a cosmological scale, large anisotropies in the energy-momentum tensor can give rise to gravitational waves as was briefly mentioned in section 1.2. Additionally, momentum anisotropies are also studied in the context of dilepton production in the quark-gluon plasma. The spectral functions associated with dilepton and photon production also appear in cosmological calculations introducing sterile neutrinos, possible warm dark matter candidates. Finally, the epoch of formation and eventual dissolution of the QGP is embedded in a series of cosmological epochs that comprise the history of the universe.

In general, one can state that the comparison of the expansion (or Hubble) rate of the universe and the equilibration rate provides insight to cosmological phenomena [30]. The equation of state (EOS) of the matter that the universe consists of governs the expansion rate while the equilibration rate is determined by the physical interactions and processes experienced by a certain particle or excitation [30]. Typically, when the equilibration rate falls below the expansion rate, the relic of a certain epoch starts to form [30]. The cosmic microwave background, for instance, stems from the time of recombination when photons effectively ceased to interact with the rest of the matter in the universe [30].

Similar mechanisms take place in relativistic heavy-ion collisions: the expansion of the medium is governed by the EOS of QCD and microphysical processes determine the response and coupling of certain probes to the medium [30]. Due to this parallelism, developments in either field have sparked progress in the other, see Ref. [30] for details.

In the following, connections of the spectral function in the vector channel to sterile neutrinos as well as of anisotropies in the QGP to gravitational waves will be addressed.

Sterile neutrinos

One of the most important tasks of modern cosmology is to explain the apparent asymmetry of baryons over antibaryons. There are several scenarios that try and realize the Sakharov conditions for the baryon-antibaryon asymmetry [31]. One path is to ex-

tend the standard model by heavy right-handed Majorana neutrinos within leptogenesis scenarios [31, 32]. Because the Majorana neutrinos are unstable, they will decay into leptons and antileptons. And since the Sakharov conditions imply that CP symmetry be violated, the decay rates are different which results in an excess of antileptons over leptons. This then can generate a baryon over antibaryon excess via sphaleron interactions that conserve $B - L$, but not $B + L$ [31, 32]. It is interesting to note that the self-energy of the Majorana neutrinos has a similar form as the one for the production of photons.

Furthermore, it is convincingly evident from neutrino experiments that neutrinos have a small, yet detectable mass and that there are mixings between the three neutrino families [33]. In order to incorporate these phenomena into the minimal standard model (MSM) it is proposed that one add 3 sterile right-handed neutrinos to the MSM [33]. This is called the νMSM. The authors of Ref. [33] show that the extension by 3 sterile neutrinos is a natural choice if the sterile neutrinos are simultaneously required to act as possible warm dark matter candidates and to satisfy constraints from neutrino oscillation data. The main production mechanism of dark matter through oscillations between active and sterile neutrinos is explored in Ref. [33]. For the case of 3 additional sterile neutrinos, the νMSM might be testable by experiments dedicated to observing dark matter. In this way, the νMSM can be thought of as a very simple and "experimentally motivated extension of the MSM" [33]. In Ref. [34], the exact mechanism that leads to a baryon-antibaryon asymmetry within the νMSM is explained.

Once the νMSM is formulated, it is possible to derive the sterile neutrino production rate within it [35]. This rate, however, exhibits a peak for temperatures around the QCD crossover where strong interactions are dominant, and consequently perturbative approaches are not applicable [35]. Hence, the authors of Ref. [35] establish an analytic relation between the sterile neutrino production rate and the active neutrino spectral function. These spectral functions can be expressed in terms of flavor non-singlet vector as well as axial vector currents accessible via QCD [35]. The vector correlator is directly connected to the photon production rate (see also chapter 6). Therefore the spectral function that is associated with the vector correlator is not only relevant for the photon production rate, but also for the production of sterile neutrinos, i.e. possible candidates of warm dark matter particles as well as possible explanations for neutrino oscillations and the baryon-antibaryon asymmetry within leptogenesis scenarios.

The possibility of encompassing many beyond standard model phenomena such as neutrino masses, warm dark matter candidates, and the asymmetry between baryonic

and antibaryonic matter in the universe within one simple extension of the standard model by 3 right-handed sterile neutrinos has sparked very recent research activity, see e.g. Ref. [36], where the corresponding cosmological evolution equations are solved numerically. A lattice estimate for certain quantities such as rate coefficients occurring in the dark matter production would be a very valuable cross-check.

Gravitational waves

Similar to electromagnetic radiation being emitted by moving charges inside the QGP, when point masses are accelerated in the hot and dense medium, they act as sources for gravitational waves. While the photon radiation from the QGP is detectable, the very light masses and the comparably weak gravitational interaction cannot produce gravitational waves that are detectable by today's means.

One known and plausible mechanism for creating gravitational waves that are detectable consists in the strong perturbations out of equilibrium that could take place in the early universe as a consequence of a possible first order phase transition. When rapid and violent phenomena like a first order phase transition appear in the early universe, they can cause anisotropic fluctuations in the energy-momentum tensor which then give rise to detectable gravitational waves [37]. Phase transitions take place at a critical temperature T_* when the universe evolves from a symmetric phase with a temperature above T_* to a state of broken symmetry at a temperature below T_*.

In Ref. [37], a few models exhibiting a strong first order phase transition are reviewed. When a first order phase transition takes place, gravitational waves can be created both by bubble collisions and magnetohydrodynamical turbulence inside the primordial plasma because they constitute fluctuations in the energy-momentum tensor. Their gravitational wave spectra due to the phase transition are presented and compared to the sensitivity limits of experiments that are currently ongoing or planned. It is interesting to note that most of the models discussed in [37] introduce dark matter candidates. Thus, the search for gravitational wave signals is an endeavor complementary to the search for dark matter candidates already conducted at the LHC.

Axions

Apart from the photon production rate of the QGP, the quest for dark matter candidates is subject to ongoing research activities applying lattice quantum field theory in the field of early universe phenomena, see Ref. [38] as an example of motivating axions as dark

matter candidates. Progress in this direction heavily relies on the determination of the topological susceptibility (being connected to the axion's mass and decay constant as $\chi_{\text{top}} \sim m_a^2 f_a^2$ [38]) in the temperature range $T \sim 540\,\text{MeV} \ldots 1150\,\text{MeV}$ which constitutes a formidable task for the lattice community.

1.4 Quantum Chromodynamics

The standard model of elementary particle physics organizes three interactions and the corresponding particles sensitive to these interactions. They are called the electromagnetic, the weak and the strong interaction (or force). Quantum Electrodynamics (QED) is the quantum field theory describing the interaction of the electromagnetic force with leptonic degrees of freedom. When one extends the symmetry group of QED from $U(1)$ to $SU(2) \times U(1)$, it is possible to unify the electromagnetic and the weak forces within a single theory for which Xxxxxxx, Xxxxxxxx and Xxxxx received the Nobel prize in physics in 1979. The interaction of particles sensitive to the strong force is subsumed in the theory of Quantum Chromodynamics (QCD). There are six known so-called quarks, massive fermionic degrees of freedom that carry a color charge. The bosonic massless particles that mediate the color charge are called gluons.

	u	d	s	c	b	t
Q/e	$2/3$	$-1/3$	$-1/3$	$2/3$	$-1/3$	$2/3$
m	$2.2\,\text{MeV}$	$4.7\,\text{MeV}$	$95\,\text{MeV}$	$1.275\,\text{GeV}$	$4.18\,\text{GeV}$	$173\,\text{GeV}$

Table 1.1: The six quark flavors and their respective electromagnetic charges and masses. The masses are quoted in the $\overline{\text{MS}}$ scheme at scale $\mu = 2\,\text{GeV}$ from [39].

The Lagrangian density of QCD reads

$$\mathcal{L}_{\text{QCD}} = -\frac{1}{4}\,\text{Tr}\left[F^{\mu\nu}F_{\mu\nu}\right] + \sum_{f=1}^{N_f} \bar{\psi}_f \left(i\gamma^\mu D_\mu - m_f\right)\psi_f, \tag{1.1}$$

where the trace is taken over color indices. The Dirac γ-matrices are Hermitian unitary matrices and satisfy the anticommutation relation $\{\gamma_\mu, \gamma_\nu\} = 2\eta_{\mu\nu}$ where $\eta_{\mu\nu}$ is the mostly negative Minkowski metric $(+,-,-,-)$. The quark spinors ψ_f with their corresponding masses m_f come in $N_f = 6$ flavors as given in table 1.1 and $N_c = 3$ colors, the spinor and color indices are suppressed. The gluons appear in the covariant

derivative D_μ as the gauge fields A^a_μ,

$$D_\mu = \partial_\mu - ig\frac{\lambda^a}{2}A^a_\mu, \tag{1.2}$$

where a is the color index, g the QCD coupling constant and λ^a are the eight Gell-Mann matrices. The gluon fields A^a_μ transform in the adjoint representation. The field strength tensor for the gluons is given by

$$\begin{aligned} F^a_{\mu\nu} &= \partial_\mu A^a_\nu - \partial_\nu A^a_\mu + igf^{abc}A^b_\mu A^c_\nu & (1.3)\\ &= \frac{i}{g}\left[D_\mu, D_\nu\right] & (1.4)\end{aligned}$$

with f^{abc} the totally antisymmetric QCD structure constant. The third term in eq. (1.3) occurs because the underlying symmetry group of the Lagrangian density $SU(N_c)$ is non-Abelian. It gives rise to cubic and quartic gluon terms in the action that is $\sim F_{\mu\nu}F^{\mu\nu}$. This represents the fact that gluons have a color charge and hence self-interact. Due to the self-interaction of gluons the static quark-antiquark potential increases linearly for large distances. This feature is mirrored in the running of the QCD coupling constant α_s. It is small at short distances/large momentum scales, and large at large distances/low momentum scales:

$$\alpha_s^{-1}(Q^2) = \frac{33 - 2N_f}{12\pi}\log\left(\frac{Q^2}{\Lambda^2_{\mathrm{QCD}}}\right), \tag{1.5}$$

where $\Lambda^2_{\mathrm{QCD}} \approx 200 - 400\,\mathrm{MeV}$ and N_f is the number of quark flavors [3, 4]. A consequence of the former is *asymptotic freedom* [3, 4], whereas the latter leads to *color confinement* [40]: When a quark-antiquark pair is separated, the production of a second quark-antiquark pair between the original one may become energetically favorable as the potential energy between the original pair increases with distance. Thus, free quarks or gluons have never been observed in experiments. It seems that only composite objects with overall vanishing net color charge appear in nature. These color singlet states are called hadrons which come in two types, quark-antiquark pairs are called mesons and systems of three quarks or three antiquarks are called baryons or antibaryons, respectively. Recent experiments claim the observation of resonances that are consistent with pentaquark states [41] as well as the production of a possible candidate for a tetraquark state [42].

The running of the QCD coupling is determined by the renormalization group equation

$$\mu^2\frac{d\,\alpha_s}{d\,\mu^2} = \beta(\alpha_s) \tag{1.6}$$

at a given energy scale μ. The QCD β function can be computed in perturbation theory, see eqn. (3.3). It is negative at leading order which shows that QCD becomes asymptotically free at large couplings. While asymptotic freedom implies that perturbative calculations are applicable in the high energy sector of QCD, the low-energy sector, however, needs to be addressed by non-perturbative frameworks such as lattice QCD, briefly introduced in chapter 2, or effective models.

The hadronic phase where quarks are confined is accompanied by another thermodynamic phase of strongly interacting matter called the quark-gluon plasma (QGP) where quarks become deconfined within the medium and chiral symmetry is restored. This QGP phase is expected to have existed in the very early stages of the universe, about $10^{-5}\,\mathrm{sec}$, i.e. a couple of microseconds after the Big Bang. The QGP is subject of active ongoing experimental research conducted at particle accelerators such as the LHC or RHIC. The goal of the theoretical and experimental research endeavors regarding the QGP is, e.g., to understand the phase transiton between the hadronic and the QGP phases, particularly the physcial mechanisms involved in the formation of composite hadrons, as well as to understand the mere properties of the QGP itself. This work focuses on the investigation of questions related to the screening masses of in-medium excitations and to real-time properties of the QGP related to the photon production rate.

1.5 Symmetries of QCD

An essential aspect of examining the thermodynamic phases of a theory lies in understanding the symmetries of the system. In this section, the exact color gauge symmetry and the chiral symmetry of the QCD Lagrangian density are discussed. The presentation follows [43].

1.5.1 Color gauge symmetry

The color gauge transformations leaving the QCD Lagrangian (1.1) invariant, belong to the $SU(3)$ symmetry group. For a general $SU(N)$ group, there are N^2-1 generators. So in the case of $N = N_c = 3$, we see 8 generators represented by the eight Gell-Mann matrices λ_a in the fundamental representation. They correspond to eight gluons within QCD. In the continuum, the quarks transform in the fundamental representation of color $SU(3)$ whereas the gluons are in the adjoint representation. On the lattice, the

gauge fields are not elements of the algebra, but of the group.

1.5.2 Chiral symmetry

The fermionic part of the QCD action reads

$$S_F\left[\bar{\psi}, \psi, A\right] = \int \mathrm{d}^4x\, \bar{\psi}\left(i\gamma^\mu D_\mu - M\right)\psi, \tag{1.7}$$

where we omitted the flavor indices f and introduced a vector notation instead [43]. Then the mass matrix M takes the form $M = \mathrm{diag}\,(m_1, m_2, \ldots, m_{N_f})$. In the chiral limit ($M \equiv 0$), the action (1.7) is invariant under the N_f^2 vector transformations

$$\psi' = e^{i\alpha_i T_i}\,\psi, \qquad \bar{\psi}' = \bar{\psi}\, e^{-i\alpha_i T_i} \tag{1.8}$$

$$\psi' = e^{i\alpha}\,\psi, \qquad \bar{\psi}' = \bar{\psi}\, e^{-i\alpha}. \tag{1.9}$$

The symmetry under (1.9) still holds when the masses m_i are arbitrary, and the corresponding conserved Noether charge is the baryon number.

The axial vector or chiral rotations are given by

$$\psi' = e^{i\alpha_i\gamma_5 T_i}\,\psi, \qquad \bar{\psi}' = \bar{\psi}\, e^{i\alpha_i\gamma_5 T_i} \tag{1.10}$$

$$\psi' = e^{i\alpha\gamma_5}\,\psi, \qquad \bar{\psi}' = \bar{\psi}\, e^{i\alpha\gamma_5} \tag{1.11}$$

and the fermionic action (1.7) is invariant under those in the chiral limit. The left- and right-handed components of the spinor fields transform independently under $SU(N_f)$ transformations. So for the case of $M = 0$, the overall symmetry of the fermion QCD action is [43]

$$SU(N_f)_L \times SU(N_f)_R \times U(1)_V \times U(1)_A. \tag{1.12}$$

Albeit the action is invariant under $U(1)_A$, a chiral flavor singlet rotation like eqn. (1.11) introduces a symmetry breaking term, the topological charge, into the fermion integration measure of the QCD path integral [43]. This is the famous axial anomaly and the symmetry of massless QCD is reduced to

$$SU(N_f)_L \times SU(N_f)_R \times U(1)_V. \tag{1.13}$$

When one allows for nonvanishing, but degenerate masses, $M = \mathrm{diag}(m, m, \ldots, m)$, then $SU(N_f)_L \times SU(N_f)_R$ reduces to its subgroup $SU(N_f)_V$ because the left- and

right-handed fermions must be phase-rotated identically in order for the action to remain invariant. The remaining

$$SU(N_f)_V \times U(1)_V \tag{1.14}$$

does not survive when $M = \mathrm{diag}(m_u \neq m_d \neq m_s \neq \dots)$. One is left with

$$U(1)_V \times U(1)_V \times \cdots \times U(1)_V \tag{1.15}$$

with N_f factors corresponding to independent phase changes for each quark.

The small masses of the up and down quark introduce only a very small explicit chiral symmetry breaking and (1.13) would be an exact symmetry if the up and down quark were massless. As a consequence of the small explicit breaking due to the masses of the up and down quark, one would expect chiral symmetry to be reflected in the spectrum of hadron masses. This would, e.g., imply nearly degenerate masses of the ρ meson and its parity partner, the a_1 meson. The mass of ρ meson is given by $770\,\mathrm{MeV}$, the mass of the a_1, however, amounts to $1260\,\mathrm{MeV}$. This difference observed in nature for the masses of parity partners is too big to be explained by the explicit symmetry breaking of the up and down quark. It is the spontaneous symmetry breaking mechanism that gives rise to the huge mass difference.

In order to understand this for a classical analogue, one can consider a ferromagnetic spin system. The action of the system is invariant under $O(3)$ rotations of the spins. When one cools the system below its Curie temperature while an external magnetic field is present, all spins within the system will align along the external magnetic field. And even when there is no external magnetic field present, all spins will eventually point in the same direction in the ground state when we consider the system in the thermodynamic limit. The result is an overall (spontaneous) magnetization of the system and a spontaneous breaking of the $O(3)$ symmetry. In this example, the magnetization plays the role of an order parameter.

In QCD, the action is invariant under chiral rotations of the fields but the ground state of the theory is not. One can also say that chiral symmetry is hidden when one examines the ground state of QCD. The order parameter for chiral symmetry is called the chiral condensate

$$\langle \bar{\psi}\psi \rangle \,. \tag{1.16}$$

It transforms exactly like a mass term and mixes left- and right-handed components of the fermion fields. Thus, in the case of a vanishing chiral condensate, the system's

chiral symmetry is restored whereas chiral symmetry is spontaneously broken when the chiral condensate is non-zero.

1.6 Path integral quantization in Euclidean space-time

The general idea of Feynman's path integral formulation [44] is described in many standard textbooks. This section briefly sketches a few basic formulae and stresses the need for the Wick rotation.

The expectation value of an operator $\hat{O}$ in QCD is given by

$$\left\langle \hat{O} \right\rangle = \frac{1}{Z} \int \mathcal{D}[\bar{\psi}, \psi, A]\, O(\bar{\psi}, \psi, A)\, \exp\left(i S_{\mathrm{QCD}}\left[\bar{\psi}, \psi, A\right]\right) \tag{1.17}$$

where the partition function reads

$$Z = \int \mathcal{D}[\bar{\psi}, \psi, A]\, \exp\left(i S_{\mathrm{QCD}}\left[\bar{\psi}, \psi, A\right]\right) \tag{1.18}$$

and the QCD action

$$S_{\mathrm{QCD}}\left[\bar{\psi}, \psi, A\right] = \int \mathrm{d}^4 x\, \mathcal{L}_{\mathrm{QCD}} \tag{1.19}$$

with $\mathcal{L}_{\mathrm{QCD}}$ given by (1.1), is an integral over Minkowski space. The exponential in the integrand of (1.17) oscillates because its argument is imaginary. Hence, it cannot act as a weight factor for numerical simulations which require a real and positive factor. A way around this is the Wick rotation of real time t to imaginary time $\tau = ix^0$, $x^0 \in \mathbb{R}$. Then the expectation value is calculated by

$$\left\langle \hat{O} \right\rangle = \frac{1}{Z} \int \mathcal{D}[\bar{\psi}, \psi, A]\, O(\bar{\psi}, \psi, A)\, \exp\left(-S^E_{\mathrm{QCD}}\left[\bar{\psi}, \psi, A\right]\right) \tag{1.20}$$

with

$$S^E_{\mathrm{QCD}}\left[\bar{\psi}, \psi, A\right] = \int \mathrm{d}^4 x\, \mathcal{L}^E_{\mathrm{QCD}} \quad \text{and} \tag{1.21}$$

$$\mathcal{L}^E_{\mathrm{QCD}} = \frac{1}{4} \mathrm{Tr}\left[F_{\mu\nu} F_{\mu\nu}\right] + \sum_{f=1}^{N_f} \bar{\psi}_f \left(\gamma^E_\mu D_\mu + m_f\right) \psi_f \tag{1.22}$$

where the γ^E_μ are the Euclidean γ-matrices satisfying the anticommutation relation

$\{\gamma_\mu, \gamma_\nu\} = 2\delta_{\mu\nu}$. In the chiral representation, the Euclidean γ-matrices are given as

$$\gamma_0 = \begin{pmatrix} 0 & 0 & -1 & 0 \\ 0 & 0 & 0 & -1 \\ -1 & 0 & 0 & 0 \\ 0 & -1 & 0 & 0 \end{pmatrix}, \quad \gamma_1 = \begin{pmatrix} 0 & 0 & 0 & -i \\ 0 & 0 & -i & 0 \\ 0 & i & 0 & 0 \\ i & 0 & 0 & 0 \end{pmatrix}, \quad \gamma_2 = \begin{pmatrix} 0 & 0 & 0 & -1 \\ 0 & 0 & 1 & 0 \\ 0 & 1 & 0 & 0 \\ -1 & 0 & 0 & 0 \end{pmatrix},$$
$$\gamma_3 = \begin{pmatrix} 0 & 0 & -i & 0 \\ 0 & 0 & 0 & i \\ i & 0 & 0 & 0 \\ 0 & -i & 0 & 0 \end{pmatrix}, \quad \gamma_5 = \gamma_0\gamma_1\gamma_2\gamma_3 = \begin{pmatrix} 1 & 0 & 0 & 0 \\ 0 & 1 & 0 & 0 \\ 0 & 0 & -1 & 0 \\ 0 & 0 & 0 & -1 \end{pmatrix}. \tag{1.23}$$

Due to the gauge invariance of (1.20), one needs to apply a gauge fixing method, for example the one of Xxxxxxx and Xxxxx, otherwise (1.20) is divergent. As discussed in chapter 2, the lattice version of this integral is formulated using link variables that are members of the compact group $SU(3)$. Therefore and because the theory is formulated in a finite volume with a finite number of variables, the integral is finite even when one does not choose one gauge trajectory as favored gauge. Gauge-fixing methods on the lattice, however, do exist and can serve as a helpful tool for complex computations or renormalization procedures, for instance.

1.7 QCD at finite temperature

Bulk properties of hot and dense matter near and in equilibrium can be addressed by thermodynamics [45]. Quantities such as pressure or energy density are easily determined by applying the fundamental tools of thermodynamics. For a system where particles and energy can be exchanged with a reservoir, the grand canonical ensemble describes the statistical processes and is the best suited choice for describing the thermodynamics of relativistic heavy-ion collisions where particles can be created and destroyed. When such a system is described by the Hamiltonian H and a set of conserved number operators N_i (e.g. baryon number), then the statistical density matrix of this system is given by [45]

$$\hat{\rho} = \exp\left[\,\beta\left(H - \mu_i N_i\right)\right]. \tag{1.24}$$

The inverse temperature is indicated by $\beta = T^{-1}$ and μ_i are the chemical potentials related to the conserved number operators. Repeated indices are understood to be summed over. The statistical densitiy matrix $\hat{\rho}$, as it describes an ensemble of states, is

a crucial object in quantum statistics when one replaces the usual vacuum expectation value of any quantity A by its ensemble average [45]:

$$\bar{A} = \langle A \rangle = \frac{\mathrm{Tr}\, A\hat{\rho}}{\mathrm{Tr}\, \hat{\rho}}. \tag{1.25}$$

Then the grand canonical partition function is given by [45]

$$Z = \mathrm{Tr}\, \hat{\rho} = \mathrm{Tr}\, \exp\left[-\beta\left(H - \mu_i N_i\right)\right] \tag{1.26}$$

and can be used to determine the pressure or entropy of a system, i.e. [45]

$$\begin{aligned} P &= \frac{\partial\left(T \ln Z\right)}{\partial V}, \\ N_i &= \frac{\partial\left(T \ln Z\right)}{\partial \mu_i}, \\ S &= \frac{\partial\left(T \ln Z\right)}{\partial T}. \end{aligned} \tag{1.27}$$

One takes the logarithmic derivative because $\ln Z$ is the generating functional from which one can derive only connected propagators or Greens functions. Disconnected ones do not contribute to the T-matrix, hence one does not compute them in thermodynamics.

In order to describe relativistic systems and include Lorentz invariance, one needs to make the transition from states to fields. The partition function can then be expressed as [45]

$$Z = \mathrm{Tr}\, \exp\left[-\beta\left(H - \mu_i N_i\right)\right] = \sum_a \int \mathrm{d}\phi_\mathrm{a} \left\langle \phi_\mathrm{a} \right| \mathrm{e}^{-\beta(\mathrm{H} - \mu_\mathrm{i} \mathrm{N_i})} \left| \phi_\mathrm{a} \right\rangle, \tag{1.28}$$

where one has performed Wick rotation under the integral, $\tau = it$. The sum runs over all states a and one integrates over all fields ϕ_a. After Wick rotation, the upper integration bound for τ is given by the inverse temperature $1/T \equiv \beta$. Bosonic degrees of freedom obey periodic boundary conditions, fermionic degrees of freedom are subject to antiperiodic boundary conditions. The thermal Greens or correlation function is then given by [45]

$$G(x, y, \tau_1, \tau_2) = Z^{-1}\, \mathrm{Tr}\left\{\hat{\rho}\, T_\tau\left[\phi(x, \tau_1)\phi(y, \tau_2)\right]\right\}, \tag{1.29}$$

where T_τ denotes the time ordering operator. The fields ϕ can be Fourier transformed as [45]

$$\phi(x, \tau) = \frac{1}{\sqrt{\beta}} \sum_n \sum_{\mathbf{p}} e^{i(\mathbf{p}\cdot\mathbf{x} + \omega_n \tau)} \phi_n(\mathbf{p}) \tag{1.30}$$

with the so called Matsubara frequencies $\omega_n = 2\pi n/\beta$ for bosons with periodic and $\omega_n = (2n+1)\pi/\beta$ for fermions with antiperiodic boundary conditions.

The following depiction follows Ref. [46].

At finite temperature, one can define the Wightman correlators as [46]

$$\begin{aligned} G_{>}^{AB}(t) &\equiv \mathrm{Tr}\,\{\hat{\rho}\, A(t)B(0)\}, \\ G_{<}^{AB}(t) &\equiv \mathrm{Tr}\,\{\hat{\rho}\, B(0)A(t)\}. \end{aligned} \tag{1.31}$$

The Euclidean correlator which is calculated within lattice QCD (see chapter 2), is related to these by

$$G_{\mathrm{E}}^{AB}(t) = G_{>}^{AB}(-it). \tag{1.32}$$

The expectation value of the commutator is given as

$$G^{AB}(t) = i\,\mathrm{Tr}\,\{\hat{\rho}\,[A(t), B(0)]\} = i(G_{>}^{AB}(t) - G_{<}^{AB}(t)) \tag{1.33}$$

and is identically zero outside the light cone due to the causality of the theory. The spectral function is then obtained by Fourier transformation of the commutator,

$$\rho^{AB}(\omega) = \frac{1}{2\pi i}\int_{-\infty}^{\infty} \mathrm{d}t\, e^{i\omega t} G^{AB}(t), \tag{1.34}$$

while integration over the positive half-axis yields the retarded correlator,

$$G_{\mathrm{R}}^{AB}(\omega) = \int_{0}^{\infty} \mathrm{d}t\, e^{i\omega t} G^{AB}(t). \tag{1.35}$$

The retarded correlator is a key figure of linear response theory which deals with the response of a medium to small and adiabatic perturbations out of equilibrium [46]. In the case of $B = A^{\dagger}$, the retarded correlator relates to the spectral function via

$$\rho^{AA^{\dagger}}(\omega) = \frac{1}{\pi}\mathrm{Im}\, G_{\mathrm{R}}^{AA^{\dagger}}(\omega). \tag{1.36}$$

Furthermore, the retarded correlator can be analytically continued to the frequency-space Euclidean correlator which proves very useful for lattice QCD calculations, and as an important conclusion, we can relate the configuration-space Euclidean correlator to the spectral function by [46]

$$G_{\mathrm{E}}^{AA^{\dagger}}(t) = \int_{-\infty}^{\infty} \mathrm{d}\omega\, \rho^{AA^{\dagger}}(\omega) \frac{\cosh(\omega(\beta/2 - t))}{\sinh(\beta\omega/2)}. \tag{1.37}$$

Further discussion on the relation of spectral functions and Euclidean as well as retarded correlators can be found in section 6.1. How to extract transport properties from these objects is briefly sketched in section 6.3.

Chapter 2

Lattice QCD

This chapter is based on the discussion in [43]. According to Ref. [43], the quantization of a system by a path integral over classical fields follows four steps:

- Continuous space-time is replaced by a Euclidean lattice in four dimensions with lattice spacing a. The classical fields Φ defined on the lattice now comprise the role of degrees of freedom of the system.
- One reformulates the lattice version of the Euclidean action $S_E[\Phi]$ in such a way that it reaches the continuum Euclidean action for $a \to 0$.
- The operators inserted into the Euclidean correlators of interest are translated into functionals whereby one uses the classical field variables instead of the field operators.
- After generating a lattice field configuration, the Euclidean correlators are computed by measuring the functionals on the configuration. One has to integrate over all possible field configurations, the weight is given by the Boltzmann factor $\exp\left(-S_E[\Phi]\right)$.

2.1 QCD on the lattice

The first step towards a lattice formulation of QCD is to discretize the Euclidean continuous space-time by introducing a four-dimensional Euclidean lattice

$$\Lambda = \left\{ x_\mu \in \mathbb{R}^4 \,|\, x_\mu = a\, n_\mu;\; n_0 = 0, 1, \ldots, N_t - 1;\; n_i = 0, 1, \ldots, N_s - 1 \right\} \qquad (2.1)$$

where a denotes the lattice spacing[1]. The lattice Λ extends to the finite spatial volume $V_3 = (N_s\, a)^3$ with the temporal extent being $\beta = N_t\, a$. For lattice ensembles at finite temperature T, the temporal extent is identified with the inverse temperature via

$$\beta \equiv \frac{1}{T} = N_t\, a. \tag{2.2}$$

The continuum limit $a \to 0$ and $V_3 \to \infty$ is necessary for providing results that are physically meaningful.

The fermionic degrees of freedom are represented by spinors that are defined on the lattice sites only

$$\psi(n),\, \bar{\psi}(n) \tag{2.3}$$

with $n \equiv n_\mu \in \Lambda$. For convenience, only the coordinate n_μ is used rather than the full physical vector x_μ. Consider the free fermionic action in the continuum

$$S_F^{\text{free}}[\psi, \bar{\psi}] = \int \mathrm{d}^4x\, \bar{\psi}(x)(\gamma_\mu \partial_\mu + m)\psi(x). \tag{2.4}$$

The discretization of the integral is realized as a sum over Λ whereas the derivative can be written as

$$\partial_\mu \psi(n) \to \frac{1}{2a}(\psi(n+\hat{\mu}) - \psi(n-\hat{\mu})) \tag{2.5}$$

where $\hat{\mu}$ denotes a unit vector on the lattice in μ direction. Then the free fermionic part of the Euclidean lattice QCD action reads

$$S_F^{\text{free}}[\psi, \bar{\psi}] = a^4 \sum_{n\in\Lambda} \bar{\psi}(n) \left(\sum_{\mu=1}^{4} \gamma_\mu \frac{(\psi(n+\hat{\mu}) - \psi(n-\hat{\mu})}{2a} + m\psi(n) \right). \tag{2.6}$$

Just as in the continuum case, where gauge fields are needed for the invariance of the action under $SU(3)$ rotations in color space, it is necessary to introduce gauge fields defined as link variables on the lattice. Consider the transformations of the fermion spinors

$$\psi'(n) = \Omega(n)\psi(n),\, \bar{\psi}'(n) = \bar{\psi}(n)\Omega^\dagger(n) \tag{2.7}$$

with $\Omega(n) \in SU(3)$. On the right hand side of Eq. (2.6) there will be terms such as $\bar{\psi}(n)\psi(n+\hat{\mu})$. But they transform as

$$\bar{\psi}'(n)\psi'(n+\hat{\mu}) = \bar{\psi}'(n)\Omega^\dagger(n)\Omega(n+\hat{\mu})\psi(n+\hat{\mu}), \tag{2.8}$$

[1]Throughout this work only isotropic lattices were considered, i.e. the lattice spacings in all spatial and the temporal direction are equal and all spatial extents of the lattice are equal.

which is not gauge invariant. To the end of making the fermionic action gauge invariant let us now introduce a field $U_\mu(n)$ as *link variable* that is attached to the link of the lattice Λ and points from n to $n+\hat{\mu}$. It is not part of the algebra but actually an element of the group $SU(3)$. Thus, if we require its transformation property to be

$$\begin{aligned} U'_\mu(n) &= \Omega(n)U_\mu(n)\Omega^\dagger(n+\hat{\mu}), \\ U'^\dagger_\mu(n) &= \Omega(n+\hat{\mu})U^\dagger_\mu(n)\Omega^\dagger(n+\hat{\mu}), \end{aligned} \tag{2.9}$$

then the modified term

$$\begin{aligned} \bar{\psi}'(n)U'_\mu(n)\psi'(n+\hat{\mu}) &= \bar{\psi}(n)\Omega^\dagger(n)\Omega(n)U_\mu(n)\Omega^\dagger(n+\hat{\mu})\Omega(n+\hat{\mu})\psi(n+\hat{\mu}) \\ &= \bar{\psi}(n)U_\mu(n)\psi(n+\hat{\mu}) \end{aligned} \tag{2.10}$$

is gauge invariant. Thus, we can also modify (2.6) and introduce the naive fermion action

$$\begin{aligned} S_F[\psi,\bar{\psi},U] &= a^4\sum_{n\in\Lambda}\bar{\psi}(n)\left(\sum_{\mu=1}^{4}\gamma_\mu\frac{U_\mu(n)\psi(n+\hat{\mu})-U^\dagger_\mu(n-\hat{\mu})\psi(n-\hat{\mu})}{2a}+m\psi(n)\right) \\ &\equiv a^4\sum_{n\in\Lambda}\bar{\psi}(n)D\psi(n) \end{aligned} \tag{2.11}$$

which satisfies $S_F[\psi',\bar{\psi}',U'] = S_F[\psi,\bar{\psi},U]$ under gauge transformations. This holds true for $N_f = 1$. But dressing the spinors as well as the mass term with a flavor label $(\bar{\psi}_f,\psi_f,m_f)$ and summing over the number of flavors generalizes this expression in a straightforward fashion. In the second line of eq. (2.11), we have introduced the naive lattice Dirac operator. This can be done because the action is bilinear in the quark fields. It is important to note that the link variable $U_\mu(n)$ is intrinsically connected to a gauge transporter known from continuum field theory. The resemblance is easily seen when defining

$$U_\mu(n) \equiv \exp(iaA_\mu(n)) \tag{2.12}$$

with $A_\mu(n)$ being the lattice version of gauge fields defined in the Lie algebra of $su(3)$. In Ref. [43], it is shown that the Euclidean version of the fermion action (1.7) is indeed recovered from (2.11) in the continuum limit $a \to 0$.

The gluon action is discretized on the lattice employing the *plaquette* variable (see fig. 2.1)

$$U_{\mu\nu}(n) \equiv U_\mu(n)\,U_\nu(n+\hat{\mu})\,U^\dagger_\mu(n+\hat{\nu})\,U^\dagger_\nu(n). \tag{2.13}$$

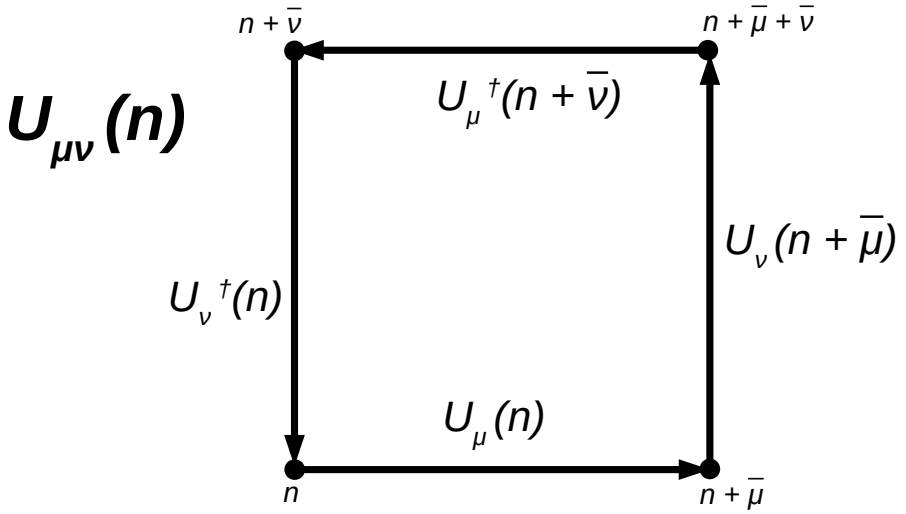

Figure 2.1: Schematic depiction of the plaquette $U_{\mu\nu}(n)$ in the $(\hat{\mu}-\hat{\nu})$ plane representing the smallest closed loop of four link variables. Here $\bar{\mu} = \hat{\mu}$ and $\bar{\nu} = \hat{\nu}$ are unit vectors on the lattice in $\hat{\mu}$ and $\hat{\nu}$ directions, respectively.

It is the smallest, nontrivial closed loop of link variables on the lattice [43]. We use $U^{\dagger}_{\mu}(n-\hat{\mu}) = U_{-\mu}(n)$. It can easily be shown that the trace of the plaquette is gauge invariant because (using (2.13) and (2.9))

$$\begin{aligned} \mathrm{Tr}\left[U'_{\mu\nu}(n)\right] &= \mathrm{Tr}\left[\Omega(n)U_{\mu\nu}(n)\Omega^{\dagger}(n)\right] \\ &= \mathrm{Tr}\left[U_{\mu\nu}(n)\right]. \end{aligned} \tag{2.14}$$

Following Wilson's idea [47], one can represent the gluon action by the sum over all plaquettes on the lattice, in particular

$$S_G[U] = \frac{2}{g^2}\sum_{n\in\Lambda}\sum_{\mu<\nu}\mathrm{Re}\,\mathrm{Tr}\left[1 - U_{\mu\nu}(n)\right]. \tag{2.15}$$

One may insert the representation (2.12) for the link variables into (2.13) and rewrite the product of exponentials of matrices in (2.15) with the help of the Baker-Campbell-Hausdorff formula. Then, after applying a Taylor expansion of the gauge fields

$$A_{\nu}(n+\hat{\mu}) = A_{\nu}(n) + a\,\partial_{\mu}A_{\nu}(n) + \mathcal{O}(a^2), \tag{2.16}$$

one can find

$$\begin{aligned} U_{\mu\nu}(n) &= \exp\left\{ia^2\left(\partial_{\mu}A_{\nu}(n) - \partial_{\nu}A_{\mu}(n) + i\left[A_{\mu}(n), A_{\nu}(n)\right]\right) + \mathcal{O}(a^3)\right\} \\ &= \exp\left\{ia^2F_{\mu\nu}(n) + \mathcal{O}(a^3)\right\}. \end{aligned} \tag{2.17}$$

For the second line of (2.17) one uses the Euclidean version of the continuum field strength tensor, see also (1.3). Inserting (2.17) into (2.15) and expanding the exponential yields

$$\begin{aligned} S_G[U] &= \frac{2}{g^2}\sum_{n\in\Lambda}\sum_{\mu<\nu}\mathrm{Re}\,\mathrm{Tr}\,[1-U_{\mu\nu}(n)] \\ &= \frac{a^4}{2g^2}\sum_{n\in\Lambda}\sum_{\mu<\nu}\mathrm{Tr}\left[F_{\mu\nu}(n)^2\right]+\mathcal{O}(a^2). \end{aligned} \tag{2.18}$$

Thus, the plaquette action recovers the Euclidean version of $F_{\mu\nu}F^{\mu\nu}$ present in the gluonic part of the QCD action up to terms of $\mathcal{O}(a^2)$. In the continuum limit $a\to 0$, $a^4\sum_{n\in\Lambda}$ corresponds to the integral over space-time. And therefore, one can recover the continuum version of the gluon action from (2.18). One may remark, however, that there are infinitely many more such lattice actions that recover the continuum gluon action in the naive continuum limit. The Wilson plaquette action is just the simplest one [48].

In eq. (2.11), we have introduced the naive lattice Dirac operator. For trivial gauge where all link variables U_μ are set to the identity matrix (that corresponds to all gauge fields A_μ being set to zero, i.e. the case of free fermions), one can perform a Fourier transform of the naive Dirac operator, yielding

$$\tilde{D}(p) = m + \frac{i}{a}\sum_{\mu=1}^{4}\gamma_\mu \sin(p_\mu a). \tag{2.19}$$

For the construction of the quark propagator, one needs to invert the Dirac operator in coordinate space. Since it is diagonal in momentum space, one can simply invert $\tilde{D}(p)$ and Fourier transform it back to coordinate space. The inverse reads

$$\tilde{D}(p)^{-1} = \frac{m - ia^{-1}\sum_\mu \gamma_\mu \sin(p_\mu a)}{m^2 + a^{-2}\sum_\mu \sin(p_\mu a)^2}. \tag{2.20}$$

For the case of free massless fermions, the solution (2.20) has 16 poles within the first Brillouin zone of the lattice and 15 of them are unphysical. Therefore, Wilson introduced a term to the Dirac operator to deal with this so-called doubling problem:

$$\tilde{D}^W(p) = m + \frac{i}{a}\sum_{\mu=1}^{4}\gamma_\mu \sin(p_\mu a) + \frac{1}{a}\sum_{\mu=1}^{4}(1-\cos(p_\mu a)). \tag{2.21}$$

At the physical pole $p_\mu = (0,0,0,0)$, the additional *Wilson term* vanishes, but it introduces a factor $2/a$ for each pole π/a at the edges of the Brillouin zone:

$$\tilde{D}^W(p) \overset{p_\mu=\text{pole}}{=} m + \frac{2l}{a} \overset{a\to 0}{\to} \infty, \tag{2.22}$$

where l counts the number of unphysical poles, which sends the mass of the doublers to infinity in the naive continuum limit such that they decouple from the theory. In the limit of massless fermions, the inverse Wilson Dirac operator is given as

$$\left[\tilde{D}^W(p)\right]^{-1} = a \cdot \frac{\sum_\mu (1-\cos(p_\mu a)) - i\sum_\mu \gamma_\mu \sin(p_\mu a)}{\left[\sum_\mu (1-\cos(p_\mu a))\right]^2 + \sum_\mu \sin(p_\mu a)^2} \tag{2.23}$$

which shows clearly that only the physical pole at $p_\mu = (0,0,0,0)$ remains whereas all the unphysical doublers vanish. In position space, the Wilson term corresponds to a lattice discretization of the Laplace operator. Taking this into account, the Wilson fermion action is then given by (employing the common notation of $\gamma_{-\mu} \equiv -\gamma_\mu$)

$$S_F^W[\psi,\bar{\psi},U] = \sum_{f=1}^{N_f} a^4 \sum_{n\in\Lambda} \bar{\psi}_f(n) \left\{ \left(m_f + \frac{4}{a}\right)\psi(n) - \frac{1}{2a}\sum_{\mu=\pm1}^{\pm4} (1-\gamma_\mu) U_\mu(n)\,\psi(n+\hat{\mu}) \right\}. \tag{2.24}$$

Thus, the Wilson Dirac operator enables a formulation of lattice QCD with dynamical fermions without doublers which reproduces the correct continuum limit. There is a fly in the ointment, however. The Wilson term breaks chiral symmetry explicitly. Moreover, the famous theorem by Nielsen and Ninomiya states that, on the lattice, the action cannot be free of fermion doublers and simultaneously preserve chiral symmetry in the form of

$$\gamma_5\, D\, \gamma_5 = -D \tag{2.25}$$

which states that the Dirac operator anti-commutes with γ_5. The Ginsparg-Wilson equation led to a solution of this problem and the result was the introduction of the overlap Dirac operator as one solution of the Ginsparg-Wilson equation for chiral fermions without doublers. Nonetheless, almost all Dirac operators obey γ_5-hermiticity, i.e.

$$\gamma_5\, D\, \gamma_5 = D^\dagger. \tag{2.26}$$

This has a remarkable consequence on the spectrum of the Dirac operator: the eigenvalues are either real or appear as complex conjugate pairs. This implies that the fermion determinant is real which is a crucial property for the feasibility of Monte Carlo simulations. Furthermore, one can show that the Dirac operator has zero modes (eigenmodes with vanishing eigenvalue) which come with positive or negative chirality, they are right- or left-handed, respectively. The difference $n_- - n_+$ of the number of left- and the number of right-handed zero modes counts the so called topological charge of a gauge

field. When one conducts certain computations only on gauge configurations with the same topological charge, one sticks to one specific topological sector. This technique underlies one method to compute the chiral condensate on the lattice which involves at first an infinite volume limit as well as a chiral limit afterwards. When including Wilson fermions the chiral symmetry may be broken but the spectrum is $\mathcal{O}(a)$ improved. One would expect that the chiral condensate $\langle\bar{\psi}\psi\rangle$ vanishes. But for a finite lattice spacing $a > 0$, a residual mass always remains although one may work in the chiral limit. Even the masses extracted from the vector and the axial vector correlators should be degenerate above the chiral critical temperature but there are $\mathcal{O}(a)$ violations. These violations can be overcome by a continuum extrapolation.

The full QCD lattice action with Wilson fermions is thus expressed as

$$S[\psi,\bar{\psi},U] = S_G[U] + S_F^W[\psi,\bar{\psi},U] \tag{2.27}$$

with $S_G[U]$ given by (2.15) and $S_F^W[\psi,\bar{\psi},U]$ by (2.24). The vacuum expectation value of an observable O then reads

$$\langle O\rangle = \frac{1}{Z}\int \mathcal{D}[\psi,\bar{\psi}]\,\mathcal{D}[U]\exp\left(-S[\psi,\bar{\psi},U]\right)\; O[\psi,\bar{\psi},U] \tag{2.28}$$

where the partition function is given as

$$Z = \int \mathcal{D}[\psi,\bar{\psi}]\,\mathcal{D}[U]\exp\left(-S[\psi,\bar{\psi},U]\right). \tag{2.29}$$

The measure of the gauge links

$$\mathcal{D}[U] = \prod_{n\in\Lambda}\prod_{\mu=1}^{4}\mathrm{d}U_\mu(n) \tag{2.30}$$

is called the Haar measure, and for

$$\mathcal{D}[\psi,\bar{\psi}] = \prod_{n\in\Lambda}\prod_{f}\mathrm{d}\psi_f\,\mathrm{d}\bar{\psi}_f \tag{2.31}$$

the rules of Grassmann integration apply because the fermion fields are realized as Grassmann numbers.

For the calculation of 2-point functions one needs to evaluate fermionic expectation values. Wick's theorem for Grassmann algebra implies that the inverse of the Dirac operator yields these expectation values. It is convenient to rewrite the inverse Wilson Dirac operator and expand it for large quark mass, resulting in the hopping parameter representation

$$D^{-1} = \sum_{n=0}^{\infty}\kappa_f^n H^n = \frac{1}{1-\kappa_f H} \tag{2.32}$$

such that the Dirac operator D and the hopping parameter are given as

$$D = 1 - \kappa_f H, \quad \kappa_f = \frac{1}{2am_{b,f} + 8} \tag{2.33}$$

where the hopping parameter κ_f is connected to the bare quark mass $m_{b,f}$ of flavor f and can be used in lattice simulation to tune the bare quark mass of the dynamical fermions. The series (2.32) converges if $\kappa||H|| < 1$. It can be shown that $||H|| \leq 8$, that means that the convergence of (2.32) is secured for $\kappa < 1/8$. The hopping matrix H collects nearest-neighbor terms of the Dirac matrix and establishes quark propagation as paths of link variables and the fermion determinant $\det[D] = \det[1 - \kappa H]$ can be shown to be gauge invariant [43].

The explicit breaking of chiral symmetry on the lattice leads to a mass shift m_c which depends on the lattice spacing and is generated dynamically by the term proportional to $\sim \bar{\psi}_f(n)U_\mu(n)\psi_f(n+\hat{\mu})$ in (2.24). It is not known *a priori* by how much the bare quark mass is shifted such that one has to measure m_c along the way during the simulation. Relating the mass shift to the hopping parameter, one finds a critical hopping parameter κ_c and the bare subtracted quark mass is then given as

$$\overline{m}_f = m_{b,f} - m_c = \frac{1}{2a}\left(\frac{1}{\kappa_f} - \frac{1}{\kappa_c}\right). \tag{2.34}$$

In the non-interacting theory, $\kappa_c = 1/8$. The Wilson term gives rise to cutoff effects of $\mathcal{O}(a)$. This is a lattice artifact which can be dealt with by a new term discussed in the next section.

2.2 Lattice artifacts and Symanzik improvement

In general, lattice artifacts come in three varieties:

- Finite size effects: Because the four-dimensional lattice box fills a finite volume, all results from lattice QCD are affected. The effect drops in in the infrared regime at low energies and the leading contribution to spectral properties stems from the lightest hadron mass, the pion mass M_π, proportional to $\mathcal{O}(e^{-M_\pi L})$: A rule of thumb suggests that one can neglect finite size corrections when one stays in the regime where $M_\pi L > 4$.

- Cutoff effects: This is the most striking error source for lattice calculations. Cutoff effects are present in the ultraviolet regime $\sim \frac{1}{a}$. A lattice spacing $a > 0$ acts as

a regularization of QCD (with the highest momentum projected onto a correlator being $\sim \frac{\pi}{a}$). Thus, all quantities measured on the lattice exhibit corrections that depend on a. Simply setting $a \to 0$ is not possible unless one also cranks up the number of lattice sites towards infinity. This increases the numerical cost and hence, one has to be content with a continuum extrapolation. Nonetheless, the improvement of the fermion action reduces the dependence of observables on the lattice action. This is achieved by the Symanzik improvement program.

- Chiral extrapolation: Usually, lattice caluclations are performed for unpysically high quark masses which makes numerical calculations much cheaper. If one is interested in the extrapolation of the results towards physical quark masses, one needs to apply chiral perturbation theory to provide guidance.

The key idea behind Symanzik improvement exploits the fact that one may add terms to the action that are of higher dimension and thus, vanish in the continuum limit. As a start, one comes up with an effective action

$$S_{\text{eff}} = \int \mathrm{d}^4x \left(L^{(0)}(x) + aL^{(1)}(x) + a^2 L^{(2)}(x) + \dots \right) \tag{2.35}$$

where $L^{(0)}$ is the usual QCD Lagrangian (1.1) and the other terms are ordered according to their dimension: With S_{eff} being dimensionless, all terms $L^{(k)}$ are of dimension $4+k$. When one adds discretized versions of the correction terms $L^{(k)}$ to the original action with the appropriate coefficients, one attains improvement to order $\mathcal{O}(a^k)$, i.e. all discretization effects of $\mathcal{O}(a^k)$ are gone. One requires that all additional terms still obey the original symmetries of $L^{(0)}$. For the case of QCD, it is possible to show that only linear combinations of five different dimension-5 operators may enter $L^{(1)}$. With the help of the field equations one can see that two of them are not actually linearly independent. And one can even eliminate two more terms by absorbing them in the bare mass and the bare coupling. Then what is left, is the so called Pauli term

$$L_1^{(1)}(x) = \bar{\psi}(x)\sigma_{\mu\nu}F_{\mu\nu}\psi(x) \tag{2.36}$$

where $\sigma_{\mu\nu} = [\gamma_\mu, \gamma_\nu]/2i$. The $\mathcal{O}(a)$ improved action then reads

$$S_F^{W,\text{imp}}[\psi, \bar{\psi}, U] = S_F^W[\psi, \bar{\psi}, U] + c_{SW} a^5 \sum_{n\in\Lambda} \sum_{\mu<\nu} \bar{\psi}(n) \frac{1}{2} \sigma_{\mu\nu} F_{\mu\nu}(n) \psi(n) \tag{2.37}$$

with the Sheikholeslami-Wohlert term c_{SW} that has to be tuned according to the lattice spacing one is working at. A suitable choice of discretizing the field strength tensor is

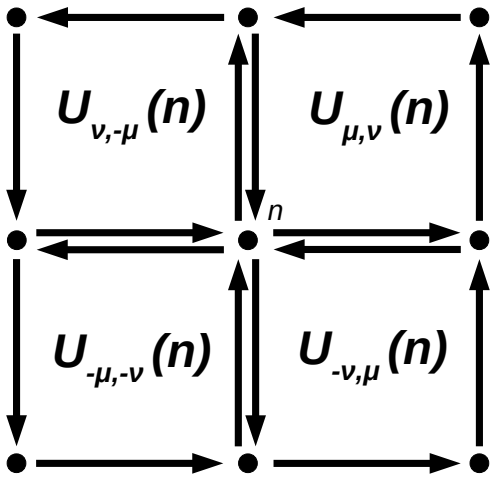

Figure 2.2: Schematic depiction of the clover term $Q_{\mu\nu}(n)$ in the $(\hat{\mu} - \hat{\nu})$ plane.

expressed by

$$F_{\mu\nu}(n) = \frac{-i}{8a^2}\left(Q_{\mu\nu} - Q_{\nu\mu}\right) \tag{2.38}$$

where $Q_{\mu\nu}$ stands for a sum of plaquettes $U_{\mu\nu}$ called the clover term (see fig. 2.2)

$$Q_{\mu\nu}(n) = U_{\mu,\nu}(n) + U_{\nu,-\mu}(n) + U_{-\mu,-\nu}(n) + U_{-\nu,\mu}(n). \tag{2.39}$$

The tuning of c_{SW} is done non-perturbatively and c_{SW} is expressed as a Padé ratio, see chapter 3.

Not only the action, but also the correlators need to be improved. The most important local operators that enter the expectation values of interest for this work are given as the pseudoscalar density, the vector current and the axial vector current, respectively:

$$\begin{aligned} P^a(x) &= \bar{\psi}(x)\,\gamma_5\,\frac{\tau^a}{2}\,\psi(x) \\ V^a_\mu(x) &= \bar{\psi}(x)\,\gamma_\mu\,\frac{\tau^a}{2}\,\psi(x) \\ A^a_\mu(x) &= \bar{\psi}(x)\,\gamma_5\,\gamma_\mu\,\frac{\tau^a}{2}\,\psi(x), \end{aligned} \tag{2.40}$$

where the τ^a are the two-dimensional Pauli matrices. The pseudoscalar density is already free of lattice artifacts to $\mathcal{O}(a)$. Along the lines of the Symanzik improvement program, one identifies the correction terms for the improved currents as

$$V^{a,\mathrm{imp}}_\mu(x) = V^a_\mu(x) + a c_V \partial_\nu T^a_{\mu\nu}(x) \tag{2.41}$$

$$A^{a,\mathrm{imp}}_\mu(x) = A^a_\mu(x) + a c_A \partial_\mu P^a(x). \tag{2.42}$$

In this case, ∂_μ denotes the symmetric version of the lattice derivative which is free of $\mathcal{O}(a)$ artifacts and $T^a_{\mu\nu} = i\bar{\psi}(x)\sigma_{\mu\nu}\frac{\tau^a}{2}\psi(x)$ is the tensor current. Just like the clover term c_{SW}, the coefficients c_A and c_V need to be tuned in a suitable fashion. For further information, the inclined reader is referred to the literature. The key ingredient for determining improvement coefficients non-perturbatively is the exploitation of *Ward-Takahashi identities*. They also play a role for the renormalization of lattice quantities.

2.3 Renormalization and scale setting

On the lattice, all quantities such as the action or observables are given as dimensionless objects. Only once one relates them to physical quantities, one establishes the determination of the lattice spacing a in physical units. An example is the dimensionless quantitiy $a\,m$: after identifying m with some physical mass (usually the mass of a hadron such as the pion), one obtains a in physical units. An outdated way of setting the scale is through the Sommer parameter r_0 which is extracted from the lattice calculation of the static quark-antiquark potential and assumes the physical value of $r_0 \approx 0.5\,\mathrm{fm}$.

The parameters that enter the lattice action such as the coupling constant g or the quark masses m_f are actually only *bare* parameters. They do not amount to the actual values of physical quantities observed in experiments. In order to establish the connection between bare parameters and the corresponding physical objects, one needs to compute lattice observables such as hadron masses, for example, and identify them with the physical parameters in the continuum. This task is rather complicated. There are, for example, various implementations of lattice actions, the derivatives may differ, the lattice grid itself can have different structures. Nonetheless, all these differences must vanish once one reaches the continuum limit $a \to 0$ and the observables should become independent of the lattice spacing. All of this means that the way bare parameters depend on the lattice spacing, must be given by nontrivial functions - $g(a)$ and $m_f(a)$, for instance. The renormalization group takes care of this *running* of the bare parameters and ensures one uses the correct values of the bare parameters for the given lattice structure. And finally, the Callan-Symanzik equation expresses the requirement that physics stays constant while changing the scale with the lattice parameter a. As an example, consider the pysical observable $P(m_f(a), g(a), a)$ defined on the lattice that

assumes the physical continuum value P_0 as one lets a go to 0:

$$\lim_{a\to 0} P(m_f(a), g(a), a) = P_0. \tag{2.43}$$

Then the Callan-Symanzik equation reads

$$\begin{aligned}
\frac{dP(m_f(a), g(a), a)}{d\ln a} &= \left(\frac{\partial}{\partial \ln a} + \frac{\partial g}{\partial \ln a}\frac{\partial}{\partial g} + \frac{\partial m_f}{\partial \ln a}\frac{\partial}{\partial m_f}\right) P(m_f(a), g(a), a) \\
&= \left(\frac{\partial}{\partial \ln a} - \beta(g)\frac{\partial}{\partial g} + \frac{\partial m_f}{\partial \ln a}\frac{\partial}{\partial m_f}\right) P(m_f(a), g(a), a) \\
&= 0.
\end{aligned} \tag{2.44}$$

In the second line we have introduced the lattice β function which determines how the coupling depends on the lattice spacing. From perturbation theory, one obtains two universal coefficients for an expansion of the β function around $g = 0$ with N_c colors and N_f flavors:

$$\begin{aligned}
\beta(g) &= -\frac{\partial g}{\partial \ln a} \\
&= -\beta_0\, g^3 - \beta_1\, g^5 + \mathcal{O}(g^7) \\
\beta_0 &= \frac{1}{(4\pi)^2}\left(\frac{11}{3}N_c - \frac{2}{3}N_f\right) \\
\beta_1 &= \frac{1}{(4\pi)^2}\left(\frac{34}{3}N_c^2 - \frac{10}{3}N_c N_f - \frac{N_c^2 - 1}{N_c}N_f\right).
\end{aligned} \tag{2.45}$$

By separation of observables one can solve the differential equation (2.45) and gain an analytic expression for the coupling g as a function of the lattice spacing a. One important finding is that $g(a)$ vanishes for the continuum limit $a \to 0$, this feature of QCD is called *asymptotic freedom*. While the lattice regularization of QCD enables us to obtain results in the infrared limit of the field theory (where the coupling is of order 1), perturbative calculations are valid in the ultraviolet (where the coupling is much smaller than 1). Thus, the perturbative renormalization schemes are not applicable to lattice calculations and there exist lattice renormalization schemes such as the Schrödinger functional scheme.

When a quark bilinear is renormalized only multiplicatively, one can write its normalized version as

$$\Psi_R = Z_\Psi^{\mathrm{RS}}(\mu, g_0)\Psi \tag{2.46}$$

where the multiplicative renormalization factor $Z_\Psi^{\mathrm{RS}}(\mu, g_0)$ may depend on the renormalization scale μ, the bare coupling g_0 and the particular renormalization scheme (RS)

of choice. The renormalized coupling and the renormalized mass are given by

$$g_r^2 = Z_g(\mu, g_0)\,(1 + b_g a\overline{m}_f)\,g_0^2 \tag{2.47}$$

$$m_r = Z_m(\mu, g_0)\,(1 + b_m a\overline{m}_f)\,\overline{m}_f \tag{2.48}$$

where $\overline{m}_f$ is given by (2.34). The renormalized currents then take the form

$$P_r^a(x) = Z_P(\mu, g_0)\,(1 + b_P a\overline{m}_f)\,P^a \tag{2.49}$$

$$V_{\mu,r}^a(x) = Z_V(g_0)\,(1 + b_V a\overline{m}_f)\,V_\mu^{a,\mathrm{imp}} \tag{2.50}$$

$$A_{\mu,r}^a(x) = Z_A(g_0)\,(1 + b_A a\overline{m}_f)\,A_\mu^{a,\mathrm{imp}} \tag{2.51}$$

2.4 PCAC mass

At the end of section 2.2, we already mentioned the important role of Ward-Takahashi identities for improving and renormalizing lattice quantities. When it comes to quark masses, one may use an operator identity that is strictly valid only as an expectation value in Euclidean space-time. The relation

$$\left\langle \partial_\mu A_{\mu,r}^a(x)\,O \right\rangle = 2m_r \left\langle P_r^a(x)\,O \right\rangle \tag{2.52}$$

holds for a suitable choice of the operator O which is nonzero at x and is chosen such that $\langle P_r^a(x)\,O\rangle$ does not vanish. Then this relation states that the axial current is conserved only in the chiral limit $m_r = 0$. Therefore, this is called the *partially conserved axial current* or PCAC relation. Then one can solve for m_r:

$$m_r = \frac{Z_A(1 + b_A a\overline{m}_f)}{Z_P(1 + b_P a\overline{m}_f)} \cdot \frac{\left\langle \partial_\mu A_\mu^{a,\mathrm{imp}}(x)\,O \right\rangle}{2\,\left\langle P^a(x)\,O \right\rangle} \tag{2.53}$$

where we identify

$$\frac{\left\langle \partial_\mu A_\mu^{a,\mathrm{imp}}(x)\,O \right\rangle}{2\,\left\langle P^a(x)\,O \right\rangle} \equiv m_{\mathrm{PCAC}}. \tag{2.54}$$

In practice, one uses $O = P^a$ and quotes m_r in a particular renormalization scheme, typically the $\overline{\mathrm{MS}}$ scheme. It is important to keep in mind that the value of m_r depends on the renormalization scheme it is quoted in, see subsection 3.4.1.

As a final remark, it is noteworthy to say that improved derivatives also occur in current calculations [49]. They are employed to the end of keeping all occurring terms free of discretization effects up to the same order $\mathcal{O}(a^n)$. The symmetric lattice derivative is already $\mathcal{O}(a)$ improved. It involves values of the function at the site where

it is defined and at two neighboring sites $f(n), f(n \pm \hat{\mu})$. The improved derivative is constructed from values the function takes even two sites away from the definition site, so it involves $f(n), f(n \pm \hat{\mu}), f(n \pm 2\hat{\mu})$. The improvement of derivatives is therefore achieved at the cost of reducing the degree of locality.

2.5 Monte Carlo simulations

For the caclulation of expectation values according to eq. (2.28) where one inserts the $\mathcal{O}(a)$ improved Wilson fermion action (2.37) and the Wilson gauge action (2.15), one utilizes Monte Carlo integration. The improved full QCD action on the lattice is given by

$$S_{\mathrm{QCD}}^{\mathrm{lat}}[\psi, \bar{\psi}, U] = S_G[U] + S_F^{W,\mathrm{imp}}[\psi, \bar{\psi}, U] \tag{2.55}$$

and the partition function reads accordingly:

$$Z = \int \mathcal{D}[\psi, \bar{\psi}]\, \mathcal{D}[U] \exp\left(-S_{\mathrm{QCD}}^{\mathrm{lat}}[\psi, \bar{\psi}, U]\right). \tag{2.56}$$

So far, there is no known way to implement Grassmann-valued fields in a numerical simulation. Therefore one denotes the fermionic part in the general form as $S_F^{W,\mathrm{imp}}[\psi, \bar{\psi}, U] = \sum_{n\in\Lambda} \bar{\psi}(n) D[U] \psi(n)$, integrates out the Gaussian integral over the Grassmannians and obtains the fermion determinant in the calculation of the expectation value

$$\langle O \rangle = \frac{1}{Z} \int \mathcal{D}[U] \det(D[U])\, \tilde{O}[U] \exp\left(-S_G[U]\right). \tag{2.57}$$

Upon this integration, the probability weight changes to

$$\mathrm{d}P(U) = \frac{\det(D[U])\, e^{-S_G[U]}\, \mathcal{D}[U]}{\int \mathcal{D}[U]\, \det(D[U])\, e^{-S_G[U]}}. \tag{2.58}$$

It is easy to see that a pure gauge simulation corresponds to setting the fermion determinant equal to one. The fermion determinant, however, generally depends on the field values U. That means that one has to calculate the determinant for each U which is simply not feasible in numerical simulations because the Dirac operator D is usually very large. One solution is to evaluate the determinant by the introduction of *pseudofermion* fields $\phi^\dagger, \phi$ which respect Bose-Einstein instead of Fermi-Dirac statistics but otherwise carry the same Dirac, color and flavor indices as the original fermion spinor

fields $\bar{\psi}, \psi$. Because we use an even number (two) of mass-degenerate light flavors in our simulations, the fermion determinant can be expressed as

$$\det\left[D[U]\right] = \det\left[M^\dagger[U]M[U]\right] \tag{2.59}$$

where $M[U]$ is given by the Dirac operator for only half the number of flavors in the system. Then the Gaussian integral over the complex bosonic fields $\phi^\dagger, \phi$ yields

$$\int \mathcal{D}[\phi^\dagger, \phi]\, e^{-\phi^\dagger M^\dagger M \phi} \;=\; \frac{1}{\det\left[M^\dagger M\right]}. \tag{2.60}$$

Now one can utilize that the Dirac operator is free of zero modes, i.e. $\det[D] = 1/\det[D^{-1}]$. That means one can evaluate the fermion determinant using the bosonic fields as pseudofermions

$$\begin{aligned}
\int \mathcal{D}[\bar{\psi}, \psi]\, e^{-\bar{\psi} D[U] \psi} &= \det\left[D[U]\right] \\
&= \det\left[M^\dagger[U]M[U]\right] \\
&= \frac{1}{\det\left[(M^\dagger[U]M[U])^{-1}\right]} \\
&= \int \mathcal{D}[\phi^\dagger, \phi]\, e^{-\phi^\dagger (M^\dagger[U]M[U])^{-1} \phi}
\end{aligned} \tag{2.61}$$

where we can now identify the pseudofermionic action

$$S_{PF}[\phi^\dagger, \phi, U] = \sum_{n \in \Lambda} \phi^\dagger(n) \left(M^\dagger[U]M[U]\right)^{-1} \phi(n) \tag{2.62}$$

2.5.1 Importance sampling

The naive Monte Carlo sample summation to evaluate the integral in (2.28) can be given as

$$\langle O \rangle = \lim_{N \to \infty} \frac{1}{N} \sum_{n=1}^{N} O[U_n] \tag{2.63}$$

where U_n denotes a sequence of field configurations sampled according to the probability distribution (2.58). The path integral contains the Boltzmann factor $\exp(-S)$. This means that certain field configurations are given more importance than others depending on the action in the Boltzmann factor. When the integral in (2.28) is determined by a sum over field configurations, it is more important to include configurations with a large weight than those with a small weight [43]. Thus, in importance sampling methods one samples the sum according to the same weight factor. Obviously, the limit of $N \to \infty$

is numerically not feasible, so one has to restrict oneself to an approximation of this sum by a subset of $\tilde{N}$ field configurations, typically this number is of the order of several hundreds for finite temperature simulations with $N_f = 2$ Wilson-type fermions. The infinite Monte Carlo sum of (2.63) is then reduced to the ensemble average

$$\langle O \rangle = \frac{1}{\tilde{N}} \sum_{n=1}^{\tilde{N}} O[U_n] \tag{2.64}$$

Now the task is to generate an ensemble of field configurations U_n according to the probability weight. This is achieved by generating them as a Markov chain, i.e. one proposes a new configuration U_n on the basis of the previous one U_{n-1} (update). Then this candidate configuration is accepted or rejected in a Metropolis accept-reject step. There is one important aspect to consider: the change of the action resulting from updating the configuration needs to be large enough to sample a representative subset of the entire configuration space (ergodicity), simultaneously one wants to keep the acceptance rate high enough such that the configuration will be accepted which means that the change cannot be too large. After enough equilibrating updates, one starts allowing the subsequent configurations to contribute in the Monte Carlo sum. Whether a chain has equilibrated or not, can be determined from autocorrelation times and the behavior of the plaquette observable, for example.

2.5.2 Hybrid Monte Carlo

The hybrid Monte Carlo algorithm is used to find suitable updates for the configurations in simulations that include dynamical fermions. Introducing the computer time τ, we want to consider a microcanonical ensemble of a nonrelativistic system described by the Hamiltonian

$$H[U, P, \phi^\dagger, \phi] = \frac{P^2}{2} + S_G[U] + S_{PF}[\phi^\dagger, \phi, U] \tag{2.65}$$

with the pseudofermionic fields $\phi^\dagger, \phi$ and the conjugate momenta P of the bosonic fields U. The equations of motion are given by

$$\begin{aligned} \dot{P} &= -\frac{\partial H}{\partial U} = -\frac{\partial (S_G + S_{PF})}{\partial U} \\ \dot{U} &= \frac{\partial H}{\partial P} = P \end{aligned} \tag{2.66}$$

where the time derivative is understood to be taken with respect to computer time τ. The equations (2.66) describe the time evolution of a classical system of particles,

hence they are called molecular dynamics (MD) equations [43]. One standard numerical integration technique to solve (2.66) is the leapfrog integrator, see e.g. [50].

This results in an update procedure which is not ergodic. One way to deal with this is a random momentum refreshment at the beginning of each configuration update. In this step, the initial momentum P is chosen from a Gaussian distribution $\propto \exp(-P^2/2)$ and then used for the integration of (2.66). The numerical integration introduces an error because of the finite step size

$$\epsilon = \frac{\tau}{N_{\text{step}}} \tag{2.67}$$

where N_{step} denotes the number of smaller substeps in the leapfrog integrator and τ is also referred to as one molecular dynamics unit (mdu).

The integration error can be compensated when one applies a Metropolis accept-reject step after the end of the integration: The resulting candidate configuration U' is accepted if a pseudorandom rumber r that is uniformly distributed within $[0, 1]$ is smaller than $\exp(-\Delta H)$,

$$r \leq \exp(-\Delta H) \tag{2.68}$$

where $\Delta H = H' - H$ denotes the difference of the action with the updated configurations and momenta ($H' = H[U', P']$) and the initial action ($H = H[U, P]$). This is equivalent to say that the candidate configuration is accepted with the acceptance probability

$$P_{\text{acc}} = \min\left[1, \frac{\exp(-H')}{\exp(-H)}\right]. \tag{2.69}$$

Through the Metropolis accept-reject step one not only corrects for the fact that the MD integration is not exact due to the step size ϵ. One even builds in the effect of quantum fluctuations into the otherwise deterministic MD evolution by the combination of the Metropolis step and the random choice of conjugate momenta as initial momenta for the integration. It is also due to the acceptance probability (2.69) that a candidate configuration that results in a change of the action $\Delta H > 0$ may be accepted from time to time which again improves ergodicity. The combination of the MD evolution with the Metropolis step is then referred to as hybrid Monte Carlo (HMC) algorithm.

In each small substep of the trajectory one has to compute the inverse of the Dirac operator which takes up the most time in the entire algorithm. The inversion is implemented as the solution of an equation of the form

$$D\phi = \eta. \tag{2.70}$$

The Dirac operator D is a large matrix and the solution of (2.70) is constructed utilizing iterative solvers such as the GCR (generalized conjugate residual) or the CG (conjugate gradient) solver, for instance. There are other solvers, too, and they all have in common that they are based on the method of searching for the solution of (2.70) within a Krylov space, see e.g. [50]. In order to improve a solver's convergence properties, one may implement certain preconditioning techniques which may reduce the number of necessary iterations. Two of them - the Schwarz alternating procedure (SAP) and deflation (DFL) - can be effectively combined and the resulting 'DFL-SAP-GCR' solver is the basis for many successful algorithms such as the one used in this work.

Apart from speeding up the solver, the performance of the algorithm can be improved even further when the Dirac operator itself is preconditioned suitably within the HMC algorithm. This is achieved by factorizing the fermion determinant after splitting the Dirac operator into pieces with structures that are easier to handle numerically. One such preconditioning concept is the *mass preconditioning* (MP) by Xxxxxxxxxx where one reduces the condition number of the Dirac operator by performing the inversions first for intermediate masses larger than the target mass and then decreasing the intermediate masses until one reaches the target mass. The Xxxxxxxxxx masses need to be chosen carefully, see also 3.5.1.

2.5.3 Euclidean 2-point functions

In order to obtain information about the spectral properties of low-lying mesons like their mass, one uses the spectral decomposition of the meson correlator. After an insertion of a complete set of eigenstates the correlator or 2-point function is represented by its spectral decomposition:

$$\begin{aligned} \left\langle O(n_\tau)\, O^\dagger(0) \right\rangle &= \sum_k \langle 0|O|k\rangle \left\langle k|O^\dagger|0\right\rangle e^{-n_\tau E_k} \\ &= A\, e^{-n_\tau E_0} + \dots \end{aligned} \tag{2.71}$$

where E_0 is the energy of the ground state. The most important meson propagators that are usually considered in many lattice QCD calculations are given by (2.40).

And then Wick's theorem states that the expectation value of an n-point function is determined by the sum over all possible Wick contractions. A Wick contraction is of the form

$$\overbrace{\psi_f(n)\,\bar{\psi}_{f'}}(m) = D_f^{-1}(n,m)\,\delta_{ff'}, \tag{2.72}$$

that is, it yields the propagator or inverse Dirac operator for flavor f. For meson operators with Dirac structure Γ, we write

$$O_M(n) = \bar{\psi}_{f'}(n)\,\Gamma\,\psi_f(n), \quad \bar{O}_M(n) = \bar{\psi}_f(n)\,\bar{\Gamma}\,\psi_{f'}(n). \tag{2.73}$$

Then the 2-point function for general meson-meson correlators is given by

$$\begin{aligned}
\left\langle O_2(n)\,\bar{O}_1(m)\right\rangle &= \left\langle \bar{\psi}_{f_2'}(n)\,\Gamma_2\,\psi_{f_2}(n)\,\bar{\psi}_{f_1}(m)\,\bar{\Gamma}_1\,\psi_{f_1'}(m)\right\rangle \\
&= \left\langle \psi_{f_2}(n)\,\bar{\Gamma}_1\,\bar{\psi}_{f_1}(m)\,(-1)^3\,\psi_{f_1'}(m)\,\Gamma_2\,\bar{\psi}_{f_2'}(n)\right\rangle \\
&\quad +(-1)^2\,\left\langle \psi_{f_2}(n)\,\Gamma_2\,\bar{\psi}_{f_2'}(n)\right\rangle \left\langle \psi_{f_1'}(n)\,\bar{\Gamma}_1\,\bar{\psi}_{f_1}(m)\right\rangle \\
&= -\operatorname{Tr}\left[D^{-1}_{f_2}(n,m)\delta_{f_2 f_1}\,\bar{\Gamma}_1\,D^{-1}_{f_1'}(m,n)\delta_{f_1' f_2'}\,\Gamma_2\right] \\
&\quad +\operatorname{Tr}\left[D^{-1}_{f_2}(n,n)\delta_{f_2 f_2'}\,\Gamma_2\right]\,\operatorname{Tr}\left[D^{-1}_{f_1'}(m,m)\delta_{f_1' f_1}\,\bar{\Gamma}_1\right].
\end{aligned} \tag{2.74}$$

The first term in the last line of (2.74) is called the connected piece while the second one is the disconnected piece. The cost of a numerical computation of disconnected pieces is usually very high. And they actually cancel out for isovecor operators in the isospin symmetric ($m_u = m_d \equiv m_{\text{light}}$) theory which we consider for the remainder of this thesis.

Since the Wilson Dirac operator satisfies γ_5-hermiticity (2.26), we can rewrite

$$D_f^{-1}(m,n) = \gamma_5\left(D_f^{-1}(n,m)\right)^\dagger\gamma_5 \tag{2.75}$$

und use that in the connected piece of (2.74) such that

$$\left\langle O_2(n)\,\bar{O}_1(m)\right\rangle_C = -\operatorname{Tr}\left[D^{-1}_{f_2}(n,m)\delta_{f_2 f_1}\,\bar{\Gamma}_1\,\gamma_5\left(D^{-1}_{f_1'}(n,m)\right)^\dagger\gamma_5\delta_{f_1' f_2'}\,\Gamma_2\right]. \tag{2.76}$$

With this form, one needs to calculate the propagator from m to n only instead of both the backwards and the forwards propagators. One often sets $m = 0$ for convenience.

So far all the correlators are defined at zero momentum. For correlators at finite momentum one has to project them according to

$$O(\mathbf{p}, n_\tau) = \sum_{\mathbf{n}\in\Lambda_3} O(\mathbf{n}, n_\tau)\,e^{-i\mathbf{n}\cdot\mathbf{p}} \tag{2.77}$$

where $n_i = 0,\ldots,N-1$ and $p_i = \frac{2\pi k_i}{N}, k_i = -\frac{N}{2}+1,\ldots,\frac{N}{2}$ are defined in the Brillouin zone. The operator at the source is placed at the origin $(\mathbf{0},0)$ and the finite momentum

correlator reads

$$\begin{aligned}\left\langle O(\mathbf{p}, n_\tau)\, \bar{O}(\mathbf{0}, 0)\right\rangle &= \sum_{\mathbf{n}\in\Lambda_3} e^{-i\mathbf{n}\cdot\mathbf{p}} \left\langle O(\mathbf{n}, n_\tau)\, \bar{O}(\mathbf{0}, 0)\right\rangle \\ &= A\, e^{-n_\tau E(\mathbf{p})} + \dots \end{aligned} \tag{2.78}$$

The energy is given by $E(\mathbf{p}) = \sqrt{m_M + \mathbf{p}^2}$ where m_M denotes the rest mass of the meson we are examining.

As a concluding remark for this subsection one may state that it is important to keep in mind that the quarks that appear in the fermion determinant are sea quarks while the quarks in the correlators are the valence quarks making up the quark content of the mesons under consideration.

2.5.4 Calculation of the propagator using sources

The Dirac operator is in general a very large matrix and inverting it is very costly. Nonetheless this is the essential task for computing (2.76) where the inverse Dirac operator or quark propagator

$$D^{-1}(n, m)^{ab}_{\alpha\beta} \tag{2.79}$$

connects a source at (m, α, a) to a sink at (n, β, b) where n, m are the respective lattice sites, α, β denote Dirac indices and a, b stand for the color indices. For the computation of connected pieces in 2-point functions, however, one does not need the "all-to-all" propagator but can work with a "point-to-all" propagator. Thus, one introduces point sources of the form

$$\eta(m, m_0)^{aa_0}_{\alpha\alpha_0} = \delta(m - m_0)\delta_{aa_0}\delta_{\alpha\alpha_0} \tag{2.80}$$

and considers only the corresponding column of the full inverse Dirac operator

$$D^{-1}(n, m_0)^{a_0 b}_{\alpha_0\beta} = \sum_{m,\alpha,a} D^{-1}(n, m)^{ab}_{\alpha\beta}\, \delta(m - m_0)\delta_{aa_0}\delta_{\alpha\alpha_0}, \tag{2.81}$$

that is the propagator from the point source at fixed (m_0, α_0, a_0) to all points of the lattice. Then the numerical cost is reduced to 12 inversions (for three color and four Dirac indices) which is much more feasible than inverting the full propagator. The point sources are usually placed randomly on the lattice and depending on the lattice size the number of random sources can be as high as 16 or even 64 in rare cases. This is all done for one single configuration. Then for the next configuration within the ensemble one repeats the aforementioned operations. Thus a statistical average can be formed.

Chapter 3

Tuning of bare parameters for lattice QCD simulations

For convenient readability, the author follows the notation given in the references cited below throughout this chapter. In order to connect the results given in this chapter with the quantities described above, one may keep in mind that we identify these quantities as following:

quantity	this chapter	previous chapters
bare quark mass	m_0	$m_{b,f}$
bare subtracted quark mass	m_q	$\overline{m}_f$
PCAC mass	m_{12}	m_{PCAC}
hopping parameter	κ_c	κ_f

Table 3.1: Table of quantities introduced in previous chapters and used within this chapter with different notation according to the references cited below.

3.1 Fits for the lattice spacing $\frac{a}{L_{\max}}\left(g_0^2\right)$

From Ref. [51], one can learn that any physical quantity P should be independent of the renormalization scale μ. The Callan-Symanzik or renormalization group equation expresses this:

$$\left\{\mu\,\frac{\partial}{\partial\mu}+\beta(\bar{g})\,\frac{\partial}{\partial\bar{g}}+\tau(\bar{g})\,\bar{m}\,\frac{\partial}{\partial\bar{m}}\right\}P=0, \tag{3.1}$$

where the β-function is given by

$$\beta(\bar{g}) = \mu \frac{\partial \bar{g}(\mu)}{\partial \mu}. \tag{3.2}$$

For weak couplings the β-function can asymptotically be expanded as

$$\beta(\bar{g}) = -\bar{g}^3(b_0 + b_1\bar{g}^2 + b_2\bar{g}^4 + \dots). \tag{3.3}$$

Only mass independent renormalization schemes shall be considered in the following, such as the Schrödinger functional and the $\overline{\mathrm{MS}}$ scheme. If the coupling of one such scheme can be expanded as a Taylor series of the other and vice-versa, then the 1- and 2-loop coefficients are universally given by [51]

$$\begin{aligned} b_0 &= \frac{1}{(4\pi)^2}\left(11 - \frac{2}{3}N_f\right) \\ b_1 &= \frac{1}{(4\pi)^4}\left(102 - \frac{38}{3}N_f\right). \end{aligned} \tag{3.4}$$

A special exact solution of the Callan-Symanzik eqn. (3.1) is the renormalization group invariant Λ-parameter [51]

$$\begin{aligned} \Lambda = \mu \left(b_0\, \bar{g}^2(\mu)\right)^{-b_1/\left(2b_0^2\right)} &\cdot \exp\left\{-1/\left(2b_0\, \bar{g}^2(\mu)\right)\right\} \times \\ &\times \exp\left\{-\int_0^{\bar{g}(\mu)} dx \left[\frac{1}{\beta(x)} + \frac{1}{b_0\, x^3} - \frac{b_1}{b_0^2\, x}\right]\right\}. \end{aligned} \tag{3.5}$$

With $\mu = \frac{1}{L}$ the inverse box size of the lattice and $-\log(\Lambda L_{\max}) = 1.09$ at $u_{\max} = \bar{g}^2(L_{\max}) \equiv 5.5$ (see Ref. [51]) we can rewrite eqn. (3.5) as

$$\begin{aligned} \frac{\Lambda}{\mu} &= \Lambda L = \Lambda L_{\max}\frac{L}{L_{\max}} \\ &= \left(b_0\bar{g}^2(\mu)\right)^{-b_1/(2b_0^2)} e^{-1/(2b_0\bar{g}^2(\mu))} \exp\left\{-\int_0^{\bar{g}(\mu)} dx \left[\frac{1}{\beta(x)} + \frac{1}{b_0 x^3} - \frac{b_1}{b_0^2 x}\right]\right\} \end{aligned} \tag{3.6}$$

and make the following fit ansatz for the Λ-parameter, eqn. (3.5):

$$-\log\left(\frac{L}{L_{\max}}\right) = -\log\left\{(\Lambda L_{\max})^{-1}\left(b_0\bar{g}^2(\mu)\right)^{-b_1/(2b_0^2)} e^{-1/(2b_0\bar{g}^2(\mu))} \exp\left(\frac{p(\bar{g}^2, m)}{p(\bar{g}^2, n)}\right)\right\}, \tag{3.7}$$

where we substitute the argument in the last exponential of eqn. (3.5) with a rational function. Here $p(x,k)$ is a polynomial in x of order k with $p(0,\cdot) = 1$.

In Table 5 of Ref. [51] we find in the two columns labeled i the number of recursions and $u_i = \bar{g}^2(L_i)$, $L_i = 2^{-i} L_{\max}$ and $u_0 = u_{\max} = 5.5$. This provides us with data $\{\bar{g}^2(L_i), -\log\left(\frac{L_i}{L_{\max}}\right)\} = \{\bar{g}^2, -\log(2^{-i})\}$ for our fit. With $m = 3$ and $n = 2$ in (3.7) we obtain the form

$$
\begin{aligned}
-\log\left(\frac{L}{L_{\max}}\right) = \; & - \quad \log\left\{9.355 \cdot \bar{g}^{-2\cdot\frac{345}{841}} \cdot e^{-\frac{24\pi^2}{29\bar{g}^2}} \times \right. \\
& \times \quad \left. \exp\left(\frac{1 - 1.89402\,\bar{g}^2 + 1.13921\,\bar{g}^4 - 0.174503\,\bar{g}^6}{1 - 0.0669224\,\bar{g}^2 + 2.54696\,\bar{g}^4}\right)\right\}.
\end{aligned}
\tag{3.8}
$$

This result (3.8) is strictly valid only for $\sim 1.0 \leq \bar{g}^2 \leq \sim 5.5$ (tables 10 and 11 of Ref. [51]). The Schrödinger functional coupling $\bar{g}$ is a renormalized quantity and at fixed L/a depends on the bare coupling g_0. The dependence is given by Taylor expansion of the Schrödinger functional in terms of the bare coupling [51]:

$$
\bar{g}^2 = g_0^2 + \sum_{k=2}^{k=\infty} c_k g_0^{2k}. \tag{3.9}
$$

Table 10 and 11 in [51] provide us with data $\{\beta = 6/g_0^2, \bar{g}^2\}$, where we fix $L/a = 6$ and stick with the data points corresponding to $L/a = 6$. There is one ambiguity for $u = 1.5031$: Table 10 states $\beta = 7.5$ and Table 11 states $\beta = 7.5457$. Although only Table 11 includes the 2-loop corrections, the fit is better when we use $\beta = 7.5$ instead of $\beta = 7.5457$. With a polynomial ansatz (3.9) truncated at $k = 4$ we find the form

$$
\bar{g}^2 = g_0^2 + 3.07442\,g_0^4 - 6.92164\,g_0^6 + 5.52135\,g_0^8 \tag{3.10}
$$

which is valid at least for $5.6215 \leq \beta = \frac{6}{g_0^2} \leq 9.5$. The fit for $\bar{g}^2(g_0^2)$ (3.10) can be inserted into (3.8) and we massage the result to obtain an expression for the quantity we look for, $\frac{a}{L_{\max}}(g_0^2)$:
We know that $\frac{L}{L_{\max}} = f(\bar{g}^2)$ and $\bar{g}^2 = h(g_0^2)$. Now, $\frac{L}{L_{\max}} = \frac{L}{a} \cdot \frac{a}{L_{\max}}$, where we fixed $\frac{L}{a} = 6$. So $\frac{a}{L_{\max}}(g_0^2) = \frac{1}{6} f(h(g_0^2))$.
Finally, we write down the normalized quantity a' as

$$
a'(g_0^2) = \frac{a(g_0^2 = 6/\beta)}{L_{\max}} \cdot \left(\frac{a(g_0^2 = 6/5.5)}{L_{\max}}\right)^{-1} = \frac{a(g_0^2 = 6/\beta)}{a(g_0^2 = 6/5.5)}. \tag{3.11}
$$

3.2 Fits for the hopping parameter κ_c

The hopping parameter can be used to tune the masses of the quarks or, equivalently, the mass of the pions on the lattice. It depends on the bare quark mass, the lattice

spacing and the Wilson parameter r, which is set to $r = 1$ for our purposes [52]:

$$\begin{aligned} \kappa_c &= \frac{1}{2m_c a + 8r} \\ \Leftrightarrow am_c &= \frac{1}{2\kappa_c} - 4. \end{aligned} \tag{3.12}$$

The chiral limit corresponds to $m_c = 0$ and it is achieved for the critical value of the hopping parameter at $1/8$ in the free case. Terms proportional to r in the action and clover terms explicitly break chiral invariance. When $\Sigma^L(p, m_c, g_0)$ denotes the truncated, 1PI fermionic two-point function, one requires that the renormalized mass vanish. Then the explicit breaking of chiral invariance is restored. This leads to [52]

$$m_c = \Sigma^L(0, m_c, g_0). \tag{3.13}$$

Eqn. (3.13) is a recursive equation and can be solved by perturbation theory. The loop expansion reads [52]

$$\Sigma^L(0, m_c, g_0) = g_0^2 \Sigma^{(1)} + g_0^4 \Sigma^{(2)} + \ldots, \tag{3.14}$$

where the coefficients read (cf. eqn. (11) in [52])

$$\Sigma^{(1)} = \frac{N^2 - 1}{N}(-0.162857 + 0.043483\, c_{SW} + 0.018096\, c_{SW}^2) \tag{3.15}$$

and (cf. eqn. (15) in [52])

$$\begin{aligned} \Sigma^{(2)}(N = 3, N_f = 2) = &- 0.11924 + 0.0174\, c_{SW} + 0.008368\, c_{SW}^2 \\ &- 0.004857\, c_{SW}^3 - 0.0011562\, c_{SW}^4 \end{aligned} \tag{3.16}$$

with the Sheikholeslami-Wohlert or clover term c_{SW}.
In [53], the clover term is given by

$$c_{SW} = c_{SW}^{(0)} + c_{SW}^{(1)} g_0^2 + c_{SW}^{(2)} g_0^4 + \ldots, \tag{3.17}$$

where $c_{SW}^{(0)} = 1$ and $c_{SW}^{(1)} = 0.267$ for $N = 3$ [53]. XXXX and XXX state the numbers obtained by Xxxxxx as $c_{SW}^{(1)} = 0.2659$ for $N = 3$, but we will stay with the parameters found by XXXX and XXX.

For the 2-loop critical mass, i.e. keeping terms only up to order g_0^4 (only including

$c_{SW}^{(0)}$ and $c_{SW}^{(1)}$) we find

$$
\begin{aligned}
am_c^{(2)} &= \frac{1}{2\kappa_c^{(2)}} - 4 \\
&= a\left(g_0^2\,\Sigma^{(1)} + g_0^4\,\Sigma^{(2)}\right) \\
&= a\Big[g_0^2\cdot\frac{8}{3}(-0.15493339023106021 - 0.00792366847979 + \\
&\quad 0.04348303388205\,c_{SW} + 0.01809576878142\,c_{SW}^2) \\
&\quad + g_0^4(-0.11924 + 0.0174\,c_{SW} + 0.008368\,c_{SW}^2 - 0.004857\,c_{SW}^3 - 0.0011562\,c_{SW}^4)\Big] \\
&= a\Big[g_0^2\cdot\frac{8}{3}(-0.15493339023106021 - 0.00792366847979 + \\
&\quad 0.04348303388205(1 + 0.267\,g_0^2) + 0.01809576878142(1 + 2\cdot 0.267\,g_0^2)) \\
&\quad + g_0^4(-0.11924 + 0.0174\cdot 1 + 0.008368\cdot 1 - 0.004857\cdot 1 - 0.0011562\cdot 1)\Big] \\
&= -0.270075\,g_0^2 - 0.0661046\,g_0^4
\end{aligned}
\tag{3.18}
$$

with $a = 1$.

One source for data points $\{g_0^2, am_c = \frac{1}{2\kappa_c} - 4\}$ is Ref. [51], where in Tables 10 and 11 we use the κ_c-values with the corresponding β-values for $L/a = 8$ (not 6), because the tuning was apparently best achieved for $L/a = 8$. Now we can fit a polynomial ansatz to the data points $\{g_0^2, am_c = \frac{1}{2\kappa_c} - 4\}$ and make sure that the slope and curvature (the first- and second-order coefficients of the polynomial ansatz) match the 2-loop coefficients found in eqn. (3.18). In [54] we find that Table 14 yields three more values for the critical value of the hopping parameter κ_c at $\beta = 5.2, 5.3, 5.5$, and so the fit ansatz

$$
am_c(g_0^2) = -0.270075\,g_0^2 - 0.0661046\,g_0^4 + \sum_{k=3}^{\infty} c_k\,g_0^{2k} \tag{3.19}
$$

yields

$$
\begin{aligned}
am_c(g_0^2) &= -0.270075\,g_0^2 - 0.0661046\,g_0^4 + 0.64402\,g_0^6 - 1.56168\,g_0^8 \\
&\quad -1.46995\,g_0^{10} + 7.43682\,g_0^{12} - 7.54832\,g_0^{14} + 2.50277\,g_0^{16}
\end{aligned}
\tag{3.20}
$$

truncated at $k = 8$. It is valid for β values in the range of $5.2 \le \beta = \frac{6}{g_0^2} \le 9.7341$. And it is very easy now to write down the form of $\kappa_c(\beta)$:

$$
\kappa_c(g_0^2 = 6/\beta) = \frac{1}{2am_c(g_0^2 = 6/\beta) + 8}\,. \tag{3.21}
$$

In Ref. [55] we find an estimate for the hopping parameter κ_c:

$$\kappa_c(g_0^2) = \frac{1}{8} + 0.008439857\, g_0^2 + 0.0085\, g_0^4 - 0.0272\, g_0^6 + 0.042\, g_0^8 - 0.0204\, g_0^{10} \tag{3.22}$$

which is compared to our result in fig. 3.5. The red curve does not describe the data as well as our Padé fit (insert the polynomial (3.20) into (3.21)) does.

3.3 Fits for $Zr_m(g_0^2)$

From [54] we quote equation (E.1)

$$m_{12}(1 + \tilde{b}_r a m_{12}) = Z_m \frac{Z_P}{Z_A} r_m m_q \equiv Z r_m m_q. \tag{3.23}$$

In Table 14 of [54] we find values for Zr_m at $\beta = 5.2, 5.3, 5.5$, so that we can use the one-loop result $Zr_m = 1 + 0.090514 g_0^2$ [54] and references therein to make the non-perturbative fit ansatz for $Zr_m(g_0^2)$

$$Zr_m(g_0^2) = (1 + 0.090514 g_0^2) \cdot \frac{1 + \sum_{m=2} a_m g_0^{2m}}{1 + \sum_{n=2} b_n g_0^{2n}}, \tag{3.24}$$

inspired by

$$Z = (1 + 0.090154\, g_0^2) \frac{1 - 0.3922\, g_0^4 - 0.2145\, g_0^6}{1 - 0.6186\, g_0^4}, \tag{3.25}$$

which comes from [54] and references therein. The ansatz (3.24) results in

$$Zr_m(g_0^2) = (1 + 0.090514\, g_0^2) \cdot \frac{1 - 0.636193\, g_0^4 - 0.057574\, g_0^6}{1 - 0.713871\, g_0^4} \tag{3.26}$$

which is strictly valid only for $5.2 \leq \beta = \frac{6}{g_0^2} \leq 5.7$. The findings of Ref. [56], however, suggest that such a Padé fit is still reliable for $\beta \leq 6.6$. There is a pole in this expression but it lies outside the area of interest (at values of $\beta < 5.2$).

3.4 Parameters obtained from the literature

For future lattice calculations we will need ensembles of gauge field configurations over which we can form the ensemble average. These configurations are obtained from production runs. Production runs are run at a certain temperature to which belongs a certain value of β, of κ and κ_c, as well as of the clover term c_{SW}.

In Mainz, there were configurations produced at $T = 254\,\mathrm{MeV}$ where $\beta = 6/g_0^2 = 5.5$. So from eqn. (3.11) we can deduce the lattice spacing in relation to the lattice spacing at $\beta = 6/g_0^2 = 5.5$. Now, the plan is to produce configurations at temperatures

$$T_i = T_{\mathrm{start}} \cdot 2^i, \qquad i \in \{1, 2, 3, 4, 5\}\,, \tag{3.27}$$

with $T_{\mathrm{start}} = 254\,\mathrm{MeV}$, i.e. for temperatures up to $8128\,\mathrm{MeV}$. The lattice spacings will be divided by two since

$$\begin{aligned} \beta_i &= \frac{1}{T_i} \cdot 197\,\mathrm{MeVfm} \\ a_i &= \frac{\beta_i}{N_t} = \frac{197\,\mathrm{MeVfm}}{16 \cdot T_i}. \end{aligned} \tag{3.28}$$

The values for a_i can be plugged into

$$\log(a'(g_0^2)) = \log(2^{-i}) \tag{3.29}$$

and the solutions for g_0^2 are used for finding all the parameters at the respective temperatures T_i.

3.4.1 Mass

Since we want to stay on a line of constant physics at all temperatures, we set the quark mass in the $\overline{\mathrm{MS}}$ scheme to

$$\overline{m}^{\overline{\mathrm{MS}}}(\mu = 2\mathrm{GeV}) = 12.8\,\mathrm{MeV} = \textit{const.} \tag{3.30}$$

throughout all the configurations at all temperatures, where $\mu = 1/L$ is the scale. All subsequent explanations follow the discussion in [54] and references therein.

Now from the $\overline{\mathrm{MS}}$ scheme one can convert to the RGI mass

$$\overline{m}^{\overline{\mathrm{MS}}} = 0.740(12) \cdot M \tag{3.31}$$

and from the RGI mass to the Schrödinger functional scheme via

$$M = 1.308(16)\,\overline{m}. \tag{3.32}$$

The renormalization factor that converts from the Schrödinger functional mass to the PCAC mass, is given by

$$\overline{m}(\mu) = \frac{Z_A}{Z_P^{SF}(\mu)}\, m_{12}, \tag{3.33}$$

where Z_A is given by

$$Z_A(g_0^2) = 1 - 0.116458\, g_0^2 + 0.0116\, g_0^4 - 0.0721\, g_0^6 \tag{3.34}$$

and

$$Z_P = 0.5184(53), \quad \text{for} \quad 5.2 \leq \beta = \frac{6}{g_0^2} \leq 6.0. \tag{3.35}$$

The bare subtracted quark mass m_q is related to the PCAC mass via

$$\begin{aligned} m_q &= \frac{1}{Zr_m(g_0^2)} m_{12}(1 + \tilde{b}_r a m_{12}) \\ &= \frac{1}{Zr_m(g_0^2)} m_{12} \left(1 + \left(\frac{1}{2} + 0.05 g_0^2\right) a m_{12}\right), \end{aligned} \tag{3.36}$$

where the fit for $Zr_m(g_0^2)$ is given in section 3.3.

So now we know how to convert our constant and fixed mass in the $\overline{\mathrm{MS}}$ scheme of $\overline{m}^{\overline{\mathrm{MS}}} = 12.8\,\mathrm{MeV}$ to the bare subtracted quark mass m_q at the different values of $\beta = 6/g_0^2$ corresponding to different lattice spacings/different temperatures. The lattice parameter, however, that tunes the bare subtracted quark mass, is κ. For each and every value of β we know the corresponding hopping parameter κ_c, cf. section 3.2. So with am_q and κ_c at hand we find the parameter values for κ by (around eqn. (E.1) in [54])

$$\begin{aligned} am_q &= am_0 - am_c \\ &= \frac{1}{2\kappa} - \frac{1}{2\kappa_c}. \end{aligned} \tag{3.37}$$

3.4.2 Clover or Sheikholeslami-Wohlert term

Also the clover term has a g_0^2-dependence which was fitted by Xxxxxx and Xxxxxx [55] to

$$c_{SW} = \frac{1 - 0.454\, g_0^2 - 0.175\, g_0^4 + 0.012\, g_0^6 + 0.045\, g_0^8}{1 - 0.720\, g_0^2} \tag{3.38}$$

with a pole outside our range of interest (pole at $\beta < 5.2$).

3.5 Summary of all lattice parameters

In this section, all the parameters for the different temperatures are presented. They are obtained by fits to the relevant data sets found in the literature or they were calculated

$T/\,\mathrm{MeV}$	g_0^2	β	κ_c	κ	c_{SW}
254	1.09091	5.5	0.13677530	0.13671046	1.7515
508	0.993712	6.03796	0.13627057	0.13623795	1.51726
1016	0.921294	6.51258	0.13542605	0.13541002	1.41088
2032	0.86062	6.97172	0.13463322	0.13462535	1.34611
4064	0.806692	7.43779	0.13390756	0.13390369	1.30072
8128	0.757069	7.92531	0.13323188	0.13322997	1.26614

Table 3.2: Lattice parameters for $V/a^4 = N_\tau \cdot N_\sigma^3 = 16 \cdot 64^3$ at different temperatures. The parameters at $T = 254\,\mathrm{MeV}$ are used as input for the extrapolations and fits and were obtained during ensemble productions by Xxxxxxx X. Xxxxxx. Out of the other ensembles at different temperatures only the one at $T = 508\,\mathrm{MeV}$ was produced to date.

$T/\,\mathrm{MeV}$	g_0^2	β	κ_c	κ	c_{SW}
254	1.02966	5.82716	0.13658765	0.13654396	1.58782

Table 3.3: Lattice parameters for $V/a^4 = N_\tau \cdot N_\sigma^3 = 24 \cdot 96^3$ at $T = 254\,\mathrm{MeV}$. The parameters are obtained in the same way as the ones in table 3.2, but at a lattice spacing $2/3$ the one of the $V/a^4 = N_\tau \cdot N_\sigma^3 = 16 \cdot 64^3$ ensemble at $T = 254\,\mathrm{MeV}$. Then the temperature is kept the same but the lattice is finer.

using the formulae already presented in the literature as can be seen in the previous sections.

For the lattice of $V/a^4 = N_\tau \cdot N_\sigma^3 = 16 \cdot 64^3$ we find the parameters shown in table 3.2 and for the lattice of $V/a^4 = N_\tau \cdot N_\sigma^3 = 24 \cdot 96^3$ we find them displayed in table 3.3.

3.5.1 Tuning algorithmic parameters

For the MP-HMC code, one needs three values of κ one of which being the target κ_{target} and the other two being smaller values κ_i corresponding to higher masses. With the highest mass one can solve the Hybrid Monte Carlo equation more easily and then solve it again with the slightly lower mass until one reaches the target mass with the target κ_{target}. In order to calculate the two mass-preconditioning κ_i values we avail

ourselves of the values previously used within the group and use the same mass ratios:

$$\begin{aligned} \frac{am_q(\kappa_{i,D})}{am_q(\kappa_{\text{target},D})} &\stackrel{!}{=} \frac{am_q(\kappa_{i,A})}{am_q(\kappa_{\text{target},A})} \\ \frac{\frac{1}{\kappa_{i,D}} - \frac{1}{\kappa_{c,D}}}{\frac{1}{\kappa_{\text{target},D}} - \frac{1}{\kappa_{c,D}}} &= \frac{\frac{1}{\kappa_{i,A}} - \frac{1}{\kappa_{c,A}}}{\frac{1}{\kappa_{\text{target},A}} - \frac{1}{\kappa_{c,A}}} \end{aligned} \tag{3.39}$$

where D denotes the previously used values of the group and A indicates the values of κ of this work. Hence, we find

$$\kappa_{i,A} = \left[\frac{1}{\kappa_{c,A}} + \left(\frac{1}{\kappa_{\text{target},A}} - \frac{1}{\kappa_{c,A}}\right)\left(\frac{\frac{1}{\kappa_{i,D}} - \frac{1}{\kappa_{c,D}}}{\frac{1}{\kappa_{\text{target},D}} - \frac{1}{\kappa_{c,D}}}\right)\right]^{-1} \tag{3.40}$$

with $i = 1, 2$.

Outlook

Since most of the temperatures we are interested in correspond to values of β much higher than 6, it is important to determine Z_P as a function of g_0^2 in that parameter region, but this is subject to future work.

3.6 Plots

In the following, some of the fitted functions with data from the literature are shown. The fits were performed using `Mathematica 10` and the χ^2 values are compatible with zero.

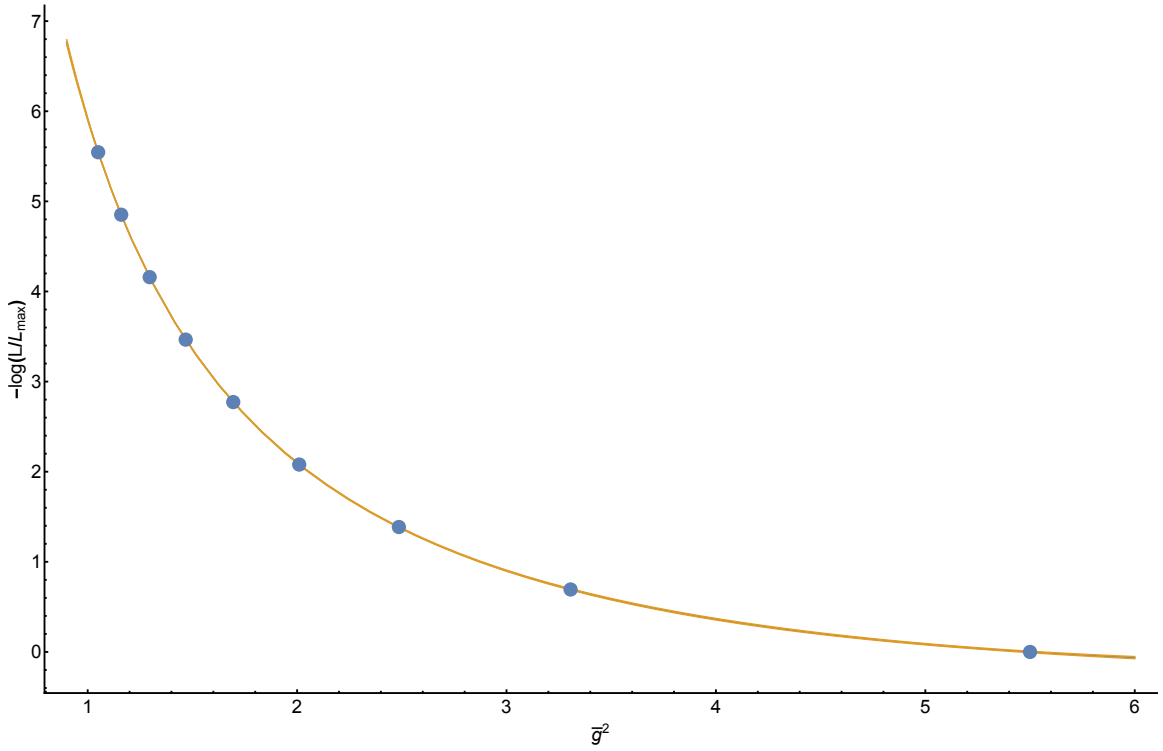

Figure 3.1: Plot of data and fitted curve for $-\log(L/L_{\max})$, cf. eqn. (3.8).

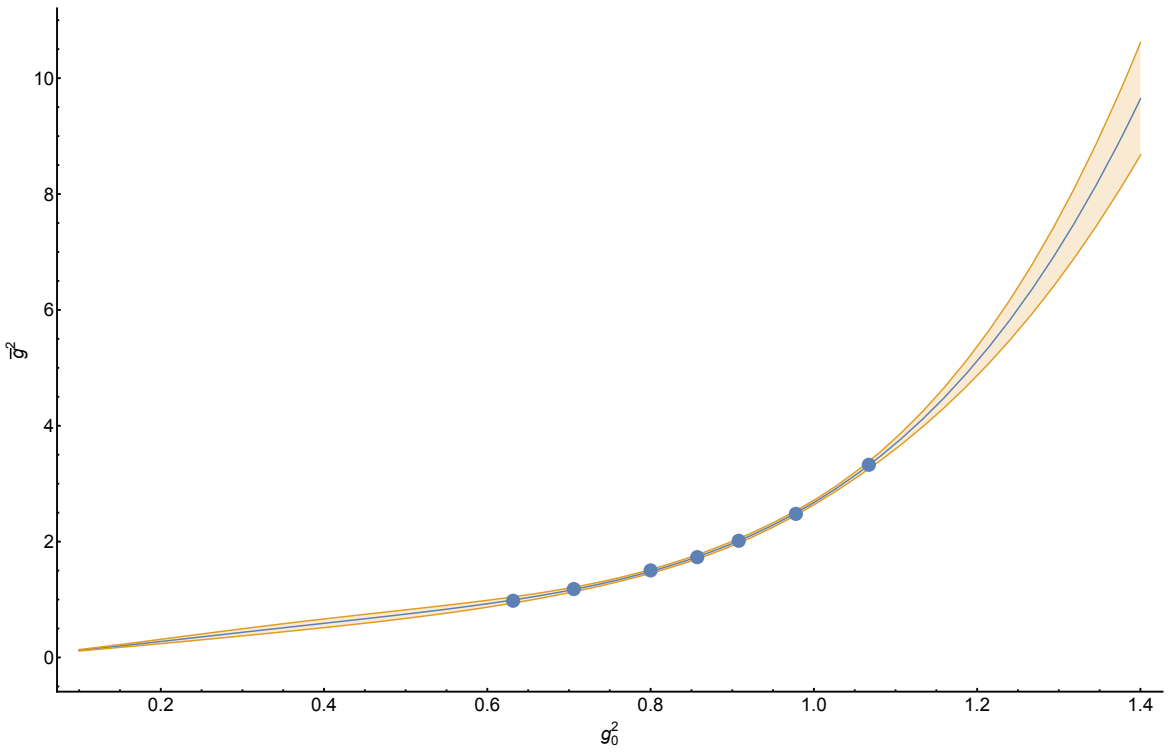

Figure 3.2: Plot of data and fitted curve for $\bar{g}^2(g_0^2)$, cf. eqn. (3.10).

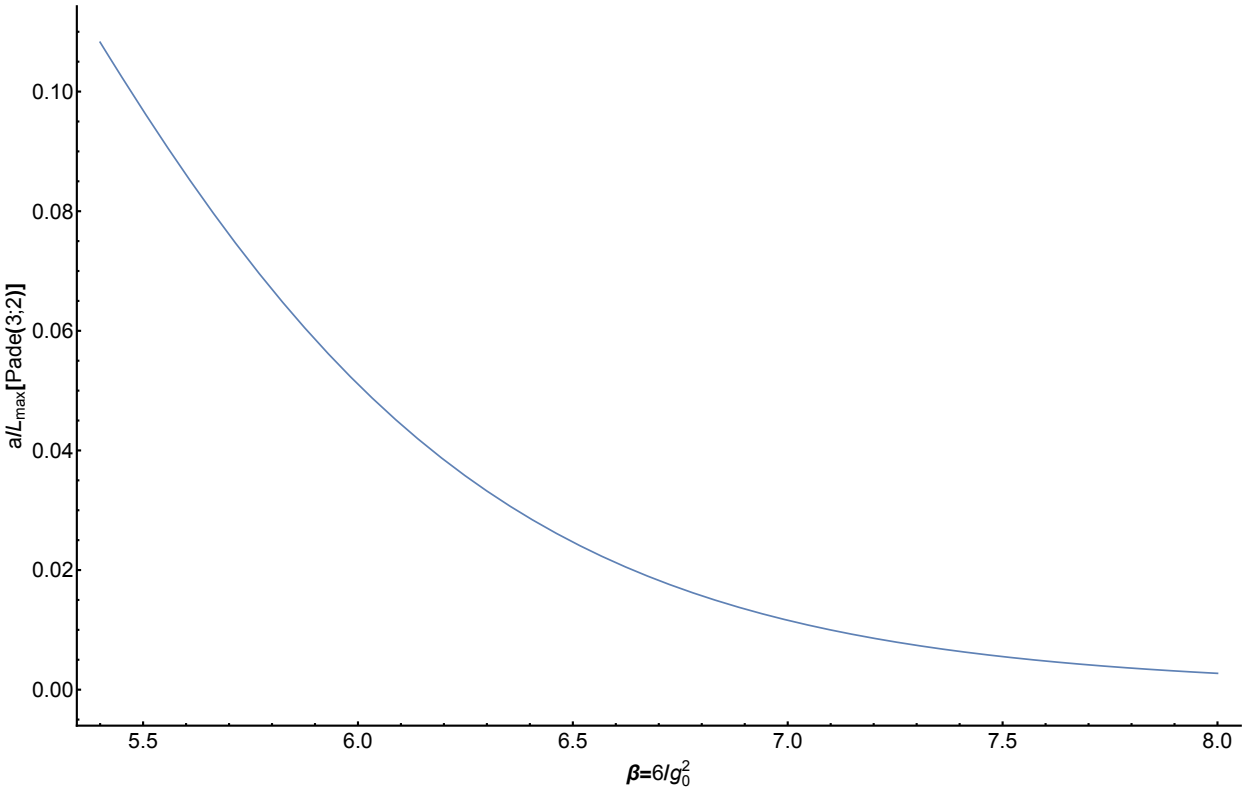

Figure 3.3: Plot of fitted curve for $\frac{a}{L_{\max}}(\beta)$.

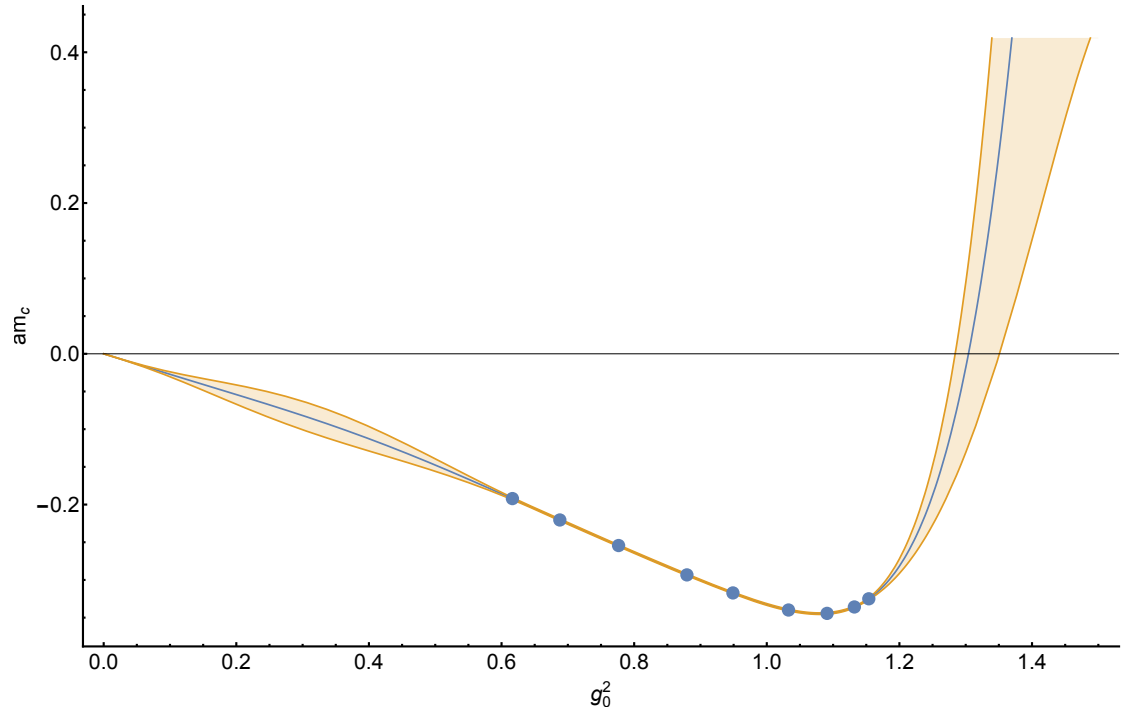

Figure 3.4: Plot of data and fitted curve for $am_c(g_0^2)$ with data points from [51] and [54].

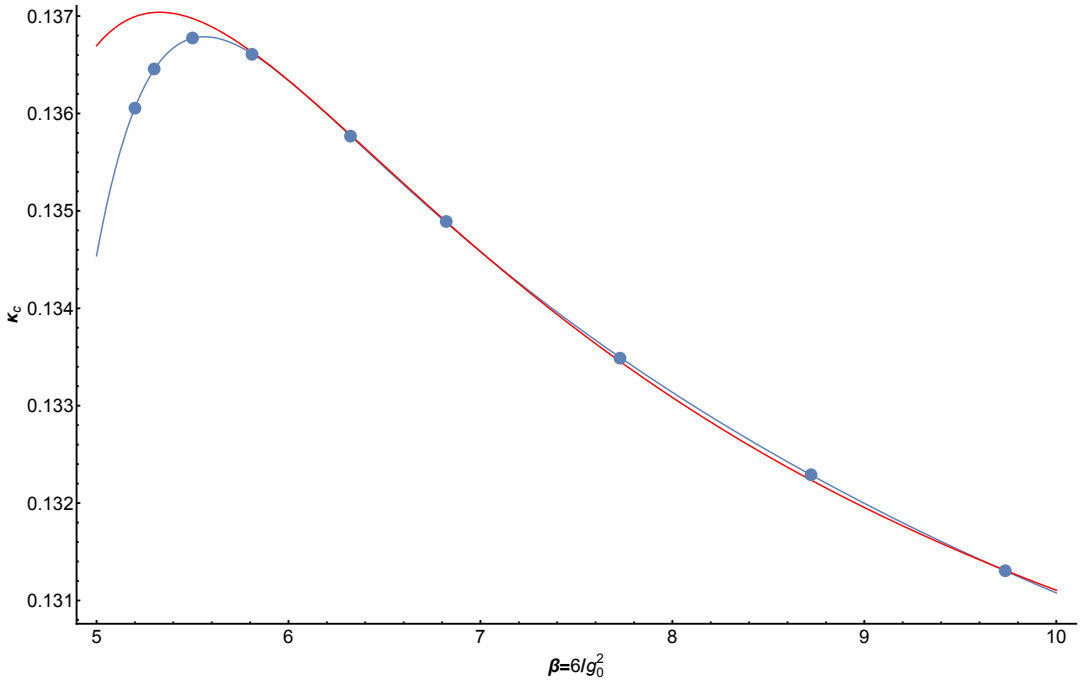

Figure 3.5: Comparison of fitted curve for $\kappa_c(\beta)$, cf. eqn. (3.21) (blue), and eqn. (3.22) (red), with data points from [51] and [54].

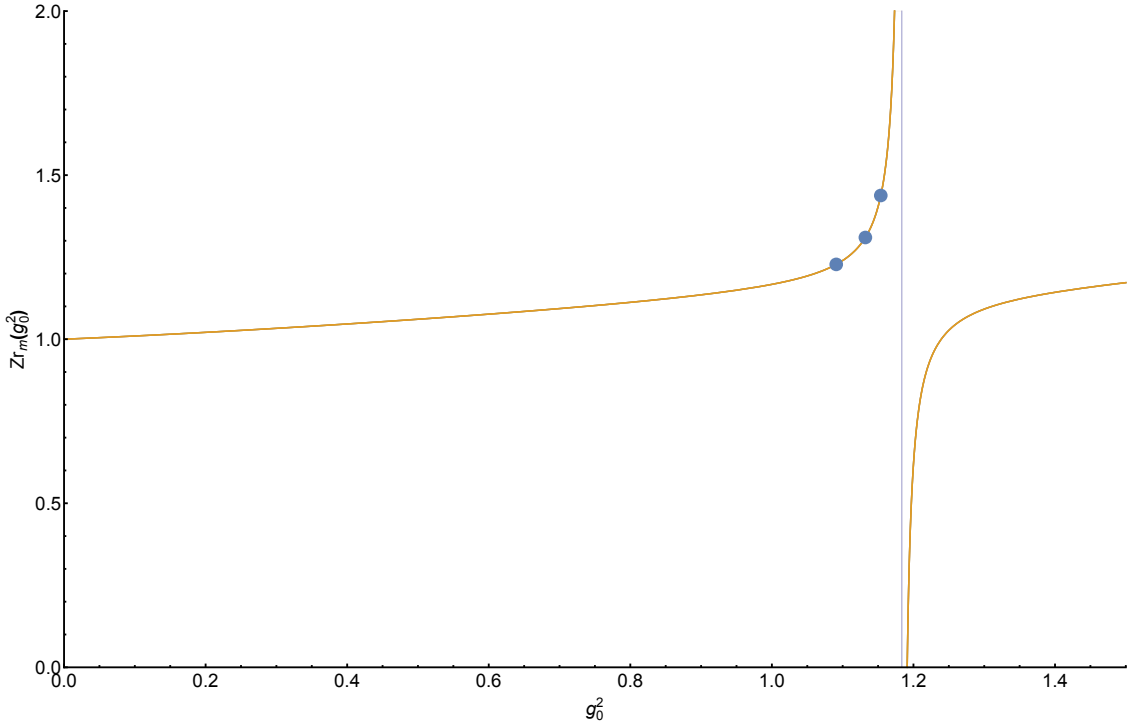

Figure 3.6: Plot of data and fitted curve for $Zr_m(g_0^2)$, cf. eqn. (3.26), with data points from [54].

Chapter 4

Gauge ensembles, correlators and continuum limit

After having tuned both the lattice and the algorithmic parameters as presented in the previous chapter we can summarize the generation of the lattice gauge ensembles, the measurement of the relevant 2-point functions as well as the construction of their continuum limit.

4.1 Gauge ensembles at $N_f = 2$ flavors

Over the course of this work two lattice gauge ensembles with two $\mathcal{O}(a)$ improved Wilson quarks with degenerate light quark masses at temperatures of $T = 508\,\mathrm{MeV}$ and $T = 254\,\mathrm{MeV}$ were generated using the MP-HMC algorithm [57, 58] in the implementation of Xxxxxxxxxx and Xxxxxxxx [59] which is based on XXXX's DD-HMC package found at *http://xxxxxxx.web.cern.ch/xxxxxxx/DD-HMC/index.html*.

The Y7 ensemble

The lattice group at Uni Mainz has generated a finite temperature ensemble at $T = 254\,\mathrm{MeV}$ with a lattice volume of $V/a^4 = N_\tau \times N_\sigma^3 = 16 \times 64^3$. This ensemble labeled O7 was described in Refs. [60, 61] and had a lattice spacing of $a \approx 0.048\,\mathrm{fm}$. It is based on a zero temperature ensemble of the same label described, e.g., in Ref. [54]. By using the same number of lattice sites in the temporal direction, but only half the lattice spacing and tuning the lattice parameters accordingly as demonstrated in the previous chapter (see table 3.2), one can produce a lattice ensemble at double the

temperature (i.e. $508\,\mathrm{MeV}$) according to

$$T = \frac{1}{N_\tau a}. \tag{4.1}$$

Since the $N_\tau = 16$ ensemble at $T = 254\,\mathrm{MeV}$ was already in a thermalized state, we were able to start a new production run from one of these thermalized configurations rather than from a hot start (all gauge links of the initial configuration set to random values) or a cold start (all gauge links of the initial configuration set to one). That meant that the thermalization of the new gauge ensemble with $N_\tau = 16$, but at $T = 508\,\mathrm{MeV}$ was achieved rather quickly. Studying the autocorrelation of the average plaquette of this ensemble showed that the autocorrelation time was given by about $20\,\mathrm{mdu}$ where mdu stands for 'molecular dynamics unit'. With the solver time set to $\tau = 2$ that means one may measure the correlation functions only on every tenth trajectory. Therefore only every tenth trajectory was saved as configuration in the gauge ensemble. The label of this ensemble is Y7. The history of the average plaquette of Y7 is shown in fig. 4.1. It progresses stably and can be considered thermalized from the beginning. The vertical dashed lines indicate where continuation runs were started[1]. This is particularly interesting for both the acceptance rate, fig. 4.2, and ΔH the difference between the action with updated configurations and momenta and the initial action, see eqn. (2.68) and fig. 4.3. For the case of the acceptance rate, one can see that the rate can drop (or sometimes rise) considerably after a continuation run starts because the acceptance rate counter is set to zero at the beginning of each continuation run. The acceptance rate $R_{\mathrm{acc}}(\mathrm{mdu})$ of a (new/continuation) run is defined as the number of accepted trajectories locally averaged over all trajectories generated within the respective run up to a given molecular dynamics unit (mdu).

$$R_{\mathrm{acc}}(\mathrm{mdu}) = \frac{N_{\mathrm{acc}}}{N}(\mathrm{mdu}) \tag{4.2}$$

where N_{acc} is the number of accepted trajectories and N is the number of all trajectories within one (new/continuation) run evaluated at a given mdu. Thus, a single configuration that is not accepted at the beginning of a (new/continuation) run, has much more weight in the rate. When the generation lasts for a longer amount of molecular dynamics units, the acceptance rate stabilizes around 0.95. The ΔH seems to vary within a narrower window for $\mathrm{mdu}/2 < 1100$ than for larger mdu (third vertical dashed

[1] New continuation runs start after adjusting algorithmic parameters such as deflation space, number of Krylov vectors, etc. in order to enhance the performance with respect to the physical time one trajectory takes to be generated.

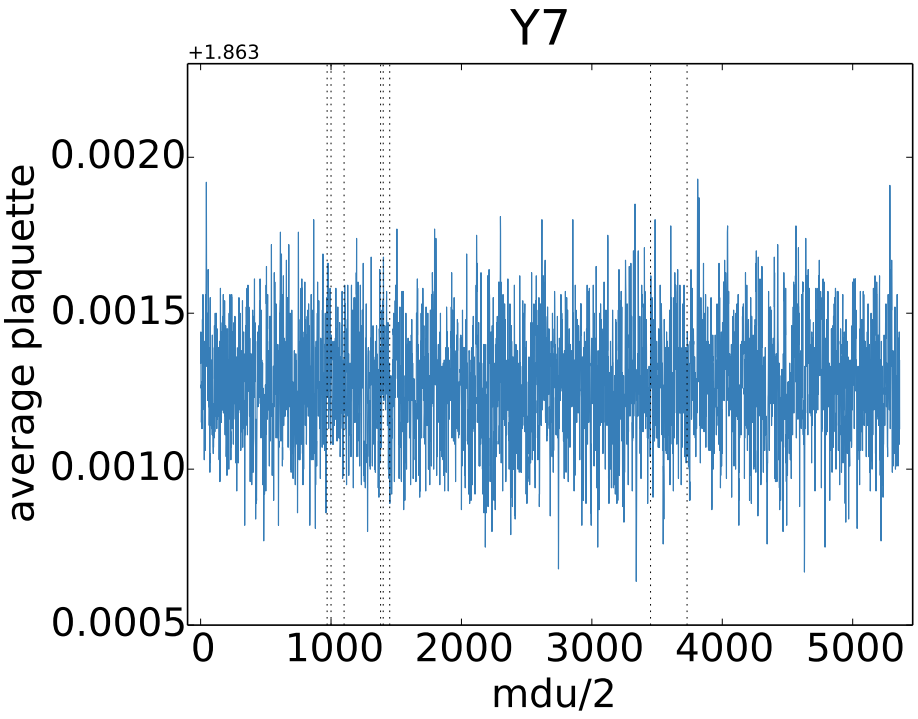

Figure 4.1: The average plaquette of the Y7 ensemble.

line from the left), fig. 4.3. The continuation run starting from $\mathrm{mdu}/2 = 1100$ has a reduced $N3 = 18$ as compared to $N3 = 30$ or $N3 = 27$ before this continuation run[2], which might have resulted in the broader window for the ΔH variance.

The X7 ensemble

In Table 3.3 we show the parameters as they were tuned for the generation of another ensemble at $T = 254\,\mathrm{MeV}$ which we label X7. This ensemble has a lattice volume of $V/a^4 = N_\tau \times N_\sigma^3 = 24 \times 96^3$ such that it preserves the aspect ratio of $L/\beta = 4$ where $\beta = 1/T$ that was also given for the O7 ensemble. In order to keep the temperature the same, one has to decrease the lattice spacing when increasing the number of lattice sites. So for the X7 ensemble with $N_\tau = 24$ the lattice spacing has to be $2/3$ the one of O7. With a third and coarse ensemble at $T = 254\,\mathrm{MeV}$ and $V/a^4 = N_\tau \times N_\sigma^3 = 12 \times 48^3$ labeled F7 at hand (see also [60, 61]), one can then measure observables on all three lattices and construct a continuum limit for these observables. The bare parameters of the finite-temperature ensembles F7 and O7

[2] $N3$ is related to N_{step} the number of substeps in the integrator and thus to the finite step size, eqn. (2.67).

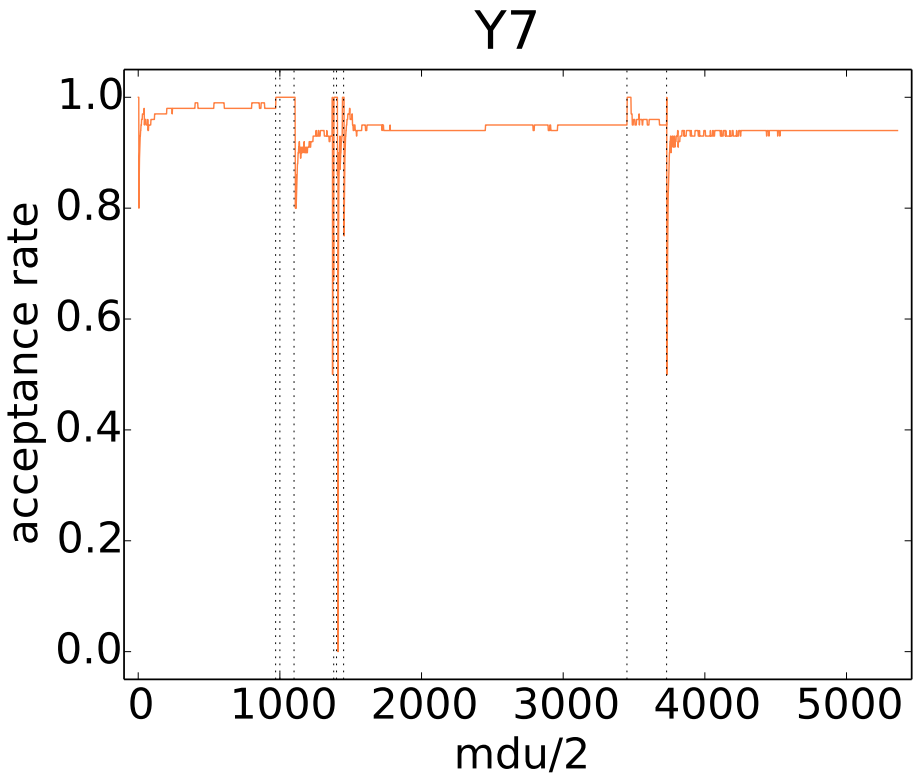

Figure 4.2: The acceptance rate of the Y7 ensemble, see eqn. (4.2).

are identical to the bare parameters of the corresponding zero-temperature ensembles with the same labels. The generation of X7 was more involved. At first, Xxx Xxxxxx generated and thermalized a pure glue (quenched) ensemble with the corresponding parameters calculated by Xxxxxx Xxxxx. And only then we could start a production run from a thermalized, albeit purely quenched configuration. Since the quenched theory corresponds to all quark masses being sent to infinity, starting a production run from a quenched configuration but now with a κ value corresponding to the target $\overline{\mathrm{MS}}$ mass of about $12.8\,\mathrm{MeV}$ means that the solvers for inverting the Dirac operator will fail to converge. Therefore we ran intermediate production runs with bare subtracted quark masses that were deliberately set to substantially larger values than the target bare subtracted quark mass corresponding to an $\overline{m}^{\overline{\mathrm{MS}}}(\mu = 2\,\mathrm{GeV}) = 12.8\mathrm{MeV}$. When the average plaquette of such an intermediate run had nearly or already thermalized, we initated a new intermediate production run with a bare subtracted quark mass lower than the previous one but closer to the target bare subtracted quark mass. This procedure was repeated until the target bare subtracted quark mass could be simulated without convergence issues of the solver. The actual $\overline{\mathrm{MS}}$ mass was found to be $\overline{m}^{\overline{\mathrm{MS}}} \approx 16\mathrm{MeV}$.

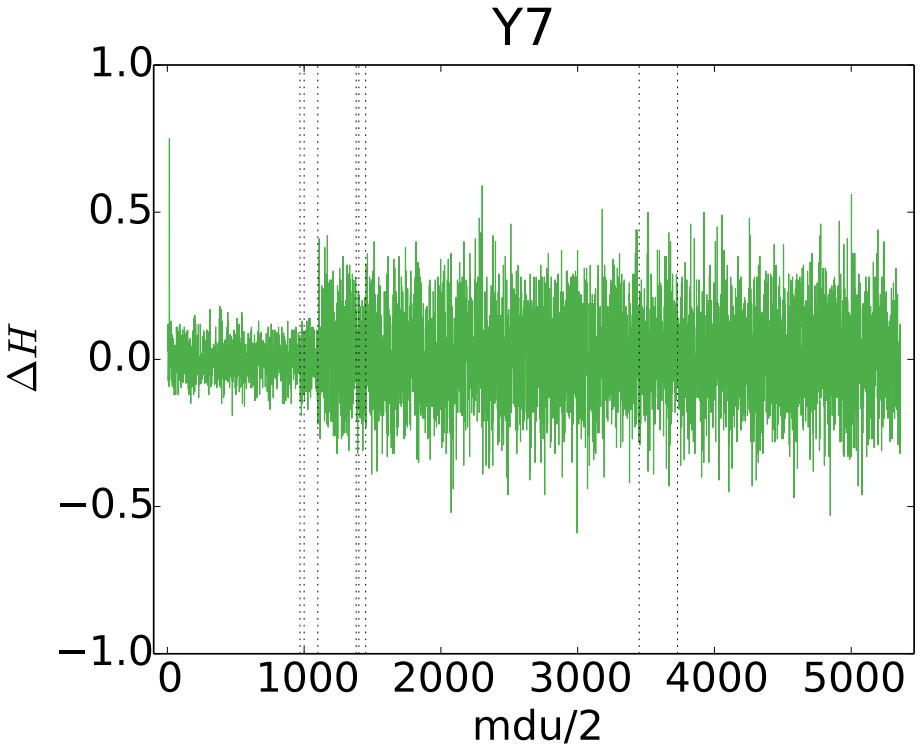

Figure 4.3: The ΔH (see around eqn. (2.68)) of the Y7 ensemble.

That is slightly higher than what we aimed for but the ratio $\overline{m}^{\overline{\mathrm{MS}}}/T \approx 6\%$ is still small enough so that one can safely neglect the effect of unphysically high quark masses.

Xxxxx XX pointed out that the autocorrelation time for gluonic or topological observables becomes very large for lattices with very small lattice spacing such as the one of X7. This is due to the known critical slowing down of the HMC algorithm [62, 63]. Xxxxx XX observed an integrated autocorrelation time of $540\,\mathrm{mdu}$ for the observable of the topological charge Q,

$$Q = \int \mathrm{d}^4x\, q(x), \qquad q(x) = \frac{1}{64\pi^2}\, \varepsilon_{\mu\nu\rho\sigma}\, F^a_{\mu\nu}(x) F^a_{\rho\sigma}(x). \tag{4.3}$$

This means that the finest ensemble is seriously affected by topological charge freezing. Fortunately, our observables of interest presented in the next section 4.2 have little coupling to the topological or gluonic observables. Hence, we may neglect the effect of topological charge freezing and extremely long autocorrelation times for these observables.

In an analysis [64] conducted after the analyses in this work, we accounted for the effects of autocorrelation and thermalization by excluding the first 200 configurations of the chain. We were able to do this because there were around 700 configurations

produced on X7 such that we could drop the first two hundred from the chain whereas at the time the analysis of this work was conducted, there were only about one hundred configurations available. Dropping the first 200 configurations resulted in an improvement of the quality of the continuum limit.

In fig. 4.4, the average plaquette for the X7 ensemble is shown during thermalization. The thermalization run starts from a thermalized, quenched configuration and the value of the average plaquette drops considerably after a few trajectories (or mdu). The vertical dashed lines indicate where a new (slightly higher) κ value was chosen. This corresponds to choosing slightly lower masses because we approached the target bare subtracted quark mass after gradually lowering the bare subtracted quark mass to accommodate for the effect that the quark masses are sent to infinity in the quenched theory. One can see that at each vertical dashed line, the average plaquette rises and plateaus. This is a sign that the average plaquette might have thermalized, and a new run was started with a higher κ value. The vertical lines correspond to the following intermediate κ values: start $\kappa = 0.120001$, 1 $\kappa = 0.120001$, 2 $\kappa = 0.125000$, 3 $\kappa = 0.129000$, 4 $\kappa = 0.130332$, 5 $\kappa = 0.131133$, 6 $\kappa = 0.132353$, 7 $\kappa = 0.133387$, 8 $\kappa = 0.134437$, 9 $\kappa = 0.135719$, 10 $\kappa = 0.136152$, 11 $\kappa = 0.136239$, 12 $\kappa = 0.136326$, 13 $\kappa = 0.136369$, 14 $\kappa = 0.136448$, 15 $\kappa = 0.136492$, 16 $\kappa = 0.136513$, 17 $\kappa = 0.136526$, 18 $\kappa = 0.136535$, 19 $\kappa = 0.136535$, 20 $\kappa = 0.136540$, 21 $\kappa = 0.136544$ (target κ reached!). The history of the corresponding acceptance rate and ΔH are displayed in fig. 4.5 and fig. 4.6, respectively.

The thermalization of the X7 ensemble was pursued further while the values for $\kappa = 0.136544$ and $\tau = 2.0$ are held fixed now. Plots of the average plaquette, the acceptance rate and ΔH are given in fig. 4.7, fig. 4.8 and fig. 4.9, respectively. Here, the vertical dashed lines indicate where new runs were started. The only exception is the last vertical line at $1148\mathrm{mdu}$ where we had to change the seed and the processor grid because the generation of the ensemble was migrated from JUQUEEN in Jülich to MOGON II in Mainz.

Finally, the last chain labeled 'id115' resulted in the final ensemble on which we measured the correlators relevant for this study and studies conducted afterwards. As mentioned above, we dropped the first 200 configurations (i.e. $2000\mathrm{mdu}$) due to autocorrelation effects which is indicated by single dashed line in figs. 4.10, 4.11 and 4.12 which show the average plaquette, the acceptance rate and ΔH, respectively. It is noteworthy that, while the average plaquette seems to be thermalized, we do encounter low acceptance rates as well as high values of ΔH indicating that the ensemble has not

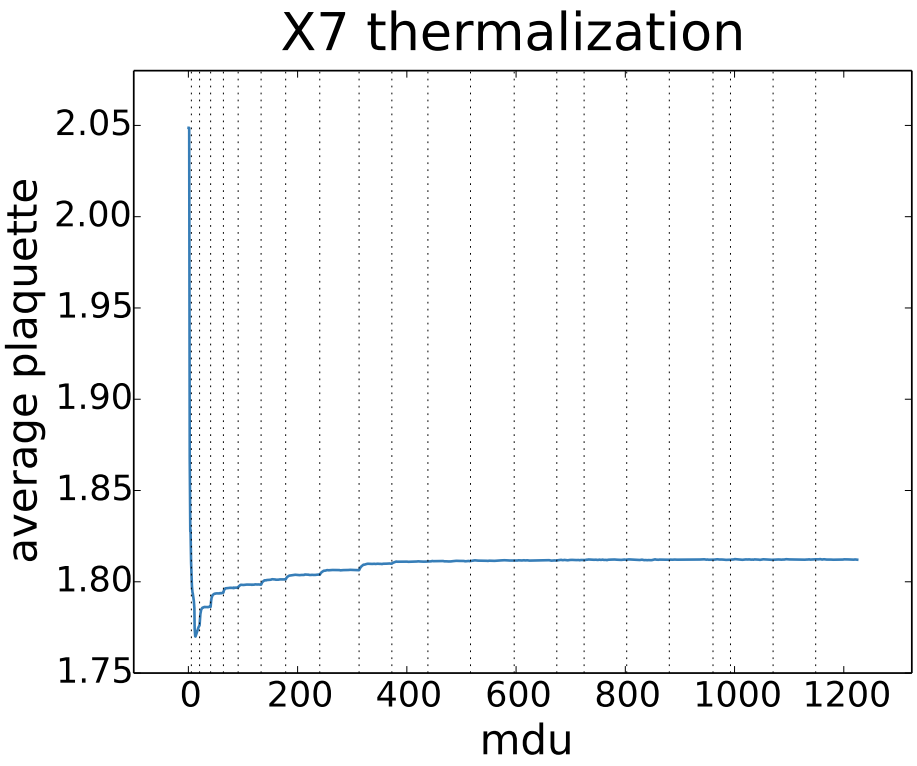

Figure 4.4: The average plaquette of the X7 ensemble during the initial thermalization phase starting from a thermalized, quenched configuration.

yet thermalized.

4.2 Correlators

For the computation of the photon production rate we examine a particular linear combination of the correlator according to eq. (6.6) in chapter 6 given by

$$G(x_0, \mathbf{k}) \equiv \left(\delta_{ij} - \frac{3k^i k^j}{k^2}\right) G_{ij}(x_0, \mathbf{k}) + 2\, G_{00}(x_0, \mathbf{k}) \tag{4.4}$$

with the isovector vector correlator

$$G_{\mu\nu}(x_0, \mathbf{k}) = \int \mathrm{d}^3x\, e^{-i\mathbf{k}\cdot\mathbf{x}} \left\langle V_\mu(x_0, \mathbf{x})\, V_\nu^\dagger(0, \mathbf{0})\right\rangle \tag{4.5}$$

and the vector current

$$V_\mu(x) = \bar{\psi}(x)\gamma_\mu\psi(x). \tag{4.6}$$

We can also define the static susceptibility

$$\chi_s \equiv \int_0^{L_0=1/T} \mathrm{d}x_0\, G^{00}(x_0, \mathbf{0}). \tag{4.7}$$

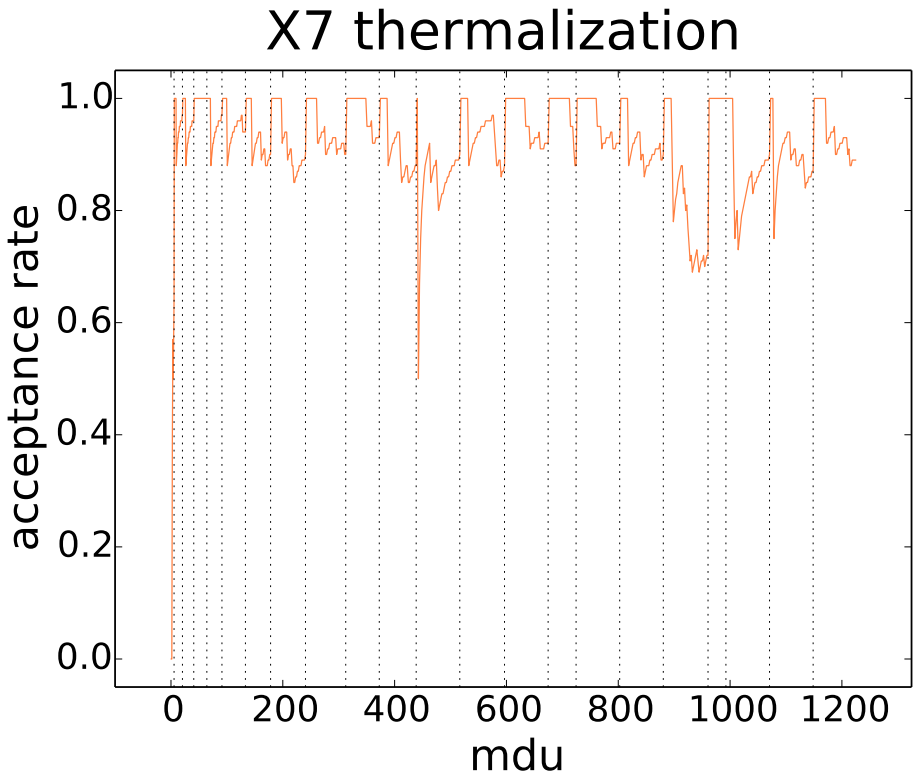

Figure 4.5: The acceptance rate of the X7 ensemble (see eqn. (4.2)) during the initial thermalization phase starting from a thermalized, quenched configuration.

The vector current can be defined with two different discretizations being the local and the conserved current

$$\begin{aligned} V_\mu^{\mathrm{l}}(x) &= \bar{\psi}(x)\gamma_\mu\psi(x) \\ V_\mu^{\mathrm{c}}(x) &= \frac{1}{2}\left[\bar{\psi}(x+a\hat{\mu})\,(1+\gamma_\mu)\,U_\mu^\dagger(x)\,\psi(x)\right. \\ &\quad \left.-\bar{\psi}(x)\,(1-\gamma_\mu)\,U_\mu(x)\,\psi(x+a\hat{\mu})\right]. \end{aligned} \tag{4.8}$$

The conserved vector current classically corresponds to the continuum version of the charge density evaluated at $x_\mu + a\hat{\mu}/2$, i.e. in the middle of two corresponding adjacent lattice points. This has to be dealt with carefully as described below.

Using the local and the conserved currents there are two discretizations of the correlator with only the local or only the conserved currents

$$G_{\mu\nu}^{\mathrm{ll}}(x_0,\mathbf{k}) = \int \mathrm{d}^3x\, e^{-i\mathbf{k}\cdot\mathbf{x}} \left\langle V_\mu^{\mathrm{l}}(x_0,\mathbf{x})\, V_\nu^{\dagger,\mathrm{l}}(0,\mathbf{0})\right\rangle \tag{4.9}$$

$$G_{\mu\nu}^{\mathrm{cc}}(x_0+a\delta_{\mu 0}-a\delta_{\nu 0},\mathbf{k}) = \int \mathrm{d}^3x\, e^{-i\mathbf{k}\cdot(\mathbf{x}+a\hat{\mu}/2-a\hat{\nu}/2)} \left\langle V_\mu^{\mathrm{c}}(x_0,\mathbf{x})\, V_\nu^{\dagger,\mathrm{c}}(0,\mathbf{0})\right\rangle \tag{4.10}$$

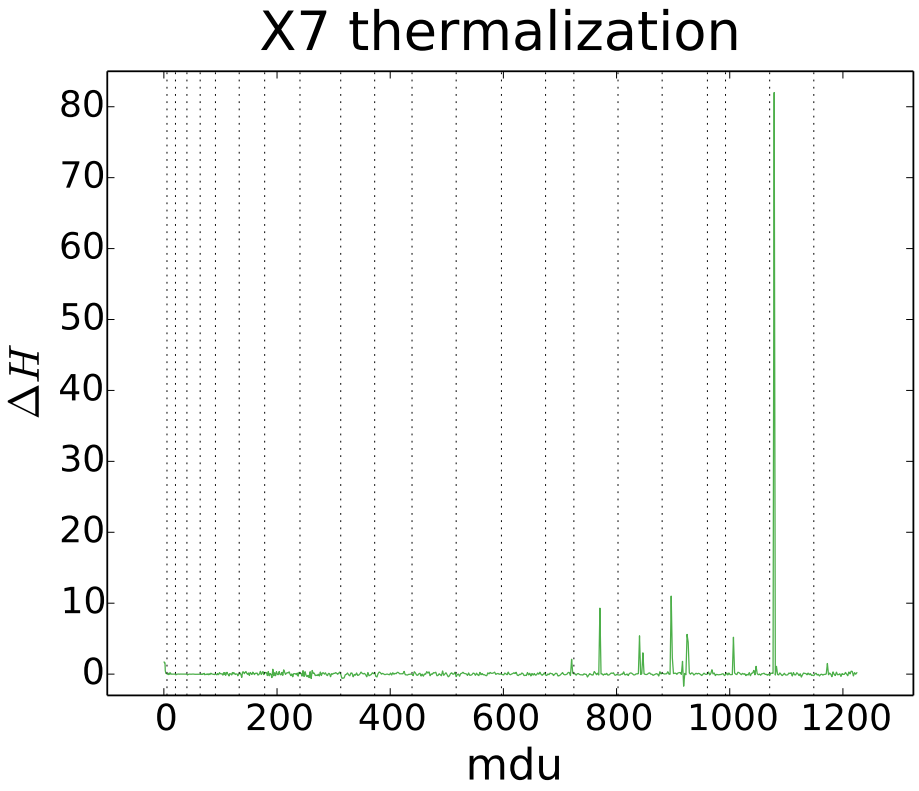

Figure 4.6: The ΔH (see around eqn. (2.68)) of the X7 ensemble during the initial thermalization phase starting from a thermalized, quenched configuration.

and the mixed discretization

$$G^{\mathrm{lc}}_{\mu\nu}(x_0 + a\delta_{\nu 0}, \mathbf{k}) = \int \mathrm{d}^3x\, e^{-i\mathbf{k}\cdot(\mathbf{x}-a\hat{\nu}/2)} \left\langle V^{\mathrm{l}}_{\mu}(x_0 + a\delta_{\nu 0}, \mathbf{x})\, V^{\dagger,\mathrm{c}}_{\nu}(0, \mathbf{0}) \right\rangle . \tag{4.11}$$

Then the local-conserved correlator transforms into the conserved-local correlator as $G^{\mathrm{lc}}_{\mu\nu}(x_0) \xrightarrow{T} G^{\mathrm{cl}}_{\nu\mu}(-x_0)$.

For the linear combination (4.4) we need to combine the component of the correlator with $\mu = \nu = 0$ with components having $\mu = i$ and $\nu = j$ located at the same temporal distance x_0. In case of the local-local or the conserved-conserved discretizations we can use (4.9) and (4.10) without further modifications. For the mixed local-conserved[3] discretization, however, there are two possible combinations for the computation of (4.4),

$$\begin{aligned} G^{\mathrm{lc,site}}_{00}(x_0, \mathbf{k}) &= \frac{1}{2}\left[G^{\mathrm{lc}}_{00}(x_0 + a/2, \mathbf{k}) + G^{\mathrm{lc}}_{00}(x_0 - a/2, \mathbf{k})\right] \\ G^{\mathrm{lc,site}}_{ij}(x_0, \mathbf{k}) &= G^{\mathrm{lc}}_{ij}(x_0, \mathbf{k}) \end{aligned} \tag{4.12}$$

[3]The conserved-local discretization behaves analogously. So we restrict the discussion to the local-conserved discretization for brevity.

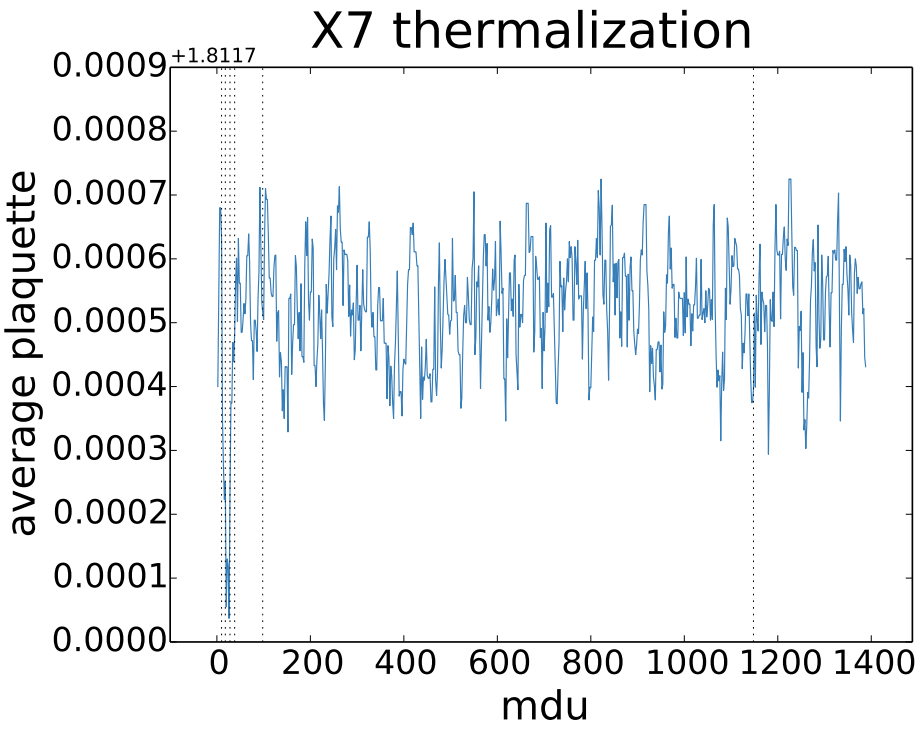

Figure 4.7: The average plaquette of the X7 ensemble during thermalization.

where the different components are added when evaluated at the site, as well as

$$\begin{aligned} G_{00}^{\mathrm{lc,link}}(x_0 + a/2, \mathbf{k}) &= G_{00}^{\mathrm{lc}}(x_0 + a/2, \mathbf{k}) \\ G_{ij}^{\mathrm{lc,link}}(x_0 + a/2, \mathbf{k}) &= \frac{1}{2}\left[G_{ij}^{\mathrm{lc}}(x_0, \mathbf{k}) + G_{ij}^{\mathrm{lc}}(x_0 + a, \mathbf{k})\right] \end{aligned} \tag{4.13}$$

where the components are evaluated at the midpoint of the links before adding them.

Now we have four different discretizations at hand $X = \{\mathrm{ll},\ \mathrm{cc},\ (\mathrm{lc}, \mathrm{site}),\ (\mathrm{lc}, \mathrm{link})\}$. The corresponding correlators $G^X(x_0, \mathbf{k})$ are then symmetrized and averaged over their momentum orientations, the symmetrized correlators are denoted as $\bar{G}^X(x_0, k)$. We have to take into account the normalization of the local currents. This can be circumvented when we divide the bare correlators by the bare static susceptibility of the same discretization, i.e.

$$h^X(x_0, k) = \frac{\bar{G}^X(x_0, k)}{2\bar{\chi}_s^X(x_0)T} \tag{4.14}$$

where $\bar{\chi}_s^X(x_0) = L_0 \bar{G}_{00}^X(x_0, \mathbf{0})$. Then the renormalization factors cancel out and (4.14) is dimensionless.

In order to account for finite-volume effects, one may define the tree-level improved

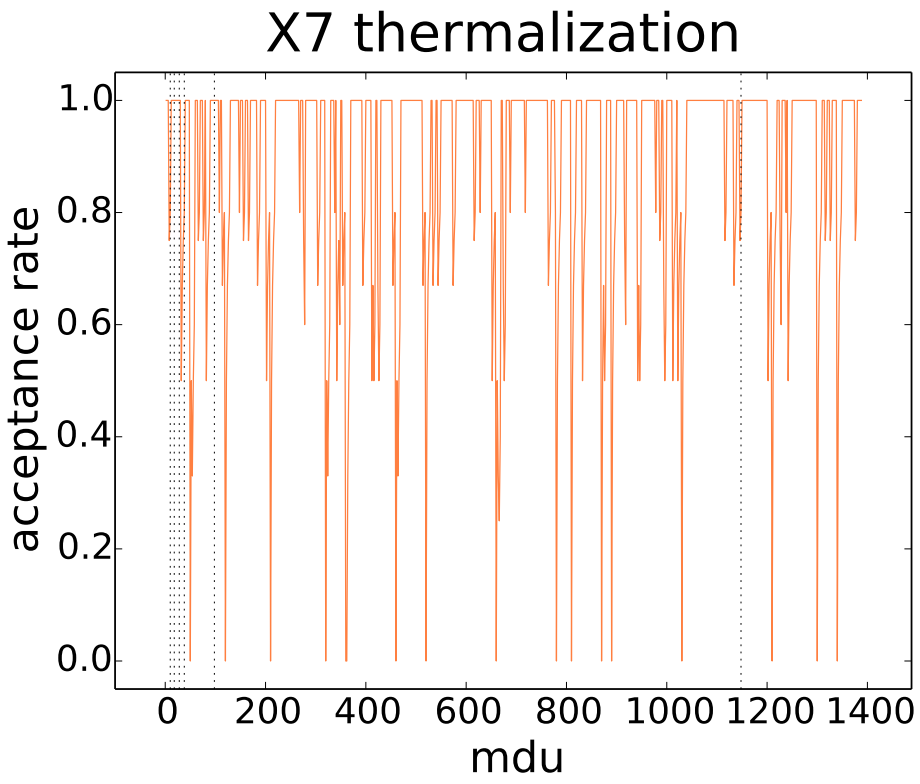

Figure 4.8: The acceptance rate of the X7 ensemble during thermalization, see eqn. (4.2).

version of $h^X(x_0, k)$ as

$$h^X_{\mathrm{TLI}}(x_0, k) = \frac{h_{\mathrm{cont}}(x_0, k)}{h^X_{\mathrm{lat}}(x_0, k)}\, h^X(x_0, k) \tag{4.15}$$

where h_{cont} is the tree-level continuum quantity of h and h^X_{lat} is the respective tree-level lattice version of it, both were computed by Xxxxx Xxxx.

The correlators at zero and finite momentum used for the analysis presented in chapter 5 were produced by the author using the `measure` code that was implemented by Xxxxxxx, Xxxxxxxxxx, Xxxxxxx, and modified within the Mainz lattice group by XXXX and XXX. The discretization of the isovector vector correlators was the local-conserved one. The correlators at different discretizations, the normalized quantity (4.14) as well as (4.15) that are relevant for the analysis presented in chapter 6, were produced, studied and analyzed by Xxx Xxxxx. He also produced the continuum limit presented in the following section.

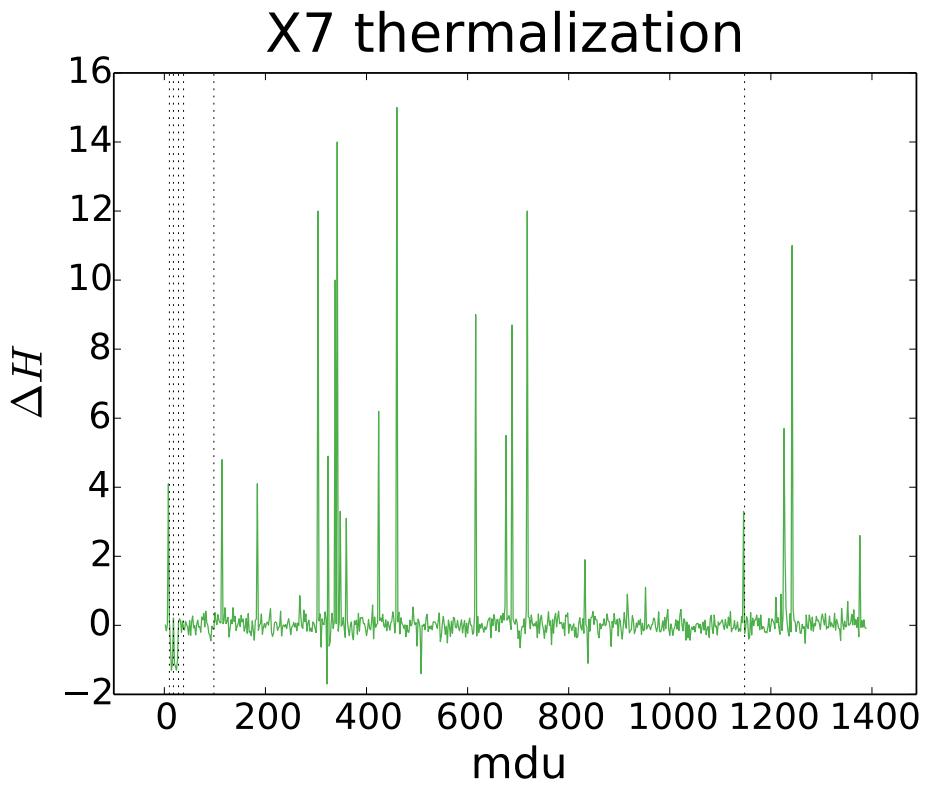

Figure 4.9: The ΔH (see around eqn. (2.68)) of the X7 ensemble during thermalization.

4.3 Continuum limit

For the continuum limit $a \to 0$ in general, the physical volume of the lattice box we are studying would shrink as a^4, unless one also sends $N_s \to \infty$ as well as $N_t \to \infty$ which is called the thermodynamic limit. This cannot be achieved within numerical simulations, so one restricts the continuum limit to the scaling analysis where one computes correlators at three different lattice spacings but with the same fixed physical box sizes and performs a cubic spline fit to extrapolate the lattice data to the continuum. What is presented in the following, is work done entirely by Xxx Xxxxxx.

The three lattice gauge ensembles labeled F7, O7, X7 can be used to form such a scaling analysis and subsequently a continuum limit of the quantity (4.14) with and without tree-level improvement. The lattice sizes of the three ensembles ($N_\tau = 12, 16, 24$ for F7, O7, X7, respectively) are not integer multiples of each other. Hence, one must construct an interpolator in x_0 for (4.14) and (4.15) at each fixed momentum k. This interpolation was performed using a cubic spline fit as implemented in the Python package `python.interpolate`. We choose to interpolate at the sites x_0 that correspond

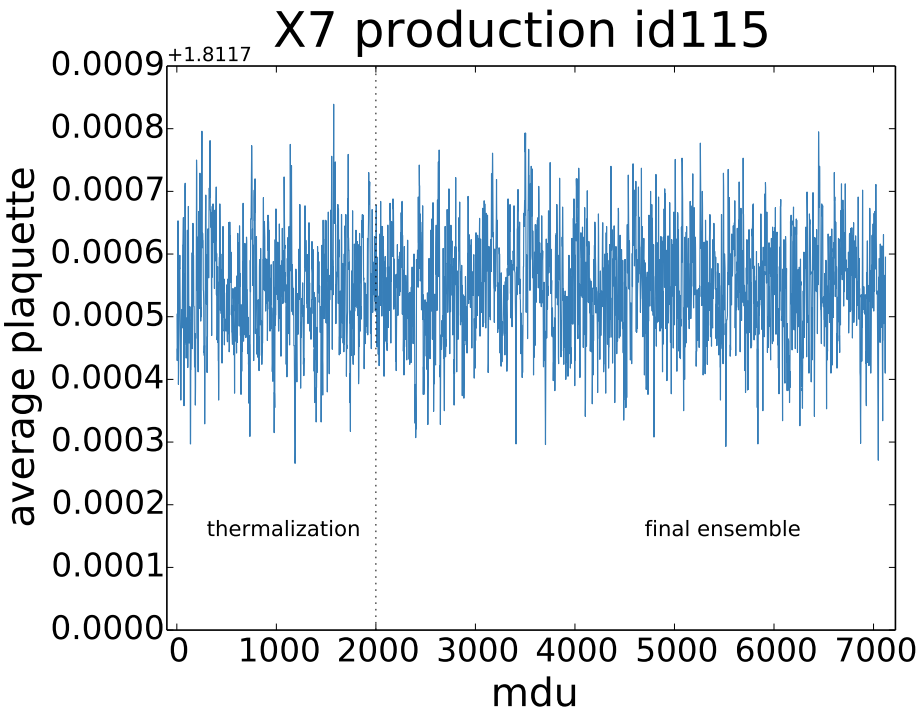

Figure 4.10: The average plaquette of the X7 ensemble with the final phase of thermalization and the final gauge ensemble. This chain is labeled 'id115'.

to the sites of the finest ensemble X7 in temporal direction.

Once the interpolants for the smaller lattices are determined, one can formulate a global least-squares problem for the continuum limit $\hat{h}(x_0, k)$ for all four discretizations of $h^X(x_0, k)$. At a fixed momentum k and a fixed distance x_0, one assumes the quadratic ansatz

$$h^X(x_0, k) = \hat{h}(x_0, k) + \frac{a^2}{L_0^2}\, s^X(x_0, k) \tag{4.16}$$

where the left-hand side is understood to be the interpolant while $\hat{h}(x_0, k)$ and $s^X(x_0, k)$ are the five fit parameters of the global fit. The fitting range is $x_0 = L_0/4 \ldots, L_0/2$ in steps of $a/N_\tau^{(\mathrm{X7})} = a/24$. Since the theory and the correlators are $\mathcal{O}(a)$ improved, we presume that the lattice estimator of h^X equals the continuum expression up to $\mathcal{O}(a^2)$ effects. That is why the ansatz (4.16) is well motivated. In general, there are $\mathcal{O}(a)$ effects due to spontaneous chiral symmetry breaking. At our temperature of $T = 254\,\mathrm{MeV}$, however, the system resides above the transition region around the chiral critical temperature of $T_c \approx 211(5)\,\mathrm{MeV}$ [65, 66] (for O7 parameters) where chiral symmetry is restored by definition. We can therefore safely neglect such effects as they are absent or at least strongly suppressed.

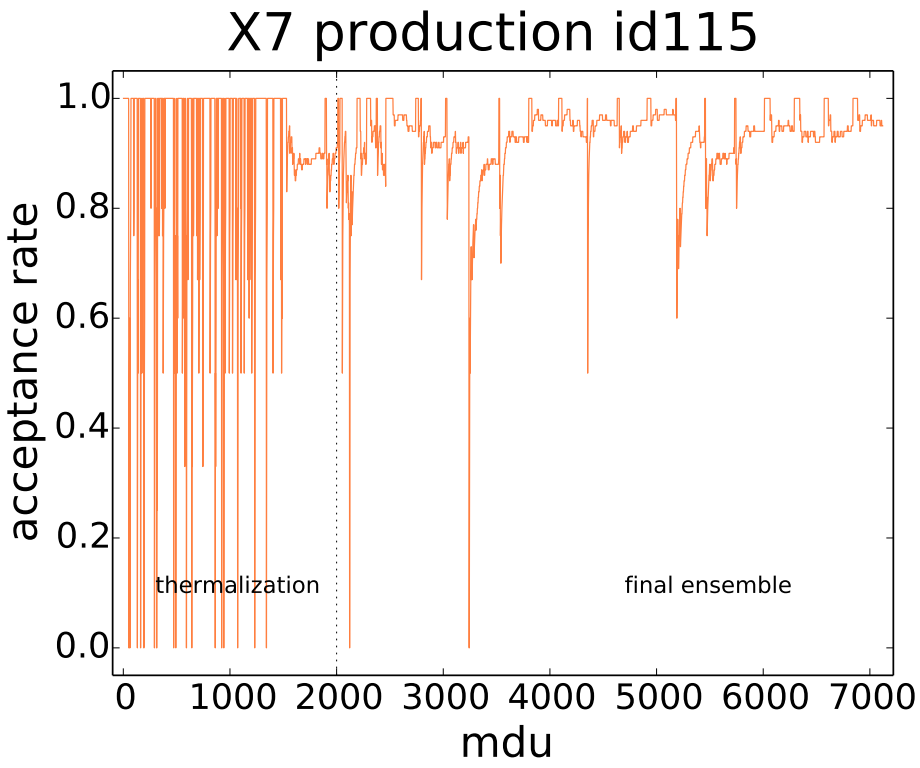

Figure 4.11: The acceptance rate of the X7 ensemble (see eqn. (4.2)) with the final phase of thermalization and the final gauge ensemble. This chain is lableed 'id115'.

For the observable given in eq. (4.14), the continuum extrapolation obtained via the ansatz (4.16) for the four discretizations at fixed temporal distance and momentum is shown in fig. 4.13. One can observe that the continuum limit for each of the four discretizations agrees such that discretization effects should be under control. While the upper panel of fig. 4.13 shows the data without tree-level improvement, the effect of multiplicatively improving the correlator according to (4.15) is depicted in the lower panel. Although the lattice data are corrected substantially, it is very reassuring that the continuum limit is not changed.

Finally, fig. 4.14 shows the continuum extrapolated correlators as functions of temporal distance τ/β (β equals inverse temperature) including tree-level improvement as open black symbols as well as the data at finite lattice spacing for the $N_\tau = 12, 16, 24$ ensembles (respectively F7, O7, X7) in red, green and blue for one fixed momentum $k\beta = \sqrt{4}\pi/2$. The corresponding interpolating functions are depicted as shaded bands and the three panels display the three discretizations conserved-conserved, local-local and local-conserved (site-centered), respectively. With the exception of points at distances $\tau/\beta < 0.25$, the data from the finest lattice X7 (blue) is already very close to the

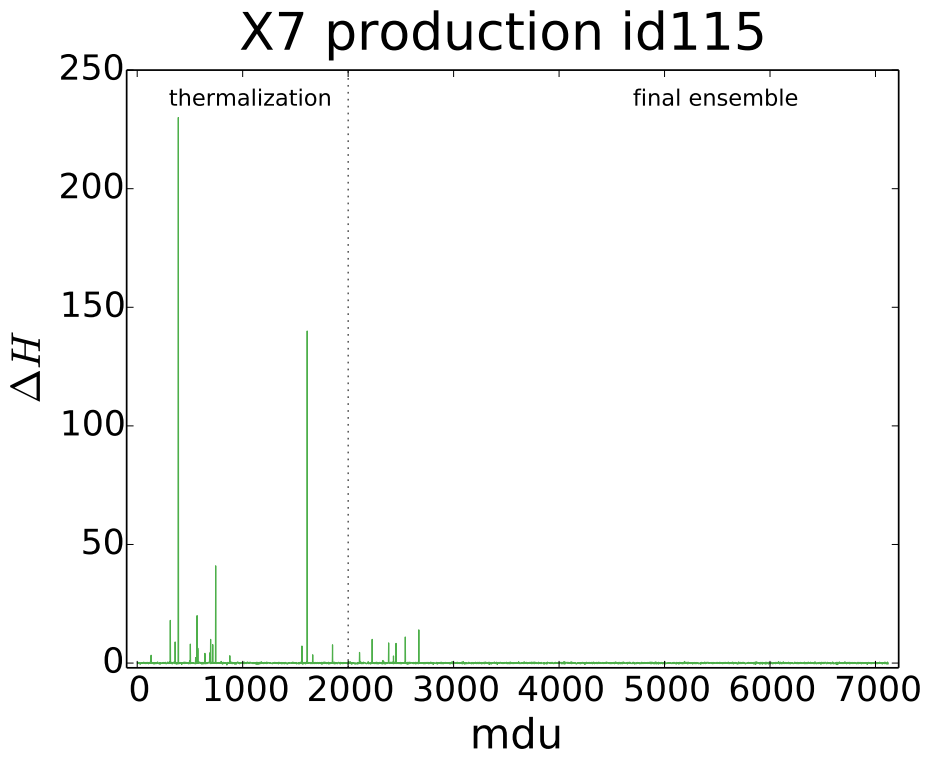

Figure 4.12: The ΔH (see around eqn. (2.68)) of the X7 ensemble with the final phase of thermalization and the final gauge ensemble. This chain is labeled 'id115'.

continuum extrapolated data set. Therefore the inclusion of this fine lattice is rather valuable for the study of cutoff effects. The results presented in chapter 6 are obtained from analyzing the continuum extrapolated data including tree-level improvement using the discretization with the site-centered local-conserved currents.

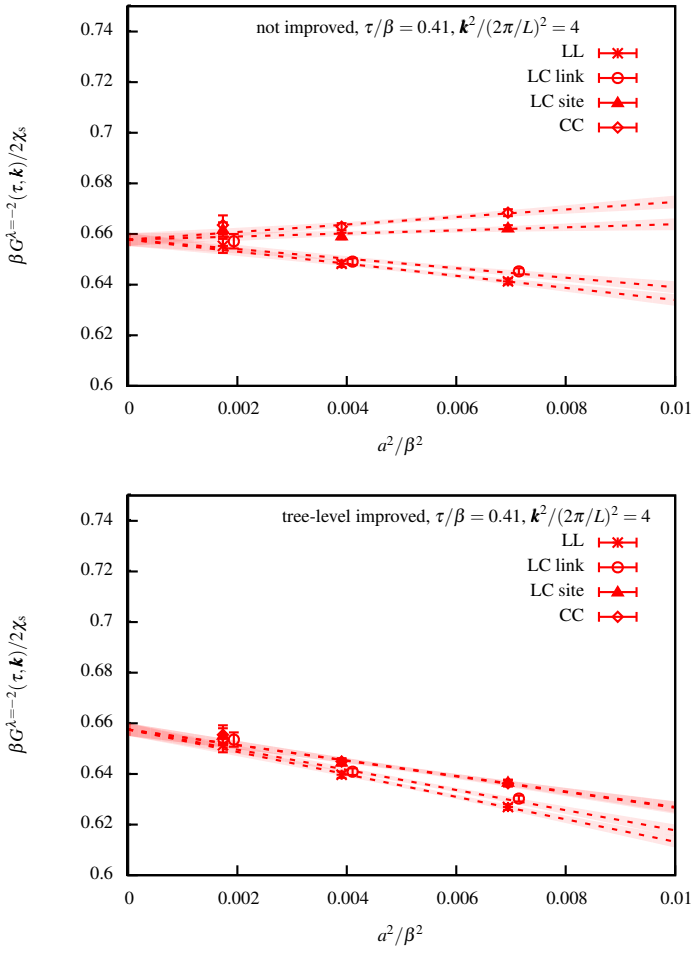

Figure 4.13: Continuum extrapolation of the observable (4.14) for all four discretizations at fixed temporal distance and momentum. The upper panel shows the non-improved quantity, while the lower one displays the tree-level improved one.

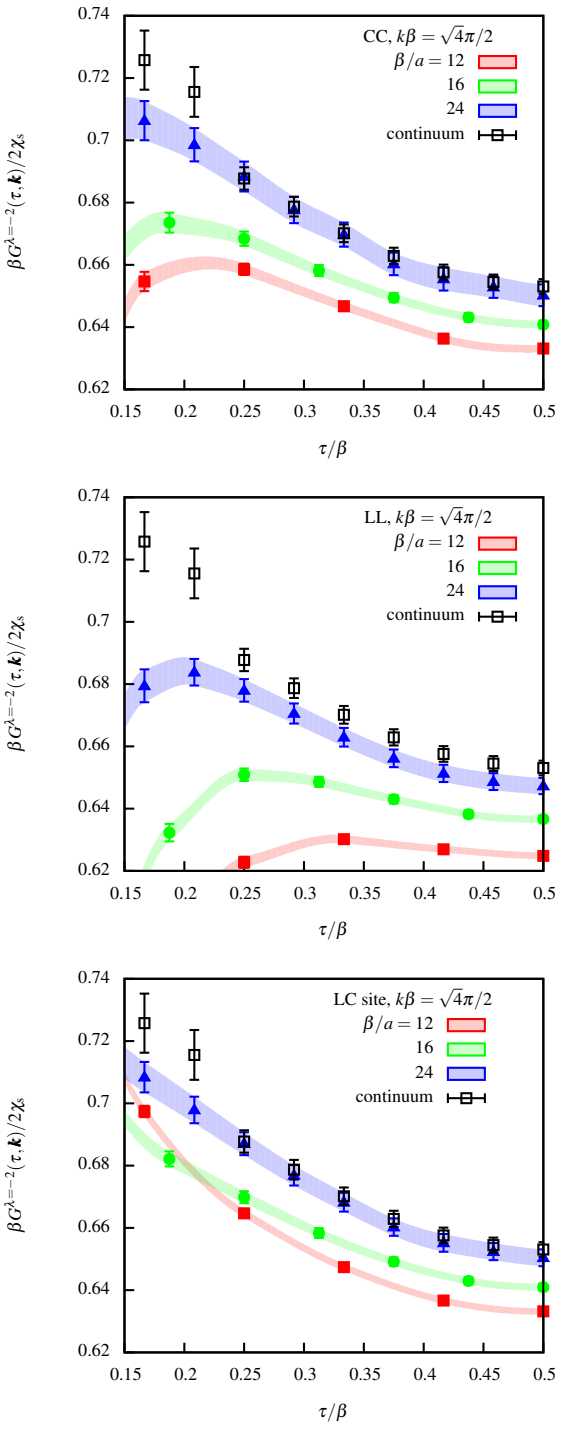

Figure 4.14: Plot of the lattice data at finite lattice spacing as well as the continuum extrapolated data for fixed momentum as a function of temporal distance τ/β where $\beta = 1/T$ stands for the inverse temperature. The three panels depict the three discretizations including the conserved-conserved, the local-local and the local-conserved (site-centered) currents, respectively.

Chapter 5

Thermal (screening) masses

This chapter is based on my previous work of Ref. [67] and most passages are kept unchanged for scientific clarity. The contribution of Xxxxxxx X. Xxxxxx and of Xxxxxxx Xxxxxxx comprises the providing of previously measured data used for comparisons and the introduction of the author to the MP-HMC algorithm as well as the `measure` code. The contribution of Xxx Xxxx consisted in multiple cross-checks of the fitting results and in pointing out a precision error in the fitting code as it was implemented by the author. The contribution of Xxxxxx Xxxxx was the supervision of the entire project.

5.1 The quark-gluon plasma

At vanishing baryon chemical potential, the phase transition from hadronic matter to the quark-gluon plasma (QGP) is predicted to be a rapid, but still continuous crossover. The hadrons in the medium undergo certain modifications as the temperature increases, this reflects the chiral and deconfinement properties of the system. The real-time, or transport properties of the medium, however, are connected to the correlators of conserved currents [68]. The spectral function in the channel of the conserved vector current can yield the thermal dilepton production rate and, when studied in the low frequency region, provides information about transport coefficients like the electrical conductivity or the diffusion coefficient by applying Kubo formulae. It is worth noticing that when one describes screening masses as a bound state of a non-relativistic quark-antiquark pair, one encounters the same effective potential that enters the calculation of the dilepton production rate [61, 69]. This will be discussed in more detail in section 5.2 and 5.4.

The thermal screening mass associated to the conserved vector current provides

an estimate for the inverse correlation length over which an electric field is screened in a strongly interacting medium, e.g. the QGP. Screening masses can as well be computed perturbatively in the high temperature regime of QCD and thus allow for a comparison between lattice and perturbative results. In terms of spectral functions, an analytic continuation of the screening pole in the Euclidean correlator to the diffusion pole in the retarded correlator establishes a link between screening masses and real-time quantities of QCD [70]. As described in section 6.3, relativistic hydrodynamics and linear response theory give a functional form for the retarded correlator at small frequency and momentum [70]

$$G_R(\omega, k) \overset{\omega,k\to 0}{=} \frac{\chi_s D k^2}{-i\omega + Dk^2}, \tag{5.1}$$

where χ_s is the static susceptibility and D the diffusion constant. Continuing to imaginary frequencies one obtains the Euclidean correlator $G_E(\omega_n, k) = G_R(i\omega_n, k)$ and the poles of (5.1) in k correspond to $iE(\omega_n)$, where $E(\omega_n)$ is the screening mass. Then, the poles are given by $k^2 = -\omega_n/D$ and the screening mass relates to the diffusion constant as [70]

$$E(\omega_n) \overset{\omega_n\to 0}{\sim} \sqrt{\frac{\omega_n}{D}}. \tag{5.2}$$

In [71], another motivation for studying screening states is given. It was shown that the lowest levels of transverse screening masses contribute to the vector correlator at light-like kinematics and therefore to the spectral function of interacting quarks. It is interesting to note that the difference of the screening mass from $2\pi Tn$ is relevant in that context, see also subsection 5.3.1 for further discussion. According to the findings in [61], it is argued that the photon emission rate discussed in chapter 6, recieves a strong contribution from infrared physics.

Within different gauge theories, there are different ways to define the Debye screening mass. In QED, for example, $k^2 + \Pi_{00}(0,k)|_{k^2=-m_E^2} = 0$ defines m_E, the static Debye screening mass as the pole of the longitudinal static photon self-energy [72]. For QCD, however, one extracts the chromo-electric Debye mass from the correlation function of the imaginary part of the trace of the Polyakov loop which is odd under Euclidean time-reversal [73]. Finally, the vector screening mass M_V explored in this work corresponds to the inverse of the screening length of an external $U(1)$ electric field in the QGP. One can extract it from the flavor non-singlet vector correlator determined from lattice QCD. The longest correlation lengths are gluonic at very high T, and the flavor-singlet quark bilinears have a very small overlap onto those states.

Thus, the disconnected contribution, i.e. the difference between singlet and non-singlet correlator, at high temperature, is expected to be negligible.

5.2 The effective formalism

It is of interest to investigate the screening of a $U(1)$ electric field inside the QGP where the intermediate screening state can be described by either an effective field theory or a lattice QCD approach. As discussed in Refs. [61, 74], an effective description of the system is motivated where one can exploit a scale hierarchy usually expressed as $g^2T \ll gT \ll 2\pi T$. Thus, the non-perturbative *ultrasoft* chromo-magnetic modes at scale $\sim g^2T$ are separated from the intermediate *soft* chromo-electric modes at $\sim gT$ [75]. Both these scales are integrated in the dimensionally-reduced effective theory we will employ whereas the *hard* scale $\sim 2\pi T$ enters through perturbative matching. The chromo-electric Debye screening mass m_E connected to the gT scale enters into an effective one-gluon exchange potential. One finds [75]

$$m_E^2 = g^2T^2\left(\frac{N_c}{3} + \frac{N_f}{6}\right). \tag{5.3}$$

The chromo-magnetic field, unlike in Abelian plasmas, is also screened on a scale of order g^2T determined by non-perturbative physics.

In accordance to the derivation in Ref. [61], the thermal flavor non-singlet vector current correlator is defined as

$$G_{\mu\nu}^{(k_n)} = \int_0^\beta \mathrm{d}\tau\, \mathrm{e}^{\mathrm{i}k_n\tau} \int_{\mathbf{x}} \left\langle \left(\,\bar{\psi}\gamma_\mu\psi\,\right)(\tau,\mathbf{x},\mathrm{z})\left(\,\bar{\psi}\gamma_\nu\psi\,\right)(0)\right\rangle, \tag{5.4}$$

where $\mathbf{x} = (x_1, x_2)^{\mathrm{T}}$ constitutes a transverse plane orthogonal to the z direction. After decomposing the quark fields into their Matsubara modes as

$$\bar{\psi}(\tau) = T\sum_{p_n} e^{-ip_n\tau}\,\bar{\psi}_{p_n}, \qquad \psi(\tau) = T\sum_{p_n} e^{ip_n\tau}\,\psi_{p_n}, \tag{5.5}$$

the screening correlator can be re-expressed as

$$G_{\mu\nu}^{(k_n)}(z) = T\int_{\mathbf{x}} \left\langle\, V_\mu^{(k_n)}(\mathbf{x},z)\, V_\nu^{(-k_n)}(0)\right\rangle, \tag{5.6}$$

where

$$V_\mu^{(k_n)}(\mathbf{x},z) = T\sum_{p_n} \bar{\psi}_{p_n}(\mathbf{x},z)\,\gamma_\mu\,\psi_{p_n-k_n}(\mathbf{x},z). \tag{5.7}$$

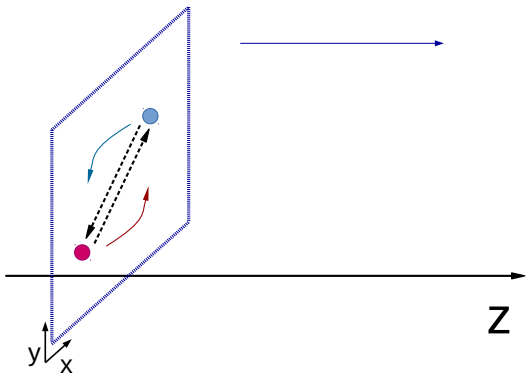

Figure 5.1: Non-relativistic auxiliary fields in the transverse plane exchanging one gluon. The quark-antiquark pair propagates in the z direction.

From [76], I quote the thermal masses for gluons and quarks, respectively,

$$m^2_{\mathrm{eff,g}} = \frac{1}{6}\left(C_A + N_f\, C_F\, \frac{d_F}{d_A}\right) g^2\, T^2 \equiv \frac{1}{2}\, m_D^2, \tag{5.8}$$

$$m^2_{\mathrm{eff,f}} = \frac{1}{4}\, C_F\, g^2\, T^2 \equiv 2\, m_F^2. \tag{5.9}$$

Fig. 5.1 depicts the quark and antiquark in the transverse plane. With the quark modes carrying frequencies of order $\sim \pi T$, the fields can be dimensionally reduced resulting in $2+1$-dimensional non-relatvistic fields,

$$\psi = \frac{1}{\sqrt{T}} \begin{pmatrix} \chi \\ \phi \end{pmatrix}. \tag{5.10}$$

This motivates a hydrogen-atom inspired picture for the two-quark bound state in an effective one-gluon exchange potential. In the transverse plane that is orthogonal to the screening direction z, the quarks perform a rotation around each other. Their chromo-electric Debye mass m_E enters in the one-gluon exchange potential,

$$V^+_{\mathrm{LO}}(\mathbf{y}) = \frac{g_E^2 C_F}{2\pi}\left[\log\left(\frac{m_E y}{2}\right) + \gamma_E + K_0(m_E y)\right], \tag{5.11}$$

where $g_E^2 = g^2 T$ is the effective coupling of our dimensionally reduced theory, $C_F = \frac{N_c^2-1}{2N_c}$, $y = |\mathbf{y}|$ and K_0 is a modified Bessel function. The same potential also occurs in the calculation of the dilepton production rate as was shown in [61, 69] and can be defined non-perturbatively. Following the steps carried out in [61], the determination of the effective screening mass requires the solution of the radial part of a homogeneous Schrödinger equation:

$$\left\{-\frac{d^2}{d\bar{y}^2} - \frac{1}{\bar{y}}\frac{d}{d\bar{y}} + \frac{l^2}{\bar{y}^2} + \rho\left(\frac{2\pi V^+_{\mathrm{LO}}}{g_E^2 C_F} - \hat{E}^{(l)}\right)\right\} R_l = 0 \tag{5.12}$$

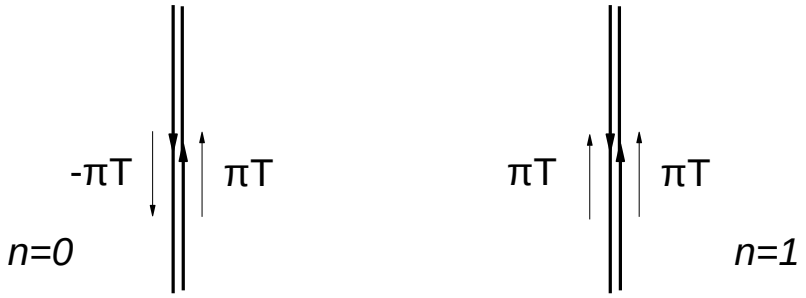

Figure 5.2: Left: static case ($n = 0$) with both quarks carrying momenta of πT each in opposing directions. Right: non-static case ($n = 1$) with both quarks carrying momenta of πT each in the same direction.

with dimensionless quantities $\bar{y} = m_E y$, $\rho = g_E^2 C_F M_r/(\pi m_E^2)$ and $g_E^2 = g^2 T$. At first, one needs to find the (physical) ground-state energy $\hat{E}^{(l)}$ of eqn. (5.12), which is used to compute the full energy $E_{\rm full}$ via

$$\begin{aligned} E_{\rm full} &= M_{cm} + \frac{g_E^2 C_F}{2\pi}\hat{E}^{(l)}\,, \\ M_{cm} &= k_n + \frac{m_\infty^2}{2M_r}\,, \quad m_\infty^2 = \frac{g^2 T^2 C_F}{4}\,, \quad M_r = \left(\frac{1}{p_n} + \frac{1}{k_n - p_n}\right)^{-1}. \end{aligned} \tag{5.13}$$

Finally, $E_{\rm full}$ can be regarded as the effective screening mass of the $U(1)$ electric field in the medium.

In addtion to the screening masses, one can study the screening amplitude. It is an estimate of how much the quark and the antiquark are overlapping. A large screening amplitude corresponds to a a tightly-bound screening state. For large distances, the screening correlator exhibits the behavior

$$\begin{aligned} -\frac{G_{00}^{(k_n)}(z)}{T^3} &\approx \frac{N_c m_E^2 \mathcal{A}_0^+}{\pi T^2} e^{-|z|E_0^{(l=0)}}\,, \\ -\frac{G_T^{(k_n)}(z)}{T^3} &\approx \frac{N_c m_E^4 \mathcal{A}_1^+}{\pi T^2}\left[\frac{1}{p_n^2} + \frac{1}{(k_n - p_n)^2}\right] e^{-|z|E_0^{(l=1)}} \end{aligned} \tag{5.14}$$

with

$$\mathcal{A}_0^+ = \frac{|R_0(0)|^2}{\int_0^\infty {\rm d}\bar{y}\bar{y}|R_0(\bar{y})|^2}, \qquad \mathcal{A}_1^+ = \frac{|R_1'(0)|^2}{\int_0^\infty {\rm d}\bar{y}\bar{y}|R_1(\bar{y})|^2} \tag{5.15}$$

for S-wave ($l = 0$) and P-wave ($l = 1$) channels, respectively.

In the static case, the situation is rather similar because both quarks carry momenta of πT but in opposing directions as illustrated in fig. 5.2. One needs to keep in mind that in the static and non-static sectors the role of the longitudinal and transverse

compontents of the current correlator are reversed and the interaction of the quark-antiquark pair is described by a different potential.

5.3 Lattice calculation

We simulate the system of interest on a lattice of space-time volume $V = (N_\tau a) \times (N_\sigma a)^3 = 16a \times (64a)^3$. Using previous lattice simulations with O7 parameters (see [61] and references therein) and the running of the coupling g_0^2 with the lattice spacing extrapolated from the data in Ref. [51], the lattice spacing is estimated to be $a \approx 0.024\,\mathrm{fm}$ corresponding to a temperature of $T = (N_\tau a)^{-1} \cong 508\,\mathrm{MeV}$. The lattice was generated with $N_f = 2$ non-perturbatively $\mathcal{O}(a)$-improved Wilson fermions. We use the plaquette gauge action with $\beta = 6/g_0^2 = 6.038$ [51]. The critical hopping parameter κ_c is extrapolated from the data in [54] keeping the 2-loop coefficients for $am_c = 1/(2\kappa_c) - 4$ obtained from [52, 53]. The clover term is set to $c_{\mathrm{sw}} = 1.51726$ using the non-perturbative tuning relations of [55]. With the chosen hopping parameter $\kappa = 0.136238$ we measure an $\overline{\mathrm{MS}}$ mass of $\overline{m}^{\overline{\mathrm{MS}}}(\mu = 2\mathrm{GeV})/T \approx 0.04$, whereby we follow the conversion of the bare subtracted quark mass to the $\overline{\mathrm{MS}}$ mass of [54]. The measurements were carried out exploiting $N_{\mathrm{cfg}} = 345$ configurations and $N_{\mathrm{src}} = 64$ random sources.

We describe the screening correlator of eqn. (5.4) by a two-state fit,

$$G_{\mu\nu}^{(k_n)}(z) \;=\; \sum_{n=1}^{2} A_n \frac{\cosh[M_n(z - L_z/2)]}{\sinh[M_n L_z/2]}. \tag{5.16}$$

The effective screening mass M_1 we extract from the fit is an estimate for the inverse screening length of the $U(1)$ electric field in the QGP and the excited-state mass M_2 corrects for the leading excited-state contamination at long distances.

5.3.1 Comparison of results

We are now in the position to compare the results of the two approaches in order to determine how well the effective perturbative description coincides with the lattice data. In a previous study [61] this comparison was done for temperatures of $T = 254\,\mathrm{MeV}$ and $T = 338\,\mathrm{MeV}$. In the static transverse channel the lattice result lies below the $2\pi T$-line for both temperatures whereas the perturbative result lies above it. The tendency, however, of the lattice data is to eventually cross the $2\pi T$-line at a certain temperature. This behaviour is confirmed by the new lattice data set at $T = 508\,\mathrm{MeV}$, shown in the

upper panel of fig. 5.3. This observation is consistent with the expectation that, the higher the temperature, the more accurate the perturbative description becomes. The agreement is less good in the static longitudinal channel, see fig. 5.3, while in both cases the perturbative results differ from the lattice data by less than 10%. The results obtained by the two different approaches in the non-static longitudinal channel with $n = 1$ agree quantitatively, see fig. 5.4 (upper panel). Both values are above $2\pi T$ and are compatible within errors. In the transverse channel of the non-static vector screening correlator the two effective masses are close although the lattice signal deteriorates as z approaches $L_z/2$, see also fig. 5.4.

Figure 5.5 gives an overview of the spectra at $T = 254,\ 338$ and $508\,\mathrm{MeV}$. It is evident that the agreement between lattice field theory and effective field theory is improved for higher temperatures. For the highest temperature, in the static sector, $n = 0$, the transverse effective mass lies above the $2\pi T$-line, in qualitative agreement with perturbation theory, and in the non-static sector, $n = 1$, the longitudinal effective masses obtained from an effective and a lattice approach agree quantitatively. Since the coupling is smaller for higher temperatures, the difference from $2\pi T$ for the perturbative results decreases with higher temperatures whereas the lattice data stays the same, as can be seen in the longitudinal channel of the static sector, $n = 0$. The perturbative results in both the longitudinal and the transverse channel of the non-static sector, $n = 1$, at $T = 508\,\mathrm{MeV}$ are systematically shifted to lower values compared to the same data at the lower temperatures $T = 254$ and $338\,\mathrm{MeV}$. For these temperatures a non-perturbative EQCD potential enhanced the agreement of lattice QCD and effective field theory results in the non-static sector, $n = 1$, whereas only a leading order potential was available for the comparison at $T = 508\,\mathrm{MeV}$.

Interpreting the amplitudes, as obtained from eqn. (5.15) and the lattice formulation, eqn. (5.16), in terms of the quark-antiquark picture, they give an estimate on how tightly bound the quark-antiquark pair is. At the lower temperatures examined in Ref. [61] the amplitudes were higher compared to the present study. In this picture, this indicates that at higher temperatures the two quarks are more loosely bound; the bound state is more extended in the (x, y) plane. Although the agreement between lattice and effective field theory is worse than for the masses (see fig. 5.6), there is noticeable improvement when comparing to the results gained for the amplitudes in the previous study [61] at a lower temperature. As compared to the masses, it is more difficult to establish good agreement between lattice and perturbative results for the amplitudes. This is because the leading order value of the mass scales as $2\pi T$ whereas

	$T/\,\mathrm{MeV} = 254$		$T/\,\mathrm{MeV} = 338$		$T/\,\mathrm{MeV} = 508$	
	$n=0$	$n=1$	$n=0$	$n=1$	$n=0$	$n=1$
$E_T/(2\pi T)$	0.917(6)	1.488(32)	0.970(2)	1.509(21)	1.012(2)	1.296(75)
$E_{00}/(2\pi T)$	1.272(32)	1.186(10)	1.261(14)	1.154(2)	1.259(12)	1.136(2)
A_T/T^3	10.3(4)	9.2(16)	10.63(13)	10.0(12)	10.972(181)	1.642(1.430)
A_{00}/T^3	7.9(7)	6.0(4)	4.1(16)	4.78(7)	5.472(645)	3.751(137)

Table 5.1: Lattice results for the energies and matrix elements. The results for $T = 254, 338\,\mathrm{MeV}$ are from Ref. [61], the results for $T = 508\,\mathrm{MeV}$ are from this work.

	$T/\,\mathrm{MeV} = 254$		$T/\,\mathrm{MeV} = 338$		$T/\,\mathrm{MeV} = 508$	
	$n=0$	$n=1$	$n=0$	$n=1$	$n=0$	$n=1$
$E_T/(2\pi T)$	1.082(16)	1.464(32)	1.066(16)	1.416(32)	1.068(5)	1.183(8)
$E_{00}/(2\pi T)$	1.210(16)	1.273(32)	1.194(16)	1.241(16)	1.172(8)	1.130(6)
A_T/T^3	17.8(22)	1.2(4)	15.7(14)	1.0(2)	14.091(399)	0.084(6)
A_{00}/T^3	0.7(2)	3.8(5)	0.5(1)	3.3(3)	0.429(28)	1.225(58)

Table 5.2: Perturbative results for the energies and matrix elements. The results for $T = 254, 338\,\mathrm{MeV}$ are from Ref. [61], the results for $T = 508\,\mathrm{MeV}$ are from this work.

the amplitudes scale as $\sim g^2$ or $\sim g^4$, and are thus more sensitive to uncertainties in the value of the running coupling.

For the three different temperatures $T = 254, 338, 508\,\mathrm{MeV}$, the results of the energies and matrix elements are given in Table 5.1 as obtained from the lattice, and in Table 5.2 as obtained from the perturbative theory. In both cases, the left and middle columns show results for $T = 254, 338\,\mathrm{MeV}$ as presented in Ref. [61], while the right column displays the results from this work.

Finally, one can compare all the results from the lattice and the peturbative treatment with $\mathcal{N} = 4$ SYM theory at infinite coupling. There the non-static screening energy in the $n = 1$ Matsubara sector at $2\pi T$ in the longitudinal (S-wave) channel lies at [77]

$$E_L^{(n=1)} = 1.338 \cdot 2\pi T. \tag{5.17}$$

Because AdS/CFT is scale invariant, this result is valid for all temperatures. Comparing to the corresponding screening masses obtained from the lattice theory at different temperatures, one observes that for all three temperatures discussed here, the $\mathcal{N} = 4$ SYM result differs from the lattice results by at least 10% to about 15%, a substantial

amount compared to the given precision. The same comparison with respect to the screening masses obtained from the perturbative theory leads to a different conclusion. In this case, the $\mathcal{N}=4$ SYM results differ from the PT results by at most 5% for the temperatures $T = 254, 338\,\mathrm{MeV}$. This shows how high the precision in the lattice and the perturbative appraches needs to be so that one can actually distinguish between the weak-coupling and the AdS/CFT prediction. At the highest temperature $T = 508\,\mathrm{MeV}$, however, the perturbative result is compatible with the lattice result within error bars and therefore the deviation from the AdS/CFT value is again about 15%. The reason for this discrepancy is that there was an EQCD potential used to determine the EFT screening masses at the two lower temperatures but it is the LO perturbative potential that provides the screening masses at the highest temperature, see Ref. [61] and references therein for further discussion of the two potentials.

5.4 Connecting screening masses to the photon emission rate

Let us denote the transverse part of the spectral function evaluated on the light cone as $\sigma(\omega) \equiv \rho_{\mathrm{T}}(\omega, |\mathbf{k}| = \omega)$, this is in fact the naturally relevant component of the spectral function directly proportional to the photon emission rate. We can also denote the momentum-space Euclidean correlator in the Matsubara sector ω_n at *imaginary* spatial momentum $k = i\omega_n$ as $H_{\mathrm{E}} \equiv G_{\mathrm{E}}(\omega_n, k = i\omega_n)$. Then both these objects are related by a dispersion relation

$$H_{\mathrm{E}}(\omega_n) - H_{\mathrm{E}}(\omega_r) = \int_0^\infty \frac{\mathrm{d}\omega}{\pi}\,\omega\,\sigma(\omega)\left[\frac{1}{\omega^2+\omega_n^2} - \frac{1}{\omega^2+\omega_r^2}\right]. \tag{5.18}$$

When the Fourier transformed Euclidean screening correlator is expressed via a sum of screening states with energies E_n as

$$\begin{aligned}\tilde{G}_{\mathrm{E}}(\omega_r, x_3) &= -\sum_{i=1}^{2}\int_0^\beta \mathrm{d}x_0\, e^{\,i\omega_r x_0}\int \mathrm{d}x_1\mathrm{d}x_2\,\langle J_i(x)J_i(0)\rangle \\ &= \sum_n A_n^{(r)} e^{-E_n^{(r)}|x_3|}\,,\end{aligned} \tag{5.19}$$

then H_{E} is given as

$$\begin{aligned}H_{\mathrm{E}}(\omega_r) &\equiv \int_{-\infty}^{\infty}\mathrm{d}x_3\,\tilde{G}_{\mathrm{E}}(\omega_r, x_3)\,e^{\,\omega_r x_3} \\ &= 2\,\omega_r^2\sum_{n=0}^{\infty} A_n^{(r)}\frac{1}{E_n^{(r)}(E_n^{(r)2}-\omega_r^2)}.\end{aligned} \tag{5.20}$$

Thus, with eqns. (5.18) and (5.20), one establishes a connection between the spectral function related to the photon emission rate and non-static screening masses. This helps to understand why the same effective potential occurs both in the computation of quark-antiquark screening states and the Landau-Pomeranchuk-Migdal resummation contributions to dilepton production rates [78], as was mentioned earlier in Ref. [61].

5.5 Brief summary and outlook

A general result of this study is that a quark-antiquark pair in the flavor non-singlet vector channel can be described as a non-relativistic bound state (bound by an effective one-gluon exchange potential) with the size of $\mathcal{O}(m_E^{-1})$ where m_E is the chromo-electric Debye screening mass. The corresponding screening amplitudes indicate that the quark-antiquark pair is more loosely bound at high temperatures than at lower ones. The effective screening mass determined for this intermediate state is an estimate for the inverse correlation length over which a $U(1)$ electric field is screened in the medium. While both the static and non-static sectors probing the momentum scale gT can be represented by an effective theory in $2+1$ dimensions, only the non-static sector can be clearly connected to real-time phenomena, see Ref. [61] and section 5.4. The same effective potential that appears in the description of non-static screening masses also enters the computation of the dilepton production rate.

The agreement between lattice and effective theory results confirms the applicability of the perturbative treatment at temperatures that are relevant for heavy-ion phenomenology. A previous study [61] implies that the lattice results in the transverse channel of the static sector would cross the $2\pi T$ line from below for increasing temperatures, thereby improving agreement with results from perturbation theory which lie above the $2\pi T$ line, see fig. 5.5. This behavior was observed in an earlier study using staggered fermions [79] and is confirmed by the results of this work using $\mathcal{O}(a)$ improved Wilson fermions, see right columns of Tables 5.1 and 5.2.

One possible future application of this study is an analytic continuation of the retarded correlator in the Matsubara frequency in order to extract the diffusion coefficient, see Refs. [70, 69] and Eq. 5.2. Finally, and in view of the following chapter 6, it is noteworthy that the so-called reconstructed correlator is of interest when examining thermal correlators and their corresponding spectral functions [80, 81]. The reconstructed correlator can be thought of as the Euclidean correlator at temperature T for which the spectral density is not affected by thermal effects [80].

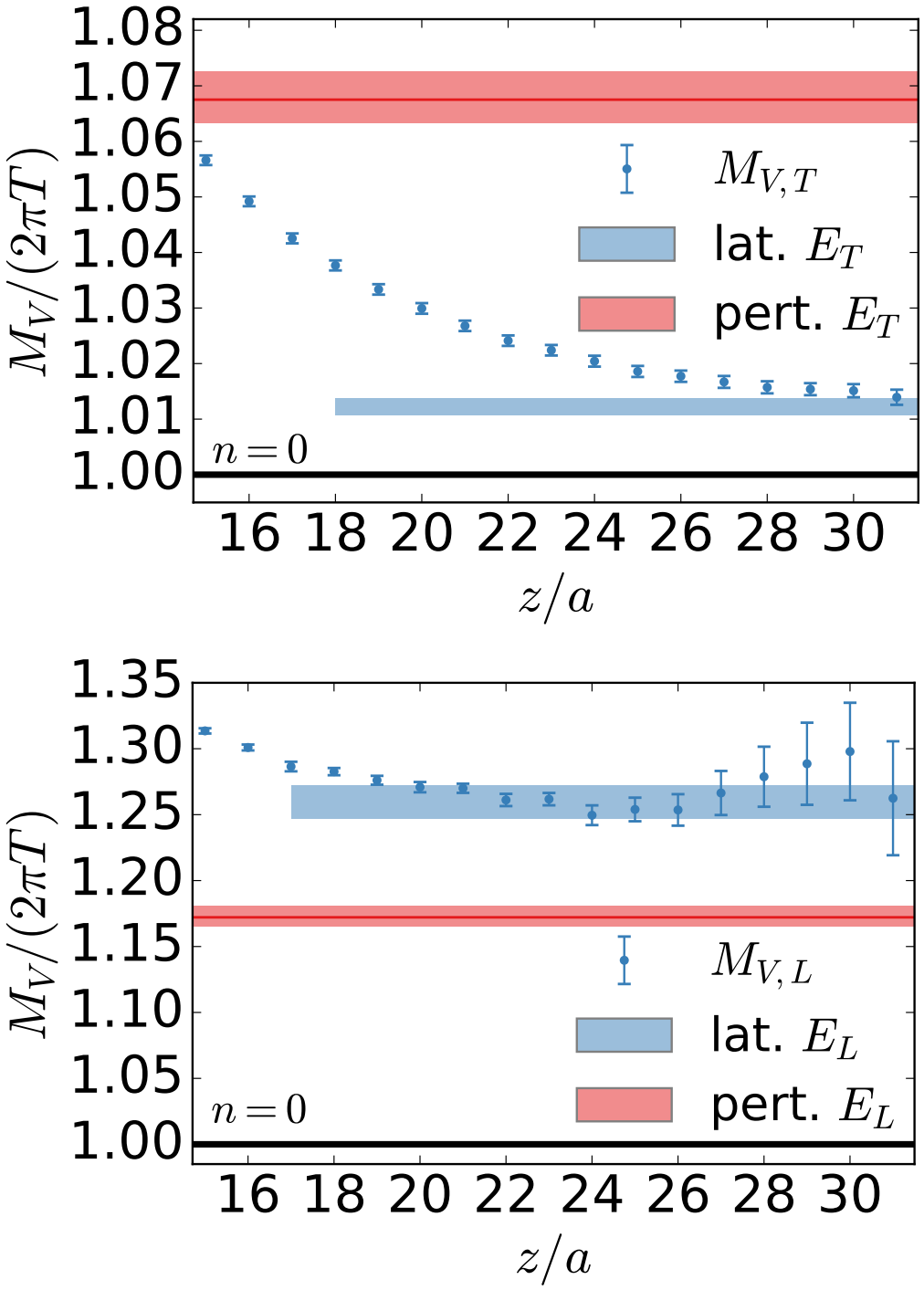

Figure 5.3: Static $(n = 0)$ screening masses at a temperature of $T = 508\,\mathrm{MeV}$. Upper panel: transverse (S-wave) channel. Lower panel: longitudinal (P-wave) channel.

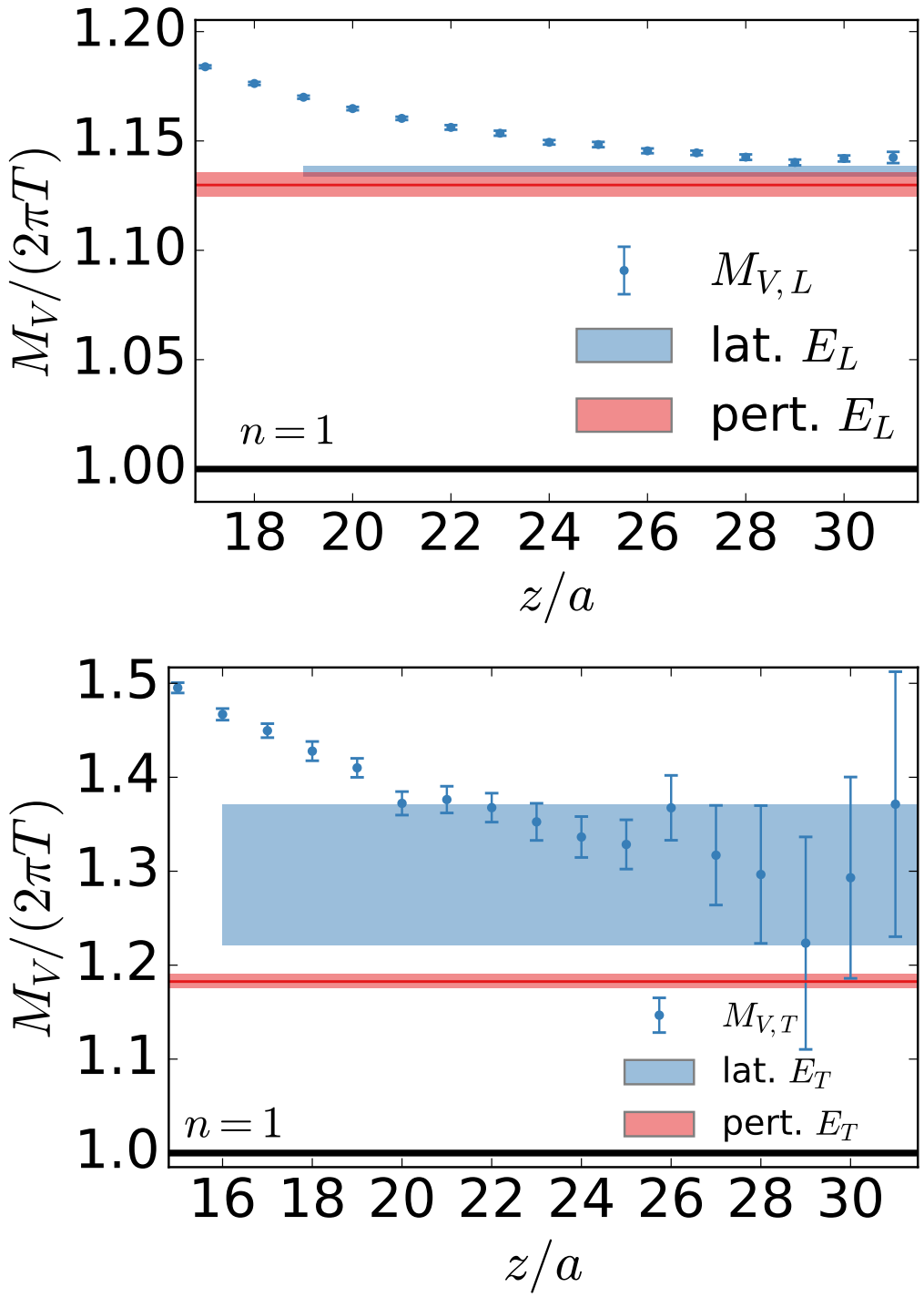

Figure 5.4: Non-static (n=1) screening masses at a temperature of $T = 508\,\mathrm{MeV}$. Upper panel: longitudinal (S-wave) channel. Lower panel: transverse (P-wave) channel.

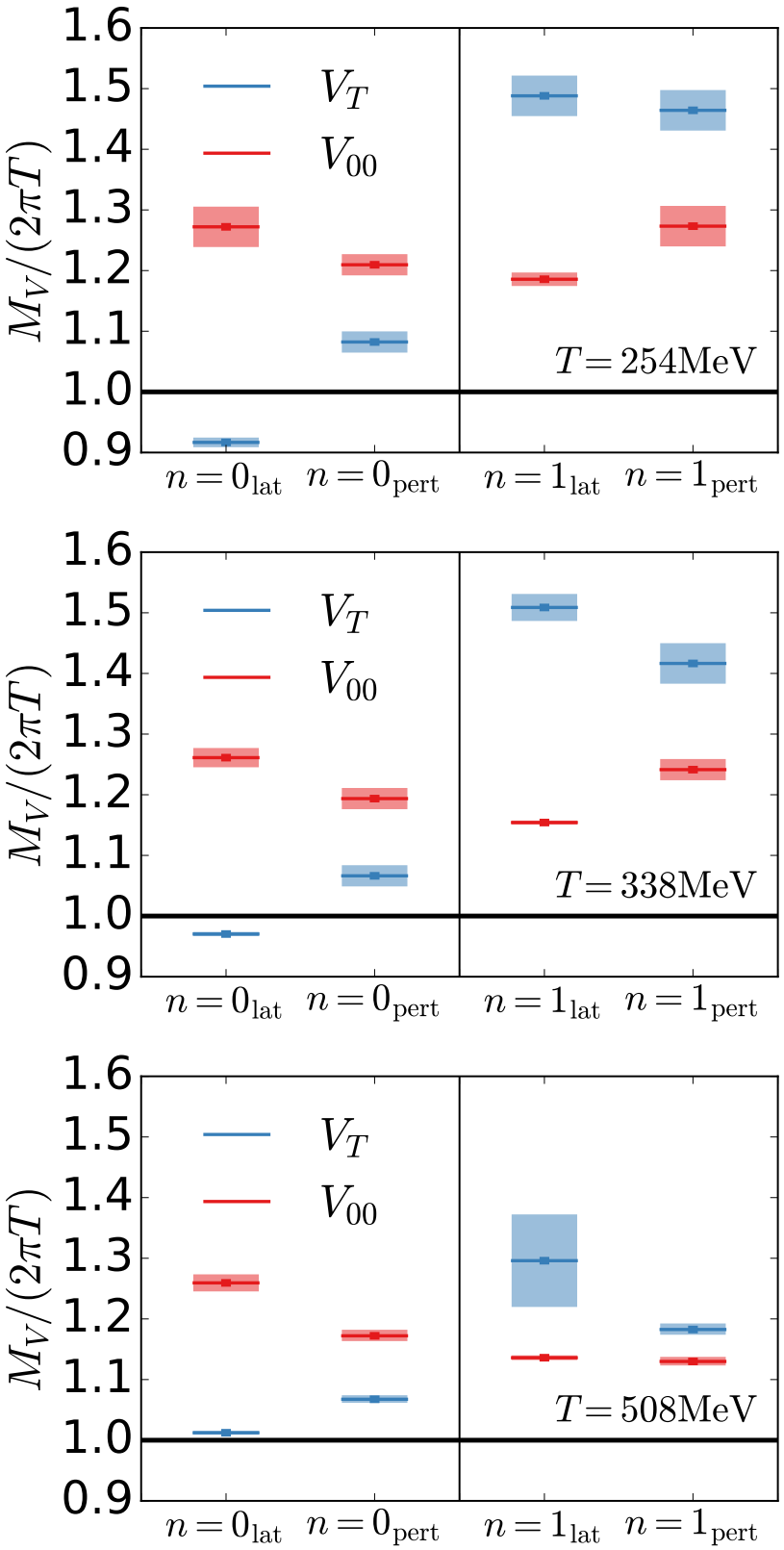

Figure 5.5: Comparison of the masses at different T. Results of the upper and middle panels are from [61].

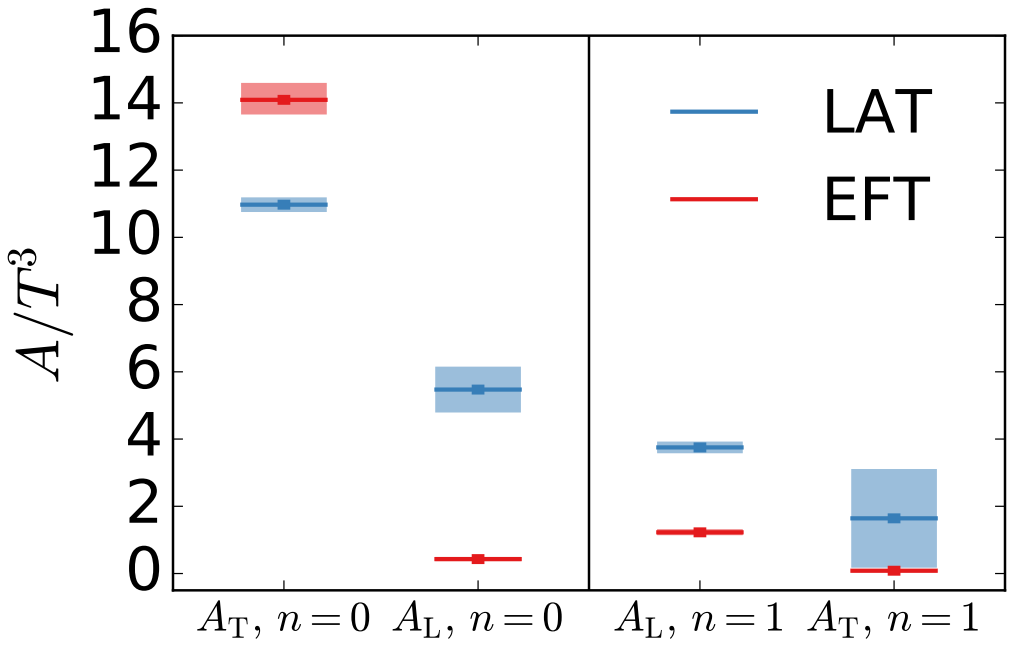

Figure 5.6: Comparison of the amplitudes at $T = 508\,\mathrm{MeV}$.

Chapter 6

The photon production rate

As described in [82], particles that interact electromagnetically, such as photons or dileptons, have little cross sections with the QGP. In plasmas of the extent produced in relativistic heavy-ion collisions, the photons probe the entire medium without too many rescatterings before they are detected. In contrast, strongly interacting constituents of the plasma suffer many rescatterings with the medium over their lifetime in the QGP, and therefore information about the initial properties of these constituents is obscured.

Hence, it is important to study direct photons, which are produced from the very early stages of a collision onward and escape the medium without having thermalized or rescattered [83]. In this way, the information they carry about the initial stages of the collision is not wiped out. Direct photons can be grouped into prompt and thermal photons. Prompt photons are produced when the partons that make up the heavy ions collide. Thermal photons are emitted by the hot quark or hadronic matter generated during the collision process [83]. When the hadrons in the medium decay radiatively, this gives rise to a background contribution of decay photons that are not direct photons. Only thermal photons, however, provide information about the early stages of the QGP [83], so they are the ones we want to study.

6.1 Correlators and spectral functions

Information about the response of an observable to the influence of an external source is usually extracted from a retarded correlator [46]. Linear response theory deals with the response of an equilibrated thermal medium to small perturbations out of equilibrium.

When studying the expectation value of a commutator and exploiting time-translation invariance of the equilibrium density matrix, the spectral function is directly related to

the retarded correlator [46]. It can be shown that one obtains the frequency-space Euclidean correlator by an analytic continuation of the retarded correlator [46].

In order to reconstruct the spectral function, ρ, from a discrete Euclidean correlator, G, it is necessary to invert an integral equation [68] (see also eqn. (1.37)),

$$G(\tau, T) = \int_0^\infty \frac{\mathrm{d}\omega}{2\pi}\, \rho(\omega, T)\, K(\omega, \tau, T), \tag{6.1}$$

where the finite temperature integration kernel reads

$$K(\omega, \tau, T) = \frac{\cosh\left(\omega\left(\tau - \beta/2\right)\right)}{\sinh\left(\omega\beta/2\right)}. \tag{6.2}$$

This inversion problem becomes numerically ill-posed when there are only about $\mathcal{O}(10)$ data points available on the l.h.s. of eqn. (6.1) but one would need many more points to resolve the spectral function, ρ [68]. Two alternate ways of dealing with this ill-posed numerical situation are discussed in sections 6.4 and 6.5.

6.2 Definitions

The differential photon production rate per unit volume of plasma is given, to leading order in the electromagnetic coupling α_{em}, by [82, 84]

$$k\,\frac{\mathrm{d}\Gamma_\gamma(k)}{\mathrm{d}^3 k} = \left(\sum_{f=1}^{N_{\mathrm{f}}} Q_{\mathrm{f}}^2\right) \frac{\alpha_{\mathrm{em}}}{4\pi^2}\; n_{\mathrm{B}}(\omega = k)\, \rho^\mu{}_\mu(\omega = k, \mathbf{k}), \tag{6.3}$$

where $n_{\mathrm{B}}(\omega)$ is the Bose-Einstein distribution. This rate is determined by the vector-vector spectral function, $\rho^\mu{}_\mu$ evalutated on the light cone, $\omega = k$.

The Ward identity connected with vector current conservation reads

$$\omega^2 \rho^{00} - k^i k^j \rho^{ij} = 0. \tag{6.4}$$

Thus, on the light cone

$$\rho^{00} - \frac{k^i k^j}{k^2}\rho^{ij} = 0. \tag{6.5}$$

It proves helpful to consider the linear combination

$$\rho_\lambda(\omega, \mathbf{k}) = \left(\delta^{ij} - \frac{k^i k^j}{k^2}\right)\rho^{ij} - \lambda\left(\rho^{00} - \frac{k^i k^j}{k^2}\rho^{ij}\right). \tag{6.6}$$

For $\lambda = 1$ one recovers the spectral function $\rho^\mu{}_\mu$. This diagonal channel, however, suffers from a UV divergence of order ω^2 for large ω. From the longitudinal part, it also

gets a contribution containing a diffusion pole. Both these obstacles are hard to deal with simultaneously which is why many authors choose to examine the purely transverse channel (corresponding to the case $\lambda = 0$) where there is no diffusion pole [46]. In this work, however, we set $\lambda = -2$ which amounts to the difference of the longitudinal and the transverse channel whereby one cancels the UV divergence for large frequencies but keeps the diffusion pole. For $\lambda = -2$, eqn. (6.6) becomes

$$\rho_{\lambda=-2} = \left(\delta^{ij} - \frac{3k^i k^j}{k^2}\right)\rho^{ij} + 2\rho^{00}. \tag{6.7}$$

With the definitions of $\mathbb{P}^{\mu\nu}_{\mathrm{L/T}}$ from Ref. [85],

$$\begin{aligned} \mathbb{P}^{\mu\nu}_{\mathrm{T}} &= \eta^{\mu}{}_{k}\,\eta^{\nu}{}_{l}\left(\eta_{kl} + \frac{\mathcal{K}_k\mathcal{K}_l}{k^2}\right) \\ \mathbb{P}^{\mu\nu}_{\mathrm{L}} &= \eta^{\mu\nu} - \frac{\mathcal{K}^\mu\mathcal{K}^\nu}{\mathcal{K}^2} - \mathbb{P}^{\mu\nu}_{\mathrm{T}}, \end{aligned} \tag{6.8}$$

where $\mathcal{K}_\mu = (k_0, k_1, k_2, k_3)^{\mathrm{T}}$ and $\eta_{\mu\nu} = (+---)$, one can decompose $\rho^{\mu\nu}$ into

$$\rho^{\mu\nu} = \mathbb{P}^{\mu\nu}_{\mathrm{T}}\rho_{\mathrm{T}} + \mathbb{P}^{\mu\nu}_{\mathrm{L}}\rho_{\mathrm{L}}. \tag{6.9}$$

It follows that

$$\begin{aligned} \rho^{ij} &= \mathbb{P}^{ij}_{\mathrm{T}}\rho_{\mathrm{T}} + \mathbb{P}^{ij}_{\mathrm{L}}\rho_{\mathrm{L}} \\ \rho^{00} &= \mathbb{P}^{00}_{\mathrm{T}}\rho_{\mathrm{T}} + \mathbb{P}^{00}_{\mathrm{L}}\rho_{\mathrm{L}}. \end{aligned} \tag{6.10}$$

One can show that [85]

$$\rho^{\mu}{}_{\mu} = 2\rho_{\mathrm{T}} + \rho_{\mathrm{L}}. \tag{6.11}$$

When one inserts eqns. (6.10) into eqn. (6.7), however, one ought to calculate

$$\begin{array}{cccc} \left(\delta^{ij} - \dfrac{3k^i k^j}{k^2}\right) & \mathbb{P}^{ij}_{\mathrm{L/T}} & \rho_{\mathrm{L/T}} & \text{and} \\ 2 & \mathbb{P}^{00}_{\mathrm{L/T}} & \rho_{\mathrm{L/T}}. & \end{array} \tag{6.12}$$

At first, we compute

$$\begin{aligned} & \left(\delta^{ij} - \frac{3k^i k^j}{k^2}\right)\mathbb{P}^{ij}_{\mathrm{T}}\,\rho_{\mathrm{T}} \\ = & \left(\delta^{ij} - \frac{3k^i k^j}{k^2}\right)\eta^{i}{}_{k}\,\eta^{j}{}_{l}\left(\eta_{kl} + \frac{\mathcal{K}_k\mathcal{K}_l}{k^2}\right)\rho_{\mathrm{T}} \\ = & \left(\delta^{ij} - \frac{3k^i k^j}{k^2}\right)\left(\eta_{ij} + \frac{\mathcal{K}_i\mathcal{K}_j}{k^2}\right)\rho_{\mathrm{T}} \\ = & \left(-3 + \frac{k^2}{k^2} + \frac{3k^2}{k^2} - \frac{3k^4}{k^4}\right)\rho_{\mathrm{T}} \\ = & -2\rho_{\mathrm{T}}. \end{aligned} \tag{6.13}$$

The second term is

$$\begin{aligned}
&\left(\delta^{ij} - \frac{3k^i k^j}{k^2}\right) \mathbb{P}_{\mathrm{L}}^{ij}\, \rho_{\mathrm{L}} \\
= &\left(\delta^{ij} - \frac{3k^i k^j}{k^2}\right) \left(\eta^{ij} - \frac{\mathcal{K}^i \mathcal{K}^j}{\mathcal{K}^2} - \mathbb{P}_{\mathrm{T}}^{ij}\right) \rho_{\mathrm{L}} \\
= &\left(-3 - \frac{k^2}{\mathcal{K}^2} + \frac{3k^2}{k^2} + \frac{3k^4}{k^2\mathcal{K}^2} - \mathbb{P}_{\mathrm{T}}^{ij}\right) \rho_{\mathrm{L}} \\
= &\left(2\,\frac{k^2}{\mathcal{K}^2} + 2\right) \rho_{\mathrm{L}}. \qquad (6.14)
\end{aligned}$$

The third term is

$$2\,\mathbb{P}_{\mathrm{T}}^{00}\, \rho_{\mathrm{T}} = 0. \qquad (6.15)$$

And the last term is computed to

$$\begin{aligned}
&2\,\mathbb{P}_{\mathrm{L}}^{00}\, \rho_{\mathrm{L}} \\
= &\; 2\left(\eta^{00} - \frac{\mathcal{K}^0 \mathcal{K}^0}{\mathcal{K}^2}\right) \rho_{\mathrm{L}} \\
= &\; 2\left(1 - \frac{k^0 k^0}{\mathcal{K}^2}\right) \rho_{\mathrm{L}}. \qquad (6.16)
\end{aligned}$$

Putting these four terms together, one gets

$$\begin{aligned}
\rho_{\lambda=-2} &= -2\rho_{\mathrm{T}} + 2\rho_{\mathrm{L}} + 2\left(1 + \frac{-k^0 k^0 + k^2}{\mathcal{K}^2}\right) \rho_{\mathrm{L}} \\
&= -2\rho_{\mathrm{T}} + 2\rho_{\mathrm{L}} + 2\underbrace{\left(\frac{\mathcal{K}^2 - k^0 k^0 + k^2}{\mathcal{K}^2}\right)}_{=0.} \rho_{\mathrm{L}} \\
&= 2\left(\rho_{\mathrm{L}} - \rho_{\mathrm{T}}\right). \qquad (6.17)
\end{aligned}$$

6.2.1 Perturbative treatment

In subsection 6.5.3, we want to constrain the lattice fit result by results obtained from a perturbative treatment. Therefore these results are briefly displayed here.

In Ref. [85], the author provides the leading order (LO) expressions for the transverse and longitudinal part of the spectral function. These read[1]

$$\begin{aligned}
\rho_{\mathrm{T}}^{\mathrm{LO}} &= -\frac{4N_c\,\mathcal{K}^2}{k^2}\left[\frac{k_0^2 + k^2}{2}\,\langle 1\rangle - 2\,\langle\, p\,(k_0 - p)\rangle\right] \\
\rho_{\mathrm{L}}^{\mathrm{LO}} &= +\frac{8N_c\,\mathcal{K}^2}{k^2}\left[\frac{k_0^2 - k^2}{2}\,\langle 1\rangle - 2\,\langle\, p\,(k_0 - p)\rangle\right], \qquad (6.18)
\end{aligned}$$

[1] The expressions given here and in Ref. [85] differ by a factor 2 because the spectral representation of the correlator, eqn. (6.1), includes a factor $1/2$ which is not present in the corresponding definition in Ref. [85].

where

$$\langle \dots \rangle \equiv \frac{1}{16\pi k} \left\{ \theta(k_-) \int_{k_-}^{k_+} \mathrm{d}p - 2\theta(-k_-) \int_{k_+}^{\infty} \mathrm{d}p \right\} \left[n_{\mathrm{F}}(p - k_0) - n_{\mathrm{F}}(p) \right] (\dots). \tag{6.19}$$

The values of $\langle 1 \rangle$ and $\langle\, p\,(k_0 - p) \rangle$ are given in Ref. [85]. In terms of the LO expressions (6.18), the spectral function $\rho^{\mu}{}_{\mu}$ reads

$$\rho^{\mathrm{LO},\mu}{}_{\mu} = 2\rho_{\mathrm{T}}^{\mathrm{LO}} + \rho_{\mathrm{L}}^{\mathrm{LO}} = -4N_c \mathcal{K}^2 \langle 1 \rangle \,. \tag{6.20}$$

Using the projection (6.17) we find

$$\rho_{\lambda=-2}^{\mathrm{LO}} = \frac{8N_c\mathcal{K}^2}{k^2} \left[\frac{3k_0^2 - k^2}{2} \langle 1 \rangle - 6 \langle\, p\,(k_0 - p) \rangle \right]. \tag{6.21}$$

6.3 Transport coefficients

The line of argumentation is based on the review by Xxxxx [46].

When a system in equilibrium is perturbed out of equilibrium by small amplitude perturbations, linear response theory teaches us that the response of an observable A in the system to the perturbation is determined by the correlator associated with A. In particular, the retarded correlator associated to A encodes the information about how the observable A relaxes back to its equilibrium value.

In order to describe the relaxation at late times, hydrodynamic predictions are applicable. Therefore, hydrodynamics provide a functional form of the retarded correlator at small frequencies ω. These analytic expressions establish the so-called Kubo formulae for transport coefficients.

Transport coefficients are the coefficients of a derivative expansion and encode the information about the real-time properties of the system at hand. Thus, relativistic hydrodynamics plays the role of a low-energy effective theory for the correlations of strongly interacting particles in a thermal medium and the 'low-energy constants' of this effective theory are the transport coefficients. As a simple example, one can look at the diffusion of a certain type of particle in a thermal bath which is described by the diffusion equation [46]

$$\partial_t n(\mathbf{x}) = D\nabla^2 n(\mathbf{x}) \tag{6.22}$$

with n being the particle number density and D the diffusion coefficient. Its solution reads [46]

$$\tilde{n}(\omega, \mathbf{k}) = \frac{n(0, \mathbf{k})}{-i\omega + D\mathbf{k}^2}, \tag{6.23}$$

where $\tilde{n}$ is the Fourier transform of $\theta(t) \cdot n$,

$$\tilde{n}(\omega, \mathbf{k}) = \int_0^\infty \mathrm{d}t\, e^{i\omega t} \int \mathrm{d}\mathbf{x}\, e^{-i\mathbf{k}\cdot\mathbf{x}}\, n(t, \mathbf{x}). \tag{6.24}$$

Here, $\theta(t)$ denotes the Heaviside step function. The initial condition $n(0, \mathbf{k})$ is given by the associated static susceptibility [46]. The solution (6.23) exhibits a pole in the complex ω plane at $\omega_{\mathrm{pole}}(\mathbf{k}^2) = -iD\mathbf{k}^2$ which indicates the relaxation rate of the perturbed particle density. The imaginary part of the density-density correlator in Fourier space provides the spectral function [46],

$$\frac{\rho^{nn}(\omega, \mathbf{k})}{\omega} = \frac{\chi_s(\mathbf{k})}{\pi} \frac{D\mathbf{k}^2}{\omega^2 + (D\mathbf{k}^2)^2}, \tag{6.25}$$

where χ_s is the static susceptibility, see also eqn. (1.36). From eqn. (6.25) one can infer how the low-frequency and low-momentum part of the spectral function contains information about transport coefficients and other real-time quantities. The longitudinal part of the current correlator is related to the density-density correlator, $\rho_{\mathrm{SL}}(\omega, \mathbf{k}) = \frac{\omega^2}{\mathbf{k}^2}\rho^{nn}(\omega, \mathbf{k})$, which results in the Kubo formula

$$D\chi_s^N = \pi \lim_{\omega\to 0} \lim_{\mathbf{k}\to 0} \frac{\rho_{\mathrm{SL}}(\omega, \mathbf{k})}{\omega} \tag{6.26}$$

with the particle number susceptibility $\chi_s^N = \beta \int \mathrm{d}\mathbf{x}\, n(t, \mathbf{x})\, n(0)$. Eqn. (6.26) shows that the diffusion coefficient D is defined in the limit $(\omega, \mathbf{k}) \to 0$. After a slow and adiabatic perturbation in particle density, the particle density (6.23) will relax back to equilibrium [45]. The dispersion relation of this relaxation process is given by the pole of the response function, i.e. $\omega = -iD\mathbf{k}^2$. Furthermore, the function $\rho_{\mathrm{SL}}(\omega, \mathbf{k})/\omega$ is expected to be smooth [45] which can be used to define an effective diffusion coefficient evaluated at $(\omega, \mathbf{k}) \neq 0$ as is done below, see eqn. (6.27).

Transport properties, like the viscosity, diffusivity or electric conductivity, describe the dynamics of weak and adiabatically changing fluctuations in a medium [76] as well as the medium's response induced by slowly varying inhomogeneities or external forces. When considering weakly coupled quantum field theories, it should be possible to calculate the transport coefficients from the theory itself. In Ref. [76], the authors show how transport coefficients are computed in an effective kinetic theory by solving a linear integral equation.

When a medium is weakly coupled, excitations with momenta $p \gg gT$ are long-lived and well-defined quasiparticles and their typical momenta can be called "hard" [76]. Furthermore, the conserved charges of the system are usually carried by these excitations.

In Ref. [86], the author shows that it is possible to compute transport coefficients diagrammatically in a weakly-coupled relativistic scalar field theory when the starting point are Kubo formulae involving current-current or stress-stress correlators.

From Ref. [87] we learn that it is important for lattice computations to be able to discriminate between the weak-coupling and the strong-coupling scenarios for the QGP. When the plasma is weakly coupled, the two time scales of the inverse temperature $\sim 1/T$ and the typical relaxation time $\sim 1/(g^4\,T)$ are clearly distinct [87]. Therefore, kinetic theory is apt to study the real time properties of the plasma. For the strongly coupled case, however, in the AdS/CFT picture, one cannot distinguish between those time scales and a quasi-particle picture is not applicable [87]. The constituents of the medium behave as a single collective system or resonance. Furthermore, one does not see a transport peak in the spectral densities of such strongly coupled theories [87].

The relevant channels appearing in the correlation functions of the energy-momentum tensor can be determined similarly to those of the vector current. With momentum $\mathbf{k}$ along the z axis, the complete set of response functions reads (G_R is the retarded correlator) [87]

- $G_R^{zxzx}(\omega, k)$, Shear mode
- $G_R^{xyxy}(\omega, k)$, Tensor mode
- $G_R^{zzzz}(\omega, k)$, Sound mode
- $\eta_{\mu\nu}\,\eta_{\alpha\beta}\,G_R^{\mu\nu\alpha\beta}(\omega, k)$, Bulk mode.

The following two sections 6.4 and 6.5 are dedicated to proposing two alternate approaches for reconstructing spectral functions from Euclidean data. Via the Kubo formula (6.26), the diffusion coefficient can be determined. And following the definition in Ref. [84], we are going to compute an *effective* diffusion coefficient

$$D_{\text{eff}}(k) = \frac{\rho_{\lambda=-2}(\omega = k, \boldsymbol{k})}{4\chi_s k}, \tag{6.27}$$

where the estimated and reconstructed spectral function is evaluated on the light cone, $\omega = k$.

6.4 Backus-Gilbert method

One way of dealing with a numerically ill-posed inversion problem, as given by eqn. (6.1), is the Backus-Gilbert method, introduced in Ref. [88] and first applied within lattice QCD in Refs. [66, 89, 81].

With a given integral representation of the Euclidean correlator, $G_{\mathrm{E}}(\tau)$, in terms of a spectral function, $\rho(\omega)$, in frequency space and an integration kernel, $K(\omega,\tau)$,

$$G_{\mathrm{E}}(\tau) = \int_0^\infty \frac{\mathrm{d}\omega}{2\pi} \underbrace{\frac{\cosh(\omega(\beta/2-\tau))}{\sinh(\beta\omega/2)}}_{K(\omega,\tau)} \rho(\omega), \tag{6.28}$$

the goal of the inversion problem consists in finding a set of coefficients $q_i(\bar{\omega})$ in order to construct an estimator ρ_{BG} such that

$$\rho_{\mathrm{BG}}(\bar{\omega}) = \int_0^\infty \frac{\mathrm{d}\omega}{2\pi}\, \hat{\delta}(\bar{\omega},\omega)\rho(\omega), \quad \hat{\delta}(\bar{\omega},\omega) = \sum_{i=1}^{N_f} q_i(\bar{\omega}) K(\omega,\tau_i). \tag{6.29}$$

The estimator ρ_{BG} should have maximal overlap with the true spectral function at a given frequency, $\bar{\omega}$. The resolution function, $\hat{\delta}(\bar{\omega},\omega)$ is constructed with respect to the given kernel and normalized to

$$\int_0^\infty \mathrm{d}\omega\, \hat{\delta}(\bar{\omega},\omega) = 1. \tag{6.30}$$

When the coefficients $q_i(\bar{\omega})$ are known, it is easy to construct the estimator via

$$\rho_{\mathrm{BG}}(\bar{\omega}) = \sum_{i=1}^{N_\tau} q_i(\bar{\omega}) G_{\mathrm{E}}(\tau_i), \qquad \mathrm{Var}\left[\rho_{\mathrm{BG}}\right] = \sum_{i,j=1}^{N_\tau} q_i(\bar{\omega}) \mathcal{C}_{ij} q_j(\bar{\omega}), \tag{6.31}$$

where the variance of the estimator is given according to the statistical interpretation of the covariance matrix of the original Euclidean data, $\mathcal{C}_{ij}$.

The Backus-Gilbert method faces two challenges of the inversion problems:

- maximize the stability of estimator ρ_{BG}
- maximize the agreement of estimator ρ_{BG} and "true" solution ρ subject to the normalization constraint (6.30).

In order to maximize the stability of the estimator one will minimize the variance, $\mathrm{Var}\left[\rho_{\mathrm{BG}}\right]$. The maximization of agreement between estimator and true spectral function is obtained by minimizing the second moment of the resolution function. Imposing the normalization constraint this amounts to minimizing the functional (for the remainder of this section, the summation convention is used for better readability)

$$\begin{aligned} F\left[q_i(\bar{\omega})\right] &= \int \mathrm{d}\omega\, (\omega-\bar{\omega})^2 \left[\hat{\delta}(\bar{\omega},\omega)\right]^2 - \lambda_1 \left(\int \mathrm{d}\omega\, \hat{\delta}(\bar{\omega},\omega) - 1 \right) \\ &= q_i(\bar{\omega}) \cdot \int \mathrm{d}\omega\, K(\omega,\tau_i)\, (\omega-\bar{\omega})^2\, K(\omega,\tau_j) \cdot q_j(\bar{\omega}) \\ &\quad -\lambda_1 \left(q_i(\bar{\omega}) \int \mathrm{d}\omega\, K(\omega,\tau_i) - 1 \right) \\ &\equiv q_i(\bar{\omega})\, \mathcal{W}_{ij}(\bar{\omega})\, q_j(\bar{\omega}) - \lambda_1 \left(q_i(\bar{\omega})\, R_i - 1 \right), \end{aligned} \tag{6.32}$$

where

$$\begin{aligned} \mathcal{W}_{ij} &= \int \mathrm{d}\omega\, K(\omega,\tau_i)\,(\omega-\bar{\omega})^2\,K(\omega,\tau_j), \\ R_i &= \int \mathrm{d}\omega\, K(\omega,\tau_i). \end{aligned} \tag{6.33}$$

In total, one minimizes

$$\alpha\cdot F[\boldsymbol{q}(\bar{\omega})] + (1-\alpha)\cdot \mathrm{Var}\left[\rho_{\mathrm{BG}}\right], \qquad \alpha\in(0,1) \tag{6.34}$$

and obtains the set of coefficients

$$\boldsymbol{q}(\bar{\omega}) = \frac{\left[\alpha\cdot\mathcal{W}(\bar{\omega})+(1-\alpha)\cdot\mathcal{C}\right]^{-1}\cdot\boldsymbol{R}}{\boldsymbol{R}\cdot\left[\alpha\cdot\mathcal{W}(\bar{\omega})+(1-\alpha)\cdot\mathcal{C}\right]^{-1}\cdot\boldsymbol{R}}, \tag{6.35}$$

Thus, one knows all the components of

$$\rho_{\mathrm{BG}}(\bar{\omega}) = q_i(\bar{\omega})G_{\mathrm{E}}(\tau_i) \tag{6.36}$$

in terms of the original data and the given kernel.

In the course of performing the Backus-Gilbert reconstruction for the spectral function $\rho_\lambda(\omega,\mathbf{k})$, eqn. (6.6), one finds that for small frequencies $2\pi \gg \bar{\omega}/T > 0$ the resolution function (6.29) picks up spectral weight from the origin. One can prevent this from happening by imposing a second constraint in the form of a node for the resolution function at the origin,

$$0 \stackrel{!}{=} \hat{\delta}(\bar{\omega},0) = q_i(\bar{\omega})\,K(0,\tau_i). \tag{6.37}$$

Then the functional (6.32) becomes

$$\begin{aligned} F\left[q_i(\bar{\omega})\right] = q_i(\bar{\omega})\,\mathcal{W}_{ij}(\bar{\omega})\,q_j(\bar{\omega}) &- \lambda_1\left(q_i(\bar{\omega})\,R_i - 1\right) \\ &- \lambda_2\left(q_i(\bar{\omega})\,K_i\right) \end{aligned} \tag{6.38}$$

with $K_i = K(0,\tau_i)$. The coefficients are calculated to

$$\boldsymbol{q}(\bar{\omega}) = \left[\alpha\cdot\mathcal{W}(\bar{\omega})+(1-\alpha)\cdot\mathcal{C}\right]^{-1}\cdot\left[\frac{\mathfrak{B}}{\mathfrak{B}\mathfrak{C}-\mathfrak{A}^2}\cdot\boldsymbol{R} - \frac{\mathfrak{A}}{\mathfrak{B}\mathfrak{C}-\mathfrak{A}^2}\cdot\boldsymbol{K}\right], \tag{6.39}$$

where

$$\begin{aligned} \mathfrak{A} &= \boldsymbol{K}\cdot\left[\alpha\cdot\mathcal{W}(\bar{\omega})+(1-\alpha)\cdot\mathcal{C}\right]^{-1}\cdot\boldsymbol{R} \\ \mathfrak{B} &= \boldsymbol{K}\cdot\left[\alpha\cdot\mathcal{W}(\bar{\omega})+(1-\alpha)\cdot\mathcal{C}\right]^{-1}\cdot\boldsymbol{K} \\ \mathfrak{C} &= \boldsymbol{R}\cdot\left[\alpha\cdot\mathcal{W}(\bar{\omega})+(1-\alpha)\cdot\mathcal{C}\right]^{-1}\cdot\boldsymbol{R}. \end{aligned} \tag{6.40}$$

variation	values
$\tau_{\min}/\beta$	$\{0.1, \ldots, 0.25\}$
with $\hat{\delta}(\bar{\omega}, 0) = 0$	{yes, no}
BG regularization parameter α	$\{10^{-2}, \cdots, 10^{-4}\}$
tree-level improved	{yes, no}

Table 6.1: Variations of the BG method used to estimate a systematic uncertainty, taken from [90].

The Backus-Gilbert method does not provide a systematic error, hence we performed many variations giving rise to a systematic uncertainty estimate. Table 6.1 shows all variations that entered the BG analysis. One usually omits several of the lowest time separations of the Euclidean correlator in any analysis because of cut-off effects and lattice artifacts near the source. So we varied the lowest time separation, $\tau_{\min}/\beta$ for which to start the BG method. Whether or not one imposes the additional constraint (6.37), also enters the systematic uncertainty. The BG regularization parameter α in eqn. (6.34) is a free parameter and therefore varied. And finally, we also perform the variation over tree-level improvement or not for the continuum correlator. As clarified in Ref. [90], the final estimate for the *effective* diffusion constant, eqn. (6.27), is quoted as the median of this distribution under all variations. The 68% interval serves as overall systematic uncertainty. The statistical error is small compared to the systematic one at the lower momenta $k < 1\,\mathrm{GeV}$.

6.5 Ansatz for the spectral function

This section is heavily based on my previous work in Ref. [90] and contains passages from there that I kept for scientific clarity. The contribution of XXXXX X. XXXX and of XXXXX XXXXX was to provide data for the continuum limit as discussed in 4.3. The contribution of Xxx Xxxxxx was to measure the correlators and to perform the continuum limit, also discussed in 4.3, and to perform the analysis using the Backus-Gilbert method as displayed in the previous section. The contribution of Xxxxxx Xxxxx was the supervision and conceptualization of the entire project.

In the previous section 6.4, a model-independent, linear method for estimating a spectral function from Euclidean data is discussed that heavily relies on the circumstance that the spectral function one wants to reconstruct, is actually slowly varying and

smooth. In this section, however, we want to introduce a rational function ansatz in form of a Padé approximant that also allows for poles in the spectral function and incorporates information from perturbation theory as well as relativistic hydrodynamics and from physics constraints. Before discussing the ansatz, it is useful to derive a sum rule for the spectral function $\rho_{\lambda=-2}(\omega, \boldsymbol{k})$.

6.5.1 Sum rule

In the vacuum theory, Lorentz invariance and transversity of $G_{\mu\nu}(\tau, \boldsymbol{k})$ lead to

$$\rho_{\lambda=-2}(\omega, \boldsymbol{k}) = \left(\delta^{ij} - \frac{3k^i k^j}{k^2}\right) \rho_{ij}(\omega, \boldsymbol{k}) + 2\rho_{00}(\omega, \boldsymbol{k}) = 0. \tag{6.41}$$

At finite temperature $T > 0$ no new divergences arise and the combination stays UV finite. Therefore we can employ an operator product expansion (OPE) for the spectral function: by power counting, $\rho_{\lambda=-2}(\omega, \boldsymbol{k}) \sim \frac{\langle \mathcal{O}_4 \rangle}{\omega^2} + \cdots$ as $\omega \to \infty$, where $\mathcal{O}_4$ is a dimension-four operator. Moreover, $\rho_{\lambda=-2}(\omega, \boldsymbol{k} = \boldsymbol{0}) = 0$ at $\omega > 0$ because of charge conservation and so we expect from the OPE

$$\rho_{\lambda=-2}(\omega, \boldsymbol{k}) \propto \frac{k^2 \langle \mathcal{O}_4 \rangle}{\omega^4}, \qquad \omega \gg \pi T, k. \tag{6.42}$$

In frequency-momentum space, the spectral representation of the Euclidean correlator can be expanded about $\omega_n = \infty$,

$$\begin{aligned} \tilde{G}(\omega_n, \boldsymbol{k}) \quad &= \quad \int_0^\infty \frac{\mathrm{d}\omega}{\pi}\, \omega\, \frac{\rho_{\lambda=-2}(\omega, \boldsymbol{k})}{\omega^2 + \omega_n^2} \\ &\overset{\omega_n \to \infty}{\longrightarrow} \quad \frac{1}{\pi\, \omega_n^2} \int_0^\infty \mathrm{d}\omega\, \omega\, \rho_{\lambda=-2}(\omega, \boldsymbol{k}) + \mathcal{O}(\omega_n^{-4}). \end{aligned} \tag{6.43}$$

From the OPE, however, one determines the first non-vanishing contribution to be of $\mathcal{O}(\omega_n^{-4})$, see Eq. (6.42). Thus, the first coefficient in Eq. (6.43) is required to vanish exactly, and we deduce the superconvergent sum rule

$$\int_0^\infty \mathrm{d}\omega\, \omega\, \rho_{\lambda=-2}(\omega, \boldsymbol{k}) = 0. \tag{6.44}$$

6.5.2 Padé ansatz

The tanh-regulated spectral function can be modelled by a rational function as a combination of two Padé approximants,

$$\frac{\rho^{\mathrm{ans}}(\omega, k)}{\tanh(\omega\beta/2)} = \underbrace{\frac{A}{[\omega^2 + a^2]}}_{\text{part I}} \cdot \underbrace{\frac{(1 + B\omega^2)}{[(\omega + \omega_0)^2 + b^2]\,[(\omega - \omega_0)^2 + b^2]}}_{\text{part II}} \tag{6.45}$$

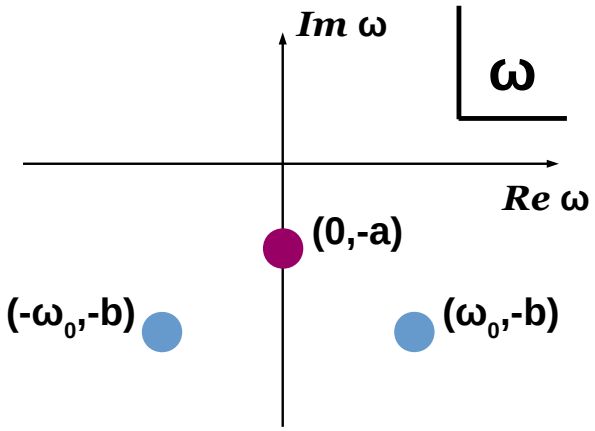

Figure 6.1: Complex ω-plane with the poles of the retarded correlator. There is the diffusion pole on the imaginary axis (red) and a pair of generic poles in the lower half-plane (blue) which model the pole structure of the AdS/CFT current correlator.

with two linear parameters A and B as well as three nonlinear parameters a, ω_0, and b. Part I models the diffusion pole as it arises in the hydrodynamics prediction for the infrared limit; when one identifies $a \leftrightarrow Dk^2$ for small k, part I resembles the known expression [77]

$$\frac{\rho(\omega,k)}{\omega} \approx \frac{4\chi_s D k^2}{\omega^2 + (Dk^2)^2}, \qquad \omega, k \ll D^{-1}. \tag{6.46}$$

Part II is inspired by the pole structure of the AdS/CFT current correlator, see Ref. [91] for details. When one wants to satisfy the superconvergent sum rule (6.44), it is necessary to introduce the second linearly independent parameter B in part II of Eq. (6.45). After imposing Eq. (6.44), however, the second linear parameter B becomes a function of (a, ω_0, b). Not only do the two poles at $(\pm\omega_0, -b)$ model the quasinormal modes of the retarded correlator as discussed in Ref. [91], they also match the $1/\omega^4$ behavior at large ω which is dictated by the operator product expansion (6.42), see also figure 6.1.

The remainder of this section deals with the straightforward uncorrelated and correlated fits and a physical exclusion criterion which was already discussed in Ref. [90]. For the sake of clarity, I stick to the exact words of this reference.

In the fit ansatz (6.45), we are left with four independent fit parameters after determining B for given (a, ω_0, b) via the sum rule (6.44). Then there are three degrees of freedom when we use seven data points between $\tau_{\min}/\beta = 0.25$ and $\tau_{\max}/\beta = 0.5$ on the continuum-extrapolated correlators. There is a huge subspace in the parameter

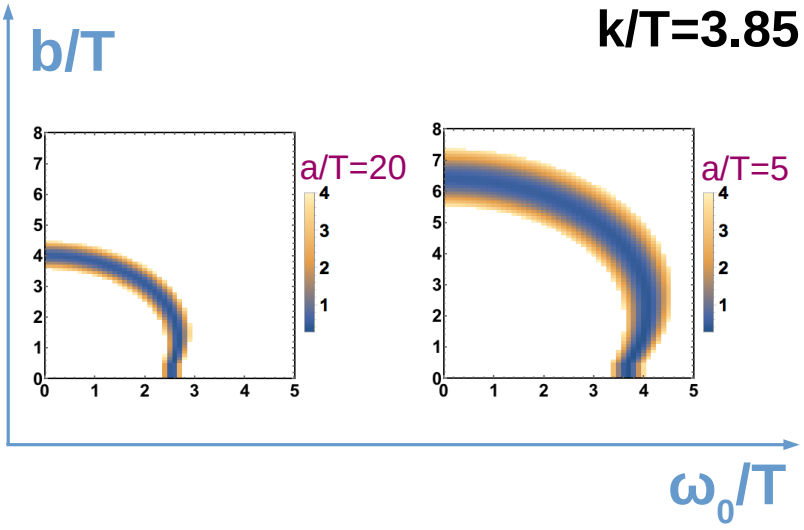

Figure 6.2: Uncorrelated χ^2-landscape in the (ω_0, b)-plane at photon momentum $k/T \approx 3.85$ for fixed values of a. The valley of $\chi^2 < 4$ is shown whereas the area with $\chi^2 > 4$ is marked in white, only solutions with uncorrelated $\chi^2 < 1$ are accepted. When the diffusion pole is fixed to be far from the origin, $a/T = 20$ (left panel), the generic pole at (ω_0, b) can move close to the real axis. In case the diffusion pole dominates the shape of the spectral function, $a/T = 5$ (right panel), the second pole is pushed into the complex plane.

space (A, a, ω_0, b) for which the uncorrelated χ^2 is smaller than one. χ^2 stands for χ^2 divided by the degrees of freedom throughout this work. Fig. 6.2 depicts the χ^2-valley in the (ω_0, b)-plane at photon momentum $k/T \approx 3.85$ where $\chi^2 < 1$ at two fixed values of a.

Because there is no local minimum in the uncorrelated χ^2-landscape, this results in a plethora of acceptable solutions. In other words, there are many shapes of the spectral function, none of which can be strongly ruled out by our data as they all satisfy $\chi^2(A, a, \omega_0, b) < 1$. So rather than minimizing the correlated χ^2, we try and find bounds to the effective diffusion constant by taking the *min* and *max* values of all photon rates with $\chi^2(A, a, \omega_0, b) < 1$.

We exclude all solutions that result in a negative photon rate from this procedure. This is due to the known positivity of the spectral function below the light cone,

$$\rho(\omega) \geq 0, \qquad \omega \leq k. \tag{6.47}$$

When one allows the second pole at (ω_0, b) to get too close to the real axis, the result is a very pronounced peak in the spectral function. This can happen when the nonlinear parameter a becomes large and the diffusion peak does not dominate the analyticity of the retarded correlator. For illustration see fig. 6.2: at $a/T = 20$ (left panel) the diffusion pole is far from the origin and the second pole at (ω_0, b) can approach the real axis. In fig. 6.4, the result is seen as a sharp peak below the light cone (dashed blue curve). For $a/T = 5$ (right panel of fig. 6.2), however, the second pole at (ω_0, b) is pushed into the complex plane and does not dominate the shape of the spectral function.

Such an additional peak from a pole close to the real axis corresponds to a very long-lived excitation in the medium which is unphysical if it survives longer than the largest possible relaxation times in the system. So we constrain the imaginary parts of both poles, i.e. the fit parameters a and b, to fulfil the exclusion criterion [77, 76]

$$\min(a, b) > \min(D_{\mathrm{AdS/CFT}} \cdot k^2, D_{\mathrm{PT}}^{-1}), \tag{6.48}$$

where $D_{\mathrm{AdS/CFT}} \cdot k^2$ describes the diffusion of an electric charge with $D_{\mathrm{AdS/CFT}} = 1/(2\pi T)$ and D_{PT}^{-1} accounts for the damping of a static current with $D_{\mathrm{PT}}^{-1} = \mathcal{O}(\alpha_s^2) \cdot T$, $\alpha_s = 0.25$. We claim that the exclusion criterion (6.48) amounts to a conservative constraint based on physics considerations. One assumes that for small frequencies, the photon production rate - and the corresponding diffusion coefficient - is actually largest in the most weakly coupled theory [77]. At these frequencies, the wavelength of the photon becomes larger than the mean free path in the medium and so the charges are diffusing. When the system is weakly coupled, charges can diffuse faster and so the current on the long photon wavelength scales is higher and the photon production, too.

6.5.3 Dealing with correlations and including constraints from perturbation theory

It is widely known that a naive spectral function fit to Euclidean data can result in spectral functions with arbitrary features and shapes. Therefore it is important to perform correlated fits and to take into account information from perturbation theory (PT) to reduce the outcome of the fit to those spectral functions that comply with PT.

Taking into account correlations

In the course of fitting an ansatz for the spectral function to the Euclidean data one encounters several obstacles. One problem we saw was the fact that an uncorrelated fit results in a χ^2-landscape that does not exhibit a unique global or local minimum. On the other hand, taking into account correlations between lattice sites has the result that for some momenta no solutions can be found that satisfy the exclusion criteria. As was argued in Ref. [92], performing a fully correlated fit improves the resolution in the low-frequency region that we are interested in. Additionally, including the covariance may yield a stronger exclusion and likelihood criterion than a naive uncorrelated fit. There is the possibility, however, that one over-interprets the correlations by considering the covariance matrix without a grain of salt and therefore no solutions are found. In order to make up for this we introduced a regularization factor $x \in (0, 1)$ such that

$$\mathcal{C} \to x \cdot \mathcal{C} + (1 - x) \cdot \mathrm{diag}(\mathcal{C}). \tag{6.49}$$

The case $x = 1$ corresponds to a fully correlated fit while with $x = 0$, one neglects all correlations in an uncorrelated fit. One needs to vary x between 0 and 1 such that one finds the largest possible value of x that yields substantial weight to the correlations and drives the χ^2 but does not rule out every possible solution as unacceptable due to its too large χ^2. We find the optimal value to be $x = 0.8$. Fig. 6.3 depicts the correlated χ^2-landscape in the (ω, b)-plane for photon momentum $k/T \approx 3.85$. The valley of acceptable χ^2 is substantially reduced compared to the uncorrelated case, fig. 6.2. Still, there is no global minimum in the interior of the parameters' domain of definition. Hence, we will quote the *min* and *max* values of the resulting photon rate. This distribution will be much smaller, though.

Applying perturbative constraints

In Ref. [85], the thermal dilepton rate is determined to NLO in a perturbative treatment at non-zero momentum. The same vector current correlators enter the calculation of both the dilepton rate and the photon rate. Hence, we can use these results to further constrain our determination of the photon production rate. One expects that the shape and the features of the spectral function at small frequencies $\omega < \pi T$ is reliably inferred from a perturbative approach. Therefore we want to rule out all such solutions to our fit ansatz (6.45) for which the curvature of the correlator at the origin $\omega = 0$ does not match the corresponding perturbative value obtained from Ref. [85] within a 30%-interval. More concisely: After scanning through the parameter space of the fit ansatz

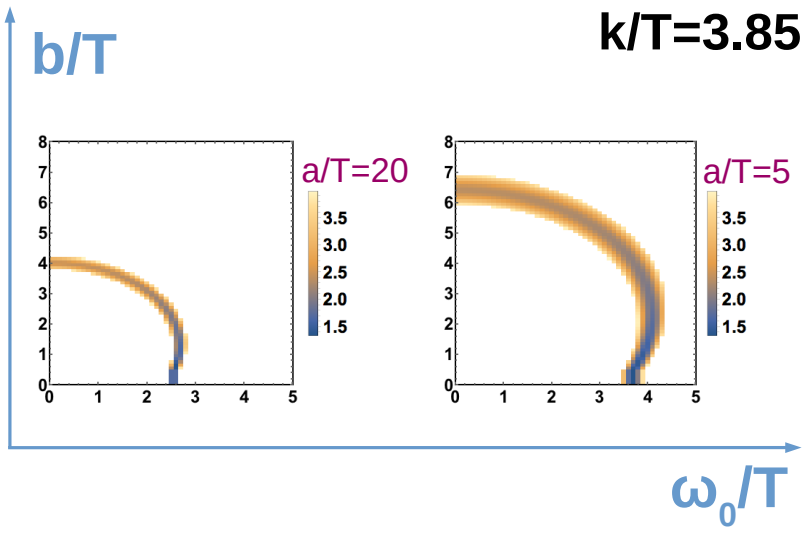

Figure 6.3: Correlated χ^2-landscape with $x = 0.8$ in the (ω_0, b)-plane at photon momentum $k/T \approx 3.85$ for fixed values of a. The valley of $\chi^2 < 4$ is shown whereas the area with $\chi^2 > 4$ is marked in white, only solutions with correlated $\chi^2 < 2$ are accepted. When the diffusion pole is fixed to be far from the origin, $a/T = 20$ (left panel), the generic pole at (ω_0, b) can move close to the real axis. In case the diffusion pole dominates the shape of the spectral function, $a/T = 5$ (right panel), the second pole is pushed into the complex plane.

(6.45) using the regularized covariance matrix (6.49) and applying the exclusion criterion (6.48) one requires

$$\left| \frac{\int_0^\infty \mathrm{d}\omega\, \omega^2 \rho^{\mathrm{ans}}(\omega, k)\, \frac{\cosh\left(\omega\left(\frac{\beta}{2}-\tau\right)\right)}{\sinh(\omega\beta/2)}}{\int_0^\infty \mathrm{d}\omega\, \omega^2 \rho^{\mathrm{LO}}_{\lambda=-2}(\omega, k)\, \frac{\cosh\left(\omega\left(\frac{\beta}{2}-\tau\right)\right)}{\sinh(\omega\beta/2)}} - 1 \right| < 0.3, \tag{6.50}$$

where ρ^{ans} is given by eqn. (6.45) and $\rho^{\mathrm{LO}}_{\lambda=-2}$ is given by eqn. (6.21). Unfortunately, this procedure has no sizeable impact on the distribution of allowed solutions.

In fig. 6.4 one can see example spectral functions for $k/T = \sqrt{8} \cdot \pi/2 \approx 4.44$ (vertical black line) as functions of the frequency, ω/T. Shown are the spectral functions that yield the median (solid green), the minimal (dashed blue) and the maximal (dotted purple) values of the photon rate distribution. The median spectral function, e.g., exhibits an unphysical bump in the timelike region, $\omega > k$. The other two spectral functions have rather pronounced peaks and features, too. Nonetheless, they all agree

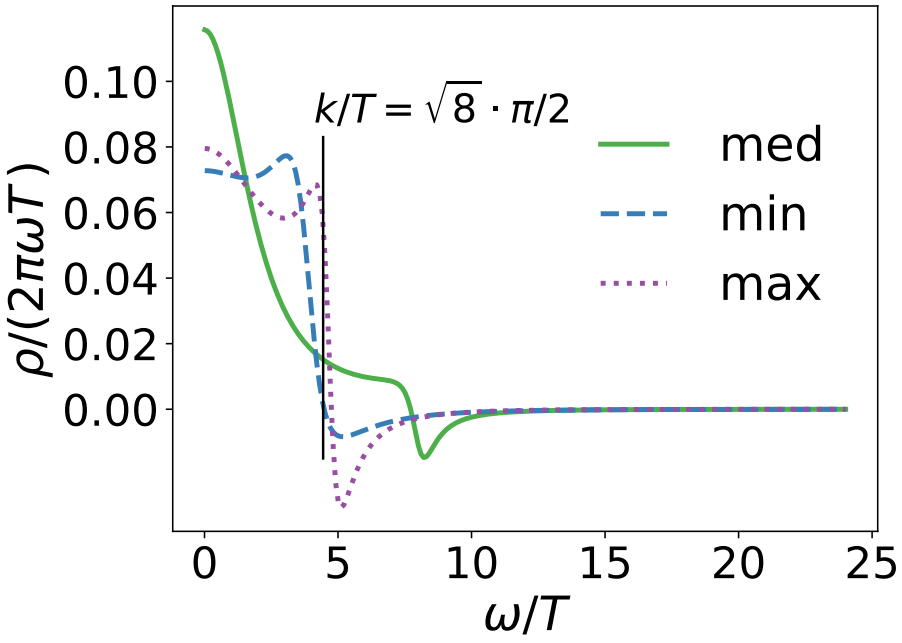

Figure 6.4: Example spectral functions for $k/T \approx 4.44$ (vertical black line) corresponding to the median, minimal and maximal values of the photon rate distribution. The spectral functions result from a correlated fit with $x = 0.8$.

with the data and therefore cannot be ruled out. As such, they represent typcial solutions of the inverse problem (6.1).

6.6 Results for the effective diffusion coefficient

After having discussed two independent approaches for estimating the spectral function from Euclidean data in sections 6.4 and 6.5, we can now display the results for the effective diffusion coefficient, eqn. (6.27) from both methods and compare them. Figure 6.5 shows the results both from the BG method and the spread from the distribution of solutions to the correlated fit at $T = 250\,\mathrm{MeV}$. As discussed in section 6.4, performing the BG method while implementing or not implementing the constraint on the resolution function yields a large spread at lower momenta. At higher momenta the two variations become compatible and the systematic and statistical error shrinks considerably. The red bars indicate the bounds we find from quoting the minimal and maximal value of the distribution of the effective diffusion constant that have correlated $\chi^2 < 2$ with a regularization parameter of $x = 0.8$ and the median of this distribution. Ruling out all such solutions of this distribution that deviate from the perturbative scenario by

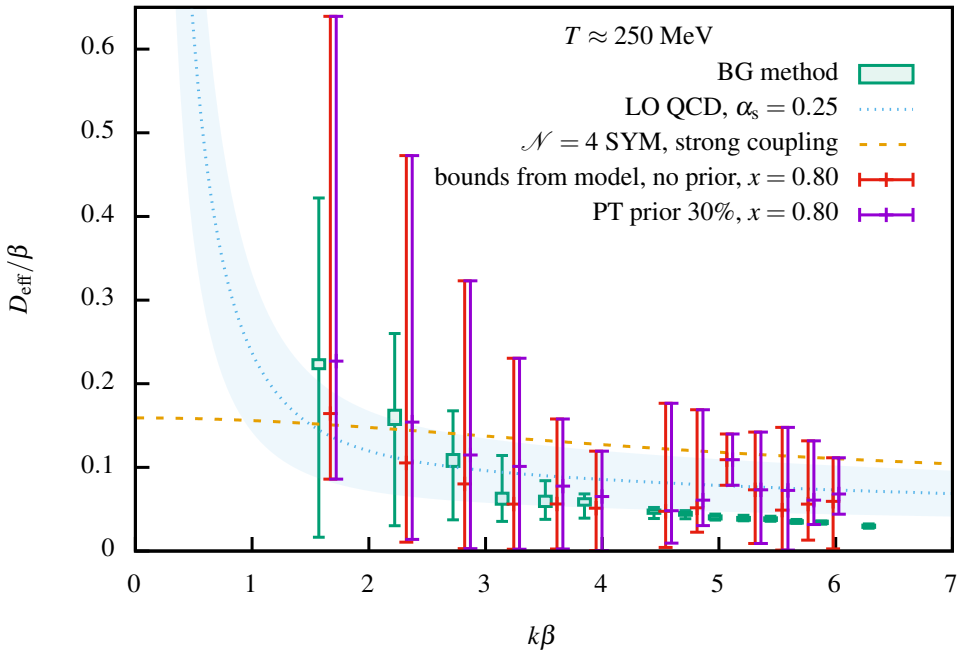

Figure 6.5: Estimate of the effective diffusion constant at $T \approx 250\,\mathrm{MeV}$. The results from the BG method are plotted as green dots. Their error bars represent the systematic uncertainty obtained through the 68% interval of the distribution of all results under the BG variations described in section 6.4. The bounds from the correlated model fit with a regularization factor $x = 0.8$ and the median of the distribution of all results compatible with the fit ansatz are displayed as red bars. After applying the perturbative constraint one obtains the purple bars. Additionally, the strong-coupling result from $\mathcal{N} = 4$ SYM and a weak-coupling result from leading-order (LO) perturbative QCD with $\alpha_s = 0.25$ are shown.

more than 30%, results in a distribution indicated by the purple bars and the respective median. Since the purple and red bars coincide with each other at nearly all momenta, one can conclude that the curvature at the origin of the results found before applying the perturbative constraint already agree with the perturbative curvature at the origin within 30%. Nonetheless, it is still of great interest to see what one might infer from higher-order perturbative calculations that have come up recently [93]. Furthermore, the strong-coupling result from $\mathcal{N} = 4$ supersymmetric Yang-Mills theory (SYM) and a weak-coupling result from leading-order (LO) perturbative QCD with $\alpha_s = 0.25$ are plotted as comparison.

Apart from two exceptions around photon momentum $k\beta \approx 5.0$ and $k\beta \approx 5.2$, the

median of the correlated fit distribution and the BG estimator are remarkably close and agree within the systematic and statistical error of the BG estimator. For the whole momentum range, the bounds of the effective diffusion constant from examining the minimum and maximum values of the maximum likelihood estimator consistent with the data, cover a big interval and it is not possible to discriminate between the weak-coupling and the strong-coupling scenarios. Applying the prior from perturbation theory does not have a big impact on the spread of the effective diffusion coefficient. At photon momenta $1.0\,\mathrm{GeV} \leq k \leq 1.4\,\mathrm{GeV}$ which are relevant for heavy-ion phenomenology, however, our study excludes photon rates larger than twice the weak-coupling prediction. Thus, the results of hydrodynamical predictions that use the leading-order photon emission rate as an ingredient, are confirmed by our study.

In a recent analysis [64], further progress was made and important studies were conducted. As mentioned above in section 4.1, Xxxxx Xx studied autocorrelation times of gluonic observables for the X7 ensemble and found strong autocorrelation. This was dealt with by dropping the first two hundred configurations out of a total of $N_{\mathrm{conf}} \sim 700$ configurations that had become available at the time of the analysis presented in [64]. For the analysis of this work, there were only $N_{\mathrm{conf}} \sim 100$ configurations available. Additionally, Xxxxx Xx even produced another very fine ensemble labeled W7 at $T = 254\,\mathrm{MeV}$ with $V/a^4 = N_\tau \times N_\sigma^3 = 20 \times 80^3$ such that the continuum limit extrapolation was constructed from (O7, W7, X7) rather than (F7, O7, X7). The result was that the quality of the continuum limit could be substantially improved.

The validity range of the Padé ansatz (6.45) with respect to the two different scenarios of weakly interacting quarks in the perturbative regime and of strongly coupled quarks in the regime of $\mathcal{N} = 4$ SYM theory with infinite coupling is tested using mock data [64]. The spectral functions in both scenarios are known and the Padé ansatz reproduces the known solutions of the effective diffusion coefficient in both scenarios with a p-value above 0.32 such that is is not ruled out by likelihood criteria. In order to keep the mock data study realistic, the covariance matrices of the lattice QCD data are re-used after rescaling in a way to keep the relative error on the correlator the same.

Furthermore, the effect of correlations between data obtained at neighboring momenta can be studied. This study was performed by Xxxxxx Xxxxxx [64, 94]. The importance of estimating the effect of correlations among the input data relevant for the inverse problem has been addressed previously [92]. One can express the three non-linear parameters a, b, ω_0 of the ansatz (6.45) as functions of the momentum k, both linear and quadratic in k. The covariance matrix is constructed in a fashion similar to

(6.49). The recent study presents the dependence on whether one chooses a linear or a quadratic ansatz. It resolves the distribution of solutions with acceptable χ^2 with respect to their corresponding χ^2 values and states the p-values. For the highest momenta $k\beta \geq\sim 4.5$, both the weakly-interacting and strongly-coupled theories cannot be ruled out, similar to the result found in this work, see fig. 6.5. At intermediate momenta one can even find values of the effective diffusion coefficient of up to twice the $\mathcal{N} = 4$ SYM result and at the lowest momenta, we observe that the lattice data is not sensitive to the photon emission rate anymore. This is largely confirming all the results found in this work. As a motivation for future endeavors, one may remark that a study in the theory of non-interacting quarks has revealed that including data points at shorter distances in the inverse problem can have the effect of ruling out large values of D_{eff}, especially at lower photon momenta [64]. This means one has to produce even finer lattices with even higher precision which constitutes a formidable challenge.

Chapter 7

Conclusion

Quantum Chromodynamics describes the interaction of particles that are sensitive to the strong force. One observes that the quarks and gluons are deconfined only at finite temperatures above the chiral critical temperature of QCD. The matter that exists above this temperature is called the quark-gluon plasma (QGP). This QGP matter is examined thoroughly in relativistic heavy-ion collision experiments. One of the most striking phenomena observed, is the ability of the plasma to form collective excitations despite its rapid expansion.

Other observables of interest are electromagnetic probes as they do not interact strongly with the medium created in a relativistic heavy-ion collision. Hence, they can serve as probes of the early (and later) stages of the collision because they escape the medium without very many rescatterings. One such observable is the rate of photon emission by the QGP. This photon production rate is intrinsically connected to the dilepton production rate which is important for heavy-ion phenomenology. Additionally, the production of photons or of weakly-interacting probes by the QGP in general may be relevant for validating or ruling out dark matter candidates. Being a real-time quantity, the rate of photon emission from the quark-gluon plasma can be addressed within the framework of Euclidean path integrals only by applying an analytic continuation. This translates to an ill-conditioned inverse problem when employing the numerical realization of QCD called lattice QCD. Attempting at a solution of the inverse problem constitutes a formidable task and the main body of this work.

Within the course of this work two fine lattices at finite temperatures of $T = 508\,\mathrm{MeV}$ and $T = 254\,\mathrm{MeV}$ (labeled Y7 and X7, respectively) were generated using the $\mathcal{O}(a)$ improved Wilson gauge action and the $\mathcal{O}(a)$ improved Wilson fermion action with $N_f = 2$ mass degenerate light quarks. The bare lattice parameters as well as

algorithmic parameters had to be tuned in order to simulate at a line of constant physics where the $\overline{\mathrm{MS}}$ mass was set to $\sim 13\,\mathrm{MeV}$. With two more ensembles at $254\,\mathrm{MeV}$ a continuum limit extrapolation of the relevant 2-point functions could be performed using the configurations of the X7 ensemble.

Thermal screening masses corresponding to the conserved vector current are of interest as they give an estimate about the inverse correlation length over which an electric field is screened in a strongly interacting medium. The present study of the static and non-static screening masses of the isovector vector correlator shows very good agreement with perturbative results in the S-wave channels, i.e. the transverse channel of the static sector and the longitudinal channel of the non-static sector at a temperature of $T = 508\,\mathrm{MeV}$. A previous study using staggered fermions observed that lattice results in the transverse channel of the static sector cross the $2\pi T$ line from below which is confirmed by the present study using $\mathcal{O}(a)$ improved Wilson fermions. Because of the agreement between lattice and effective theory results, the applicabilty of the perturbative treatment at temperatures relevant for heavy-ion phenomenology is confirmed as well. The corresponding amplitudes can tell whether a quark-antiquark pair is bound tightly or not. The agreement between the lattice and the perturbative approach for the calculated amplitudes is less good although there was improvement made with regard to previous studies. The present study indicates that the quark-antiquark pair is more loosely bound at higher temperatures than at lower ones. One can establish a connection between real-time phenomena of the QGP and non-static screening masses because one encounters the same effective potential in the description of non-static screening masses as when calculating the dilepton production rate. Moreover, the screening pole occurring in Euclidean data can be analytically continued to the diffusion pole in the retarded correlator. Thus, a future application of this study may consist in extracting the diffusion coefficient using non-static screening masses, see Eq. (5.2).

The inverse problem occurring at the heart of the calculation of the photon rate from Euclidean lattice data is tackled in a twofold way. Firstly, the Backus-Gilbert method consists in finding a set of coefficients that depend only on the spectral representation of the Euclidean correlator with a given kernel and the original data points in order to construct an estimator for the spectral function connected to the correlator. One assumes that the true spectral function one wants to estimate, is only slowyly varying and smooth. Thus, the applicability of the Backus-Gilbert method is limited. And secondly, a model ansatz in form of a rational Padé approximant is employed. It allows for a pole structure which is inspired by both the diffusion pole as it arises in the prediction of

hydrodynamics and the quasinormal modes of the retarded correlator in the AdS/CFT picture. Additionally, it satisfies the ultraviolet behavior $\sim \omega^{-4}$ as dictated by the operator product expansion and a superconvergent sum rule. Finally, we impose spectral positivity below the light cone and constraints for the widths of the poles reflecting the fact that there cannot be excitations with arbitrarily long relaxation times in the system. The results for the effective diffusion coefficient are in agreement with previous studies in the quenched limit of lattice QCD and with both the weakly-interacting scenario from perturbation theory and the strongly-interacting scenario from the $\mathcal{N} = 4$ SYM theory at infinite coupling. At photon momenta $1.0\,\mathrm{GeV} \leq k \leq 1.4\,\mathrm{GeV}$, we rule out photon rates twice as large as the weak-coupling prediction. This consolidates results obtained from perturbation theory and hydrodynamic models at these momenta.

This page is left blank intentionally.

Bibliography

[1] R. Rapp, J. Wambach, and H. van Hees, Landolt-Bornstein **23**, 134 (2010), arXiv:0901.3289.

[2] A. Bzdak *et al.*, (2019), arXiv:1906.00936.

[3] D. J. Gross and F. Wilczek, Phys. Rev. Lett. **30**, 1343 (1973), [,271(1973)].

[4] H. D. Politzer, Phys. Rev. Lett. **30**, 1346 (1973), [,274(1973)].

[5] B. S. Kasmaei and M. Strickland, Phys. Rev. **D99**, 034015 (2019), arXiv:1811.07486.

[6] M. Strickland, The non-equilibrium attractor: Beyond hydrodynamics, in *25th Cracow Epiphany Conference on Advances in Heavy Flavour Physics (Epiphany 2019) Cracow, Poland, January 8-11, 2019*, 2019, arXiv:1904.00413.

[7] WA98, M. M. Aggarwal *et al.*, (2000), arXiv:nucl-ex/0006007.

[8] WA80, R. Albrecht *et al.*, Phys. Rev. Lett. **76**, 3506 (1996).

[9] P. Aurenche, F. Gelis, R. Kobes, and H. Zaraket, Phys. Rev. **D58**, 085003 (1998), arXiv:hep-ph/9804224.

[10] WA98, M. M. Aggarwal *et al.*, Phys. Rev. Lett. **85**, 3595 (2000), arXiv:nucl-ex/0006008.

[11] D. K. Srivastava and B. C. Sinha, Eur. Phys. J. **C12**, 109 (2000), arXiv:nucl-th/9906057, [Erratum: Eur. Phys. J.C20,397(2001)].

[12] P. B. Arnold, G. D. Moore, and L. G. Yaffe, JHEP **11**, 057 (2001), arXiv:hep-ph/0109064.

[13] P. B. Arnold, G. D. Moore, and L. G. Yaffe, JHEP **12**, 009 (2001), arXiv:hep-ph/0111107.

[14] P. B. Arnold, G. D. Moore, and L. G. Yaffe, JHEP **06**, 030 (2002), arXiv:hep-ph/0204343.

[15] S. Turbide, R. Rapp, and C. Gale, Phys. Rev. **C69**, 014903 (2004), arXiv:hep-ph/0308085.

[16] S. Turbide, C. Gale, S. Jeon, and G. D. Moore, Phys. Rev. **C72**, 014906 (2005), arXiv:hep-ph/0502248.

[17] J. P. Blaizot, F. Gelis, and R. Venugopalan, Nucl. Phys. **A743**, 13 (2004), arXiv:hep-ph/0402256.

[18] D. K. Srivastava and B. Sinha, Phys. Rev. Lett. **73**, 2421 (1994).

[19] A. Dumitru and D. H. Rischke, Phys. Rev. **C59**, 354 (1999), arXiv:nucl-th/9806003.

[20] J.-e. Alam, S. Sarkar, T. Hatsuda, T. K. Nayak, and B. Sinha, Phys. Rev. **C63**, 021901 (2001), arXiv:hep-ph/0008074.

[21] D. Peressounko, Phys. Rev. **C67**, 014905 (2003).

[22] J.-e. Alam, B. Mohanty, P. Roy, S. Sarkar, and B. Sinha, Phys. Rev. **C67**, 054902 (2003), arXiv:nucl-th/0302054.

[23] D. K. Srivastava and B. Sinha, Phys. Rev. **C64**, 034902 (2001), arXiv:nucl-th/0006018.

[24] NA60, R. Arnaldi *et al.*, Phys. Rev. Lett. **96**, 162302 (2006), arXiv:nucl-ex/0605007.

[25] J. Alam, S. K. Ghosh, P. Roy, and S. Sarkar, J. Phys. **G30**, 1967 (2004), arXiv:nucl-th/0309017.

[26] R. J. Fries, B. Muller, and D. K. Srivastava, Phys. Rev. Lett. **90**, 132301 (2003), arXiv:nucl-th/0208001.

[27] S. Turbide, C. Gale, E. Frodermann, and U. Heinz, Phys. Rev. **C77**, 024909 (2008), arXiv:0712.0732.

[28] B. G. Zakharov, JETP Lett. **80**, 1 (2004), arXiv:hep-ph/0405101, [Pisma Zh. Eksp. Teor. Fiz.80,3(2004)].

[29] ALICE, J. Adam *et al.*, Phys. Lett. **B754**, 235 (2016), arXiv:1509.07324.

[30] N. Brambilla *et al.*, Eur. Phys. J. **C74**, 2981 (2014), arXiv:1404.3723.

[31] A. Anisimov, D. Besak, and D. Bodeker, JCAP **1103**, 042 (2011), arXiv:1012.3784.

[32] D. Besak and D. Bodeker, JCAP **1203**, 029 (2012), arXiv:1202.1288.

[33] T. Asaka, S. Blanchet, and M. Shaposhnikov, Phys. Lett. **B631**, 151 (2005), arXiv:hep-ph/0503065.

[34] T. Asaka and M. Shaposhnikov, Phys. Lett. **B620**, 17 (2005), arXiv:hep-ph/0505013.

[35] T. Asaka, M. Laine, and M. Shaposhnikov, JHEP **06**, 053 (2006), arXiv:hep-ph/0605209.

[36] J. Ghiglieri and M. Laine, JHEP **07**, 078 (2019), arXiv:1905.08814.

[37] P. Schwaller, Phys. Rev. Lett. **115**, 181101 (2015), arXiv:1504.07263.

[38] G. D. Moore, EPJ Web Conf. **175**, 01009 (2018), arXiv:1709.09466.

[39] Particle Data Group, M. Tanabashi *et al.*, Phys. Rev. **D98**, 030001 (2018).

[40] L. D. McLerran and B. Svetitsky, Phys. Rev. **D24**, 450 (1981).

[41] LHCb, R. Aaij *et al.*, Phys. Rev. Lett. **115**, 072001 (2015), arXiv:1507.03414.

[42] D0, V. M. Abazov *et al.*, Phys. Rev. Lett. **115**, 232001 (2015), arXiv:1508.07846.

[43] C. Gattringer and C. B. Lang, Lect. Notes Phys. **788**, 1 (2010).

[44] R. P. Feynman, Rev. Mod. Phys. **20**, 367 (1948).

[45] J. I. Kapusta and C. Gale, *Finite-temperature field theory: Principles and applications*, Cambridge Monographs on Mathematical Physics (Cambridge University Press, 2011).

[46] H. B. Meyer, Eur. Phys. J. **A47**, 86 (2011), arXiv:1104.3708.

[47] K. G. Wilson, Phys. Rev. **D10**, 2445 (1974), [,45(1974); ,319(1974)].

[48] H. J. Rothe, World Sci. Lect. Notes Phys. **43**, 1 (1992), [World Sci. Lect. Notes Phys.82,1(2012)].

[49] ALPHA, M. Guagnelli *et al.*, Nucl. Phys. **B595**, 44 (2001), arXiv:hep-lat/0009021.

[50] M. Luscher, Modern perspectives in lattice QCD: Quantum field theory and high performance computing. Proceedings, International School, 93rd Session, Les Houches, France, August 3-28, 2009 , 331 (2010), arXiv:1002.4232.

[51] ALPHA, M. Della Morte *et al.*, Nucl. Phys. **B713**, 378 (2005), arXiv:hep-lat/0411025.

[52] H. Panagopoulos and Y. Proestos, Phys. Rev. **D65**, 014511 (2002), arXiv:hep-lat/0108021.

[53] M. Luscher and P. Weisz, Nucl. Phys. **B479**, 429 (1996), arXiv:hep-lat/9606016.

[54] P. Fritzsch *et al.*, Nucl. Phys. **B865**, 397 (2012), arXiv:1205.5380.

[55] ALPHA, K. Jansen and R. Sommer, Nucl. Phys. **B530**, 185 (1998), arXiv:hep-lat/9803017, [Erratum: Nucl. Phys.B643,517(2002)].

[56] P. Fritzsch, J. Heitger, and N. Tantalo, JHEP **08**, 074 (2010), arXiv:1004.3978.

[57] M. Hasenbusch, Phys. Lett. **B519**, 177 (2001), arXiv:hep-lat/0107019.

[58] M. Hasenbusch and K. Jansen, Nucl. Phys. **B659**, 299 (2003), arXiv:hep-lat/0211042.

[59] M. Marinkovic and S. Schaefer, PoS **LATTICE2010**, 031 (2010), arXiv:1011.0911.

[60] B. B. Brandt, A. Francis, H. B. Meyer, and H. Wittig, JHEP **03**, 100 (2013), arXiv:1212.4200.

[61] B. B. Brandt, A. Francis, M. Laine, and H. B. Meyer, JHEP **05**, 117 (2014), arXiv:1404.2404.

[62] S. Schaefer, R. Sommer, and F. Virotta, PoS **LAT2009**, 032 (2009), arXiv:0910.1465.

[63] ALPHA, S. Schaefer, R. Sommer, and F. Virotta, Nucl. Phys. B **845**, 93 (2011), arXiv:1009.5228.

[64] M. Cè, T. Harris, H. B. Meyer, A. Steinberg, and A. Toniato, (2020), arXiv:2001.03368.

[65] B. B. Brandt, A. Francis, H. B. Meyer, and D. Robaina, Phys. Rev. D **90**, 054509 (2014), arXiv:1406.5602.

[66] B. B. Brandt, A. Francis, H. B. Meyer, and D. Robaina, Phys. Rev. **D92**, 094510 (2015), arXiv:1506.05732.

[67] B. B. Brandt, A. Francis, H. B. Meyer, A. Steinberg, and K. Zapp, PoS **LATTICE2016**, 072 (2016), arXiv:1611.09689.

[68] H.-T. Ding, O. Kaczmarek, S. Mukherjee, H. Ohno, and H. T. Shu, Phys. Rev. **D97**, 094503 (2018), arXiv:1712.03341.

[69] H. B. Meyer, PoS **LATTICE2015**, 014 (2016), arXiv:1512.06634.

[70] B. B. Brandt, A. Francis, M. Laine, and H. B. Meyer, Nucl. Phys. **A931**, 861 (2014), arXiv:1408.5917.

[71] H. B. Meyer, Eur. Phys. J. **A54**, 192 (2018), arXiv:1807.00781.

[72] E. Braaten and A. Nieto, Phys. Rev. Lett. **73**, 2402 (1994), arXiv:hep-ph/9408273.

[73] P. B. Arnold and L. G. Yaffe, Phys. Rev. **D52**, 7208 (1995), arXiv:hep-ph/9508280.

[74] M. Laine and M. Vepsalainen, JHEP **02**, 004 (2004), arXiv:hep-ph/0311268.

[75] M. Laine and A. Vuorinen, Lect. Notes Phys. **925** (2016), arXiv:1701.01554.

[76] P. B. Arnold, G. D. Moore, and L. G. Yaffe, JHEP **05**, 051 (2003), arXiv:hep-ph/0302165.

[77] S. Caron-Huot, P. Kovtun, G. D. Moore, A. Starinets, and L. G. Yaffe, JHEP **12**, 015 (2006), arXiv:hep-th/0607237.

[78] P. Aurenche, F. Gelis, G. D. Moore, and H. Zaraket, JHEP **12**, 006 (2002), arXiv:hep-ph/0211036.

[79] M. Cheng *et al.*, Eur. Phys. J. **C71**, 1564 (2011), arXiv:1010.1216.

[80] H. B. Meyer, JHEP **04**, 099 (2010), arXiv:1002.3343.

[81] B. B. Brandt, A. Francis, B. Jäger, and H. B. Meyer, Phys. Rev. **D93**, 054510 (2016), arXiv:1512.07249.

[82] L. D. McLerran and T. Toimela, Phys. Rev. **D31**, 545 (1985).

[83] M. E. Carrington, A. Gynther, and P. Aurenche, Phys. Rev. **D77**, 045035 (2008), arXiv:0711.3943.

[84] J. Ghiglieri, O. Kaczmarek, M. Laine, and F. Meyer, Phys. Rev. **D94**, 016005 (2016), arXiv:1604.07544.

[85] M. Laine, JHEP **11**, 120 (2013), arXiv:1310.0164.

[86] S. Jeon, Phys. Rev. **D52**, 3591 (1995), arXiv:hep-ph/9409250.

[87] J. Hong and D. Teaney, Phys. Rev. **C82**, 044908 (2010), arXiv:1003.0699.

[88] G. Backus and F. Gilbert, Geophysical Journal of the Royal Astronomical Society **16**, 169 (1968).

[89] A. Francis, O. Kaczmarek, M. Laine, T. Neuhaus, and H. Ohno, Phys. Rev. **D92**, 116003 (2015), arXiv:1508.04543.

[90] B. B. Brandt, A. Francis, T. Harris, H. B. Meyer, and A. Steinberg, EPJ Web Conf. **175**, 07044 (2018), arXiv:1710.07050.

[91] P. K. Kovtun and A. O. Starinets, Phys. Rev. **D72**, 086009 (2005), arXiv:hep-th/0506184.

[92] H.-T. Ding, O. Kaczmarek, and F. Meyer, Phys. Rev. **D94**, 034504 (2016), arXiv:1604.06712.

[93] G. Jackson and M. Laine, JHEP **11**, 144 (2019), arXiv:1910.09567.

[94] B. B. Brandt *et al.*, Lattice QCD estimate of the quark-gluon plasma photon emission rate, in *37th International Symposium on Lattice Field Theory (Lattice 2019) Wuhan, Hubei, China, June 16-22, 2019*, 2019, arXiv:1912.00292.